DEPARTAMENTO DE ASTROFISICA

Universidad de La Laguna

S-process nucleosynthesis in AGB stars with the full spectrum of turbulence scheme for convection

Memoria que presenta
D. Andrés Yagüe López
para optar al grado de
Doctor en Ciencias Físicas.

INSTITUTO Đ ASTROFISICA Đ CANARIAS
junio de 2018

Examination date: July, 2018
Thesis supervisors: Prof. Paolo Ventura & Dr. Domingo Aníbal García Hernández

ISBN: xx-xxx-xxxx-x
Depósito legal: TF-xxxx/2018

a mi familia,
a Elena

Agradecimientos

Un doctorado no se debe ni puede hacer en solitario y, desde el primer review leído hasta el punto y final de la tesis, se acumula un sinnúmero de contribuciones que permiten llevarlo a buen término. Quizá las contribuciones más directas sean también las menos interesantes: los artículos citados y el estudiante que realiza el trabajo y lo plasma en la memoria de la tesis. Obviando, pues, lo obvio, a las primeras personas que debo agradecer la existencia de este trabajo es a mis supervisores y las instituciones de las que forman parte: Paolo Ventura y el observatorio astronómico de Roma (OAR-INAF), y Aníbal García Hernández junto con el Instituto de Astrofísica de Canarias.

De forma menos oficial pero no por ello menos importante, he acumulado una gran deuda tanto con Maria Lugaro como con Carolyn Doherty, las cuales trabajan actualmente en el observatorio de Konkoly. Durante mi visita de poco más de dos meses a esta institución magiar, ambas investigadoras me brindaron sus vastos conocimientos en la materia principal de esta tesis. Sin su predisposición para responder a todas y cada una de mis innumerables preguntas, el trabajo que tienes hoy entre tus manos no existiría.

Por supuesto no ha sido todo trabajar en estos años de aprendizaje, pues el espacio entre un resultado y el siguiente está lleno del resto de la vida. Y la vida, sin compañía, sabe un poco desabrida. Por ello querría también extender mis agradecimientos a los más cercanos de entre mis amigos: Carlos, Tanausú, Fidel, Mariano y a mi pareja Elena, cuyo apoyo y aliento en cada momento de este proceso han sido de valor incalculable. Finalmente, no puedo olvidarme de mi familia, puesto que tanto mi madre como mi padre y su mujer, Vanessa, y mis hermanos y hermanas Alveán, Miguel, Pablo, Alberto y Lucía, me han ayudado a trazar el camino que me ha llevado a ser quien soy.

Resumen

En esta tesis describimos SNUPPAT (llamado así por sus siglas en inglés ***s**-process **nu**cleosynthesis **p**ost **p**rocessing code for **At**on*), un código numérico que hemos desarrollado de post-procesado para el cálculo de la nucleosíntesis debida al proceso de captura lenta de neutrones (*s*-process) para el código de evolución estelar ATON. El objetivo es proporcionar al código ATON, que se diferencia de otros códigos de evolución estelar en ciertas características físicas clave, una forma de predecir la nucleosíntesis de elementos pesados en estrellas de masa baja e intermedia. Para ello necesitamos incrementar el número de especies atómicas cuya evolución seguimos desde las 30 (desde el hidrógeno hasta el ^{31}P) de ATON hasta unas 320 (desde el hidrógeno hasta el ^{210}Po) como mínimo. A largo plazo estamos interesados en obtener una mayor comprensión de los procesos físicos que se dan en el interior de las estrellas en la fase TP-AGB (del inglés *thermally pulsing asymptotic giant branch*).

Para lograr este objetivo, hemos creado un código de nucleosíntesis desde cero, descrito al comienzo de esta tesis. También hemos decidido incluir una serie de posibles optimizaciones a los métodos numéricos tradicionales utilizados para este tipo de problemas astrofísicos. Para completar la descripción del código SNUPPAT también estudiamos cómo mezclar correctamente las abundancias elementales en este tipo de estrellas. Esto incluye tanto la mezcla debida a la convección como la debida a un caso de overshooting convectivo. Este último es esencial para la formación de un *pocket* de ^{13}C, necesario para la nucleosíntesis en las estrellas en la fase de TP-AGB.

Tras la descripción del código de nucleosíntesis, presentamos las predicciones a metalicidad solar de SNUPPAT en la forma de abundancias finales en la superficie de la estrella. Exploramos tanto con distintas masas iniciales (en el rango 3-6 $M_\odot$) como con distintos parámetros de *overshooting*. Seguidamente, analizamos estos resultados teóricos para trazar una conexión entre las abundancias superficiales y los diferentes procesos físicos que se dan en las capas

más profundas de las estrellas AGB.

Finalmente, comparamos nuestros resultados con los de otros códigos de nucleosíntesis de *s*-process conocidos. Al hacerlo, encontramos un acuerdo razonable con al menos uno de ellos (en concreto, los de la versión MONASH del *Mount Stromlo Stellar Structure Program*), precisamente los modelos de nucleosíntesis que mejor explican la limitada información observacional (abundancias de Rb, Zr) de la que se dispone hasta la fecha. Con esta comparación concluimos que los modelos conjuntos de ATON y SNUPPAT parecen generar estrellas más calientes a la misma masa y con relativa baja eficiencia del tercer dragado. Este hecho nos obliga a incrementar la producción debida a la nucleosíntesis en las capas más internas para obtener resultados comparables en la superficie. Como consequencia de esto los modelos de SNUPPAT muestran, en general, signos de una mayor captura neutrónica en las abundancias finales de la superficie estelar.

Abstract

This thesis describes SNUPPAT (***s***-process **nu**cleosynthesis **p**ost **p**rocessing code for **At**on), a post-processing slow neutron-capture process (*s*-process) code developed by us for the stellar evolutionary code ATON. The aim is to provide ATON, which shows distinct key physical characteristics to other evolutionary codes, with the capability of following heavy element nucleosynthesis in low- to intermediate-mass stars. Meaning that we have to increase the number of species followed from 30 (ATON follows 30 species from hydrogen to ^{31}P) to around 320 (from hydrogen to ^{210}Po) at the very least. In the long term we hope that, through ATON nucleosynthesis predictions, we may open the way to a deeper understanding of the physics and evolution during the thermally pulsing asymptotic giant branch (TP-AGB) phase.

This objective is realized by the creation from scratch of a nucleosynthesis code, explained at the beginning of this thesis, along with possible optimizations to some of the traditional numerical methods used for these kind of astrophysical problems. We also tackle the issue of mixing, which includes both the convective mixing as well as the convective overshooting responsible of, among other things, the formation of an effective ^{13}C pocket, essential for nucleosynthesis in TP-AGB stars.

Following the code description, we present SNUPPAT solar metallicity results in the form of final stellar surface abundances. We explore different stellar initial masses as well as variations of the extra-mixing parameter, which governs the convective overshooting behavior. These results are analyzed to connect them with the different physical processes taking place in the deeper layers of the AGB stars.

Finally, we compare our results with those from other known *s*-processing numerical codes, finding a reasonably good agreement with at least one of them (specifically, the MONASH version of the Mount Stromlo Stellar Structure Program), which coincidentally is the nucleosynthesis code that better explains the

currently limited observational information (Rb, Zr abundances) about these stars. We note the fact that ATON-SNUPPAT appears to generate hotter models with a low third dredge-up efficiency that forces us to increase the nucleosynthesis output in the helium intershell, in order to obtain comparable surface abundances. The consequence is that SNUPPAT predictions present, generally, the signs of a higher overall neutron exposure (a measure of the total neutron captures) in the final stellar surface abundances.

Contents

1

Introduction

1.1 Stellar evolution: from the main sequence to the TP-AGB

From the first fusion reaction to the last, the behavior and evolution of a star is dominated mainly by its structure, initial mass, and chemical composition. Due to their distinct evolutionary paths, there are several possible subdivisions according to the initial stellar mass (see Figure 1.1). Among these, here we are interested in primarily two of them, which are the low- ($\lesssim 2$ $M_\odot$) and intermediate-mass (2 $M_\odot \lesssim M \lesssim 8$ $M_\odot$) stars.

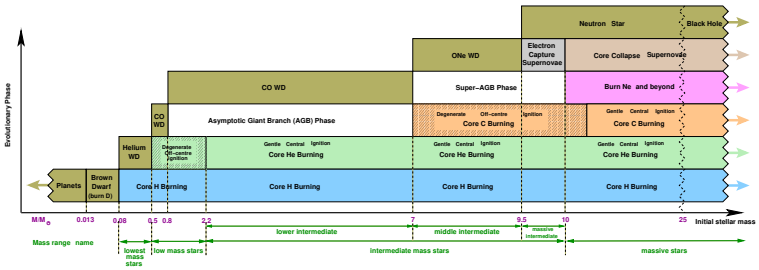

Figure 1.1— Scheme showing the different subdivisions (evolutionary phase and final fate) depending on the initial stellar mass. Adapted from Karakas & Lattanzio (2014).

Stars below 2 $M_\odot$ can be further subdivided into stars above and below the 1.5 $M_\odot$ limit. This mass is the limit between the efficient activation of the pp chain or the CNO cycle for energy production through hydrogen fusion during the Main Sequence (MS). The notable difference between these two

cases is the nature of the energy transportation outside of the stellar core, with the pp chain energy being transported radiatively to the shallower layers of the star and the CNO cycle luminosity triggering a convective instability. Once the core hydrogen is spent, these stars exit the MS and enter the Red Giant Branch (RGB). At this point, the stellar structure consist of an inert helium core surrounded by a hydrogen burning shell. During the RGB phase the helium core contracts continuously, increasing the hydrogen burning shell temperature and the surface luminosity. This change in structure deepens the stellar convective envelope until it encompasses the majority of the stellar mass, mixing the products from the hydrogen burning up to the surface. This process is known as "first dredge-up". The second significative consequence of this phase is the degeneracy of the helium core, effectively decoupling the temperature and pressure of the material there and setting up the stage for the event known as the helium flash.

When the temperature in the core is high enough (around 0.1 GK), the 3α reaction activates, burning helium into carbon and oxygen. The electron degeneracy of the core allows for the increase in temperature without producing an expansion of the gas, in account of the pressure remaining constant through the process. Therefore, a feedback loop occurs by which the luminosity released by the 3α reaction increases the core temperature which, in turn, increases the efficiency of the 3α reaction without any mechanism able to counteract it. Eventually, a high enough temperature is reached for the degeneracy status of the core gas to change into a non-degenerate state. At this moment the helium flash occurs, moving the star to the Horizontal Branch (HB) where the helium core burns at a more sustained rate and the hydrogen keeps fusing in a shell around the core.

After the helium in the core is exhausted, it contracts until the temperature is high enough to re-ignite a helium shell surrounding the inert carbon-oxygen core. In this situation both helium and hydrogen burn in shells around the core, which puts the star in the Asymptotic Giant Branch (AGB) phase. In this stage, the helium burning shell soon becomes thin and unstable, giving rise to an alternate ignition of the helium and hydrogen shells. In this situation, the helium burning period, shorter ($\sim 10^2 - 10^3$ years) and more luminous than its hydrogen counterpart, is usually referred to as a thermal pulse (TP), while the longer ($\sim 10^4$ years) hydrogen burning phase is consequently known as an interpulse period. During the interpulse the hydrogen burns just below the convective envelope transmuting into helium, which accumulates in the region known as the helium intershell that sits between the hydrogen-rich convective envelope and the inert CO core (see Figure 1.2). When enough helium mass is generated, it ignites starting a TP, switching off the hydrogen burning, and

increasing the core mass in the process. The energy increase is sudden enough so that a convective zone (the pulse driven convective zone or PDCZ) develops in the helium burning shell. There is also a penetration of the convective envelope into the lower stellar layers, mixing the products from the hydrogen burning region and, as we will later see, the *s*-process nucleosynthesis back to the surface. This process is known as the "third dredge-up" (TDU), and the whole process takes place during what is known as the thermally pulsing AGB (TP-AGB) phase.

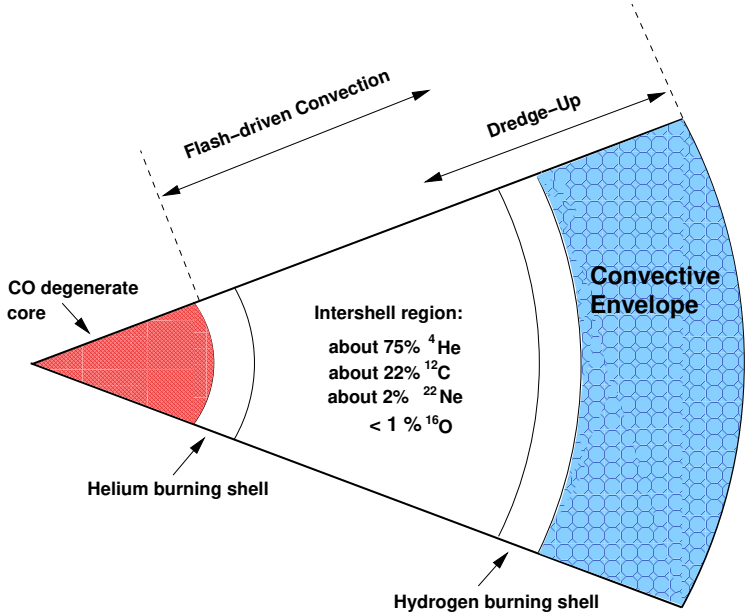

FIGURE 1.2— General structure of an AGB star. Adapted from Karakas & Lattanzio (2014).

The stars above 2 and below 7 $M_{\odot}$ follow a slightly different path than their less massive counterparts into the TP-AGB phase. In particular, these stars do not suffer from an helium flash and, instead, if they are initially more massive than ~ 4 $M_{\odot}$ they experience what is known as the "second dredge-up". This event occurs when the helium in the core is spent, with a strong expansion inhibiting the hydrogen burning shell and the inner edge of the convective

envelope expanding to reach it, mixing its ashes to the surface.

Independently of the initial stellar mass, during this phase the AGB star loses most of its mass (up to 80% of their initial mass for the more massive AGB stars) in the form of stellar winds (see e.g., Vassiliadis & Wood 1993), enriching the interstellar medium with the products of the nucleosynthesis processes that shape the envelope composition after each TDU event.

A more detailed description of the AGB stellar evolution can be found in the literature (see e.g., Iben 1991; Herwig 2005; Karakas & Lattanzio 2014)

1.2 Nucleosynthesis during the TP-AGB

Among the different events that can change the stellar surface chemical make-up during the evolution of low- and intermediate-mass stars, the most important nucleosynthesis processes occur during the TP-AGB phase. For these masses the heavy element nucleosynthesis takes place through a process that starts with the capture of free neutrons by the so-called iron seed nuclei[1] (see e.g., Cameron 1955; Busso et al. 1999; Straniero et al. 2009). These captures along with the β-decay climb up the stability valley of the chart of nuclides, slowly transmuting a fraction of the iron seeds into every heavy element between them and ^{210}Po, which sits at the end of the stability valley. The specific path taken by this process depends on the neutron density and temperature, which sets the relative timescale between the competing neutron capture and β-decay processes. In the stellar mass range 1-8 $M_{\odot}$, the neutron capture timescale is, generally, orders of magnitude slower than that of the decay process. This is the reason why this process is usually referred to as the *slow* or *s*-process[2] (e.g., Busso et al. 1999). An example of the path taken by this nucleosynthesis process is represented in Figure 1.3.

The free neutrons necessary for the *s*-process to take place come from the ^{13}C(α, n)^{16}O (commonly referred to as the ^{13}C neutron source) and ^{22}Ne(α, n)^{25}Mg (the ^{22}Ne neutron source) reactions. Each one of these neutron sources defines a different regime with its own nucleosynthesis signature (e.g., Lambert et al. 1995; Abia et al. 2002; Straniero et al. 2006; García-Hernández et al. 2006; van Raai et al. 2012). The reason behind this is that the activation temperature for the ^{13}C neutron source is around 70 to 90 MK, well within the possibilities of an intershell from a low- to intermediate-mass star during an interpulse period. The ^{22}Ne neutron source, however, requires a minimum temperature

[1] Mainly ^{56}Fe.

[2] In contrast with the rapid or *r*-process, in which the neutron capture timescale is faster than the β-decay rates. The *r*-process takes place in the more massive stars, such as those that undergo core-collapse supernova (see e.g., Qian 2003).

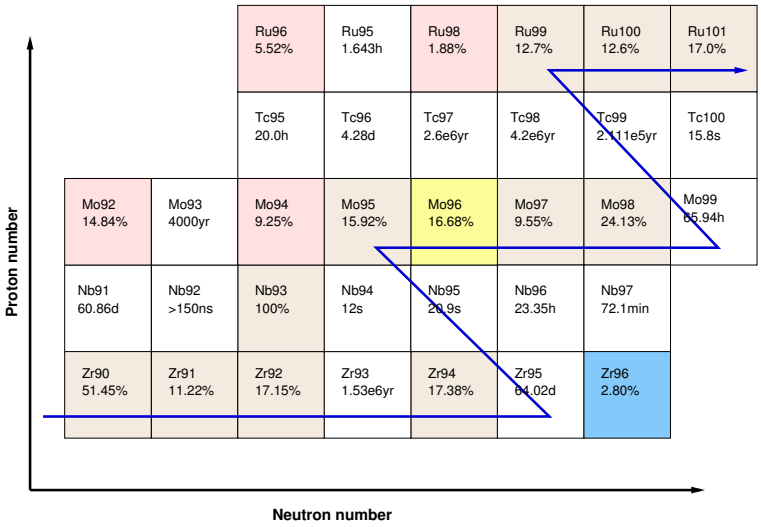

FIGURE 1.3— Example of the s-process path around the ^{96}Mo. The white squares denote the unstable isotopes with the half-life of their ground state displayed below their symbols. The blue line represent the s-process path for a low-neutron density case. The rightward direction in the chart represents the increase in neutron number due to neutron captures, while the row changes that follow an upper-left diagonal path indicate the species transmutation after a β-decay event. Figure adapted from Karakas & Lattanzio (2014).

around 300 MK, which is usually only attained during the short-lived TP (e.g., Goriely & Mowlavi 2000; van Raai et al. 2012). Furthermore, although there is plenty of ^{22}Ne in the He intershell, ^{13}C must be created from existing ^{12}C and protons through the ^{12}C(p, γ)^{13}N(β^+)^{13}C reaction. Unfortunately, protons are completely exhausted below the convective envelope and, in order for there to be enough ^{13}C, there must be a mechanism to mix them into the He intershell. Among the proposed mechanisms to explain this mix for solar metallicity stars, we find from the relatively well known convective overshooting and rotation (e.g., Herwig & Langer 2000), to the arguably more interesting thermohaline and magnetic buoyancy cases (e.g., Palmerini et al. 2011). Moreover, whichever the actual mechanism for proton mixing into the He intershell is, it must be compatible with the formation of a decreasing proton profile from the convective envelope to the deeper stellar layers. The reason is that, with an homogeneous

proton abundance typical of the convective envelope, the neutron poison ^{14}N is synthesized as well, inhibiting the whole *s*-process nucleosynthesis chain (e.g., Lugaro et al. 2003; Cristallo et al. 2009).

These fundamental differences between the neutron sources translate into different nucleosynthesis signatures for each one, with the ^{13}C neutron source producing abundance distributions typical of a low-neutron density (10^{7-8} n/cm^3) and high neutron exposure nucleosynthesis, mainly enhancing the Ba peak (atomic number Z $\sim$ 56). This neutron source produces the higher surface overabundances of heavy *s*-process elements, and is therefore known as the main component of the *s*-process. Conversely, the ^{22}Ne neutron source produces abundance distributions compatible with higher neutron densities (10^{10-12} n/cm^3) and lower neutron exposures, enhancing mainly the Sr peak (Z $\sim$ 38). With a typically lower *s*-element surface overabundances relative to the main component, this neutron source is also referred to as the weak component of the *s*-process.

Because of the different physical conditions for each of the neutron sources, not all TP-AGB stars are capable of efficiently activating both of them. For example, for the lower end of the mass spectrum (below 4 - 4.5 M$_\odot$) the temperatures in the He intershell do not rise above the 300 MK threshold for the ^{22}Ne neutron source to efficiently activate and the *s*-process nucleosynthesis is expected to be dominated by the ^{13}C neutron source (e.g., Lambert et al. 1995; Abia et al. 2002). On the other hand, some authors (see e.g., Goriely & Siess 2004) argue that for stars with an initial mass above 5 M$_\odot$, the ^{13}C pocket never protrudes outside of the ^{14}N rich pocket, being therefore effectively inhibited by it; this time the ^{22}Ne neutron source is expected to dominate the *s*-process elements production (e.g., García-Hernández et al. 2006, 2007, 2009, 2013; van Raai et al. 2012).

The way these neutron sources impact the stellar surface abundances is related to both the neutron density and exposure during the *s*-process nucleosynthesis. The neutron density is a self-explanatory concept and an intuitive way to understand the neutron exposure is as an indicator of the number of free neutrons (and, therefore, captures) available during any particular neutron capture process. In principle, each species has a unique neutron capture cross section, this means that for two species to have the same probability of capturing a neutron, the product σY, where Y represents the number fraction of the species and σ its neutron capture cross section, must be the same. This fact results in several bottlenecks along the *s*-process path where the neutron magic numbers (50, 82, and 126) are located (such as near the Sr or Ba). The neutron capture cross section for a species with a neutron magic number is much lower than its neighboring nuclides, producing the accumulation of such nuclides un-

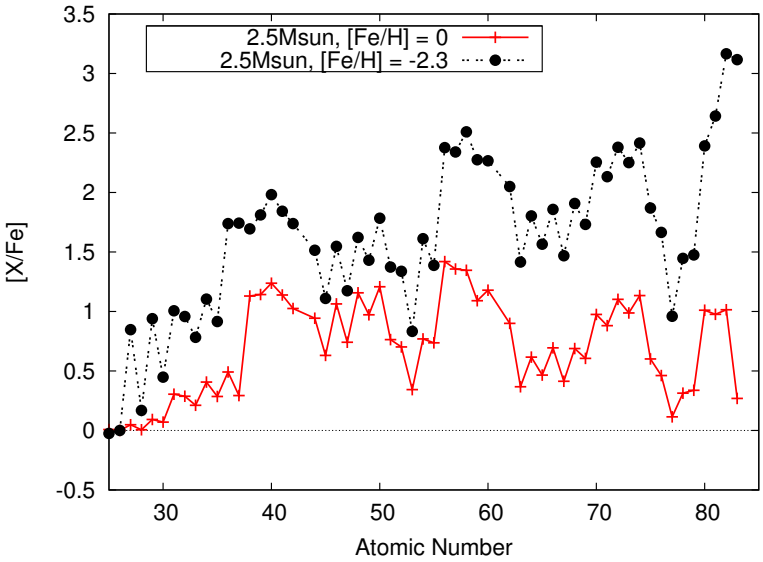

FIGURE 1.4— Typical stellar surface abundance distributions of a low-mass AGB star at solar and sub-solar metallicity. With this figure we wish to bring attention to the different relative heights of the peaks found around Z = 38, 56, and 80. The differences between the abundance distributions are produced by the difference in metallicity, because metallicity and neutron exposure are negatively correlated (Clayton 1988). Figure adapted from Karakas & Lattanzio (2014).

til enough abundance is produced so that they might capture neutrons as well, allowing for the synthesis of heavier elements (e.g., Clayton et al. 1961).

This behavior creates what is known as the three *s*-process peaks. The first one located around Sr, the second one around Ba, and the third one near the end of the stability valley around Pb. The relative overabundance of each peak with respect to the other two indicates the high or low neutron exposure nature of the nucleosynthesis at the *s*-process site (see Figure 1.4).

The dependence of the abundances distribution on the neutron density is best explained by the existence of what is known as "branching points". These points consist of isotopes for which the nucleosynthesis path can follow either a neutron capture or a β-decay with comparable probability, and the balance can be tipped to one side or the other depending on the neutron density (see Figure

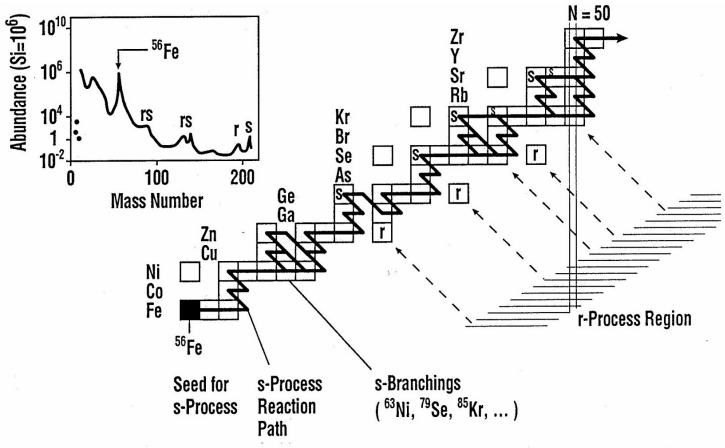

FIGURE 1.5— Scheme of the *s*-process path along with several of its branching points. Adapted from Käppeler et al. (2010).

1.5). For example, in Table 1.1, we show the probability of both ^{85}Kr and ^{86}Rb of capturing a neutron instead of suffering a decay depending on the current neutron density. If the new path goes through a stable or slowly decaying isotope (such as is the case for the ^{87}Rb), then a higher neutron density can modify the ratios between certain key elements in the stellar surface abundances distribution.

Finally, it is to be noted that we have intentionally left out of this discussion other examples of surface chemical evolution and nucleosynthesis processes such as the first and second dredge-ups or the Hot Bottom Burning (HBB, see e.g.,

n/cm^3	^{85}Kr	^{86}Rb
1×10^6	0.67%	0.03%
4×10^7	21.16%	1.05%
1×10^9	87.03%	20.99%
1×10^{12}	99.99%	99.62%

TABLE 1.1— Probability of neutron capture versus β-decay for ^{85}Kr and ^{86}Rb for a number of representative neutron densities.

Boothroyd et al. 1993; Mazzitelli et al. 1999). The reason is that, although these processes do indeed change the surface composition of the star (with the HBB in particular being responsible for the destruction of surface ^{12}C, and the production of N and Li, see e.g., García-Hernández et al. 2007, 2013, and references therein), they do not affect the heavy *s*-elements production that we are studying in this thesis. We have also left out of the discussion the proton-ingestion mechanism due to it being restricted to metal-poor stars (see e.g., Stancliffe et al. 2011).

1.3 An *s*-process nucleosynthesis code for ATON

Up to this point, we have briefly stated how the physical characteristics of the star affect the final abundances both in total overabundance and chemical distribution. Of course, in order to understand the physical mechanisms taking place inside stars in the TP-AGB phase, a comprehensive theory regarding the stellar evolution has to be detailed in the form of stellar models. Once those are available, one can solve the nucleosynthesis equations for the *s*-process mechanism and obtain what would be the particular theoretical prediction for a specific evolutionary code. These predictions can be then compared with either astronomical observations (i.e., stellar abundances) or predictions from other nucleosynthesis models to determine the validity of the implied understanding of the physical processes the evolutionary code has.

However, we cannot forget that the *s*-process nucleosynthesis code is subject to a number of hypotheses as well that can hide the actual impact that the evolutionary model has on the obtained abundances. Nevertheless, by carefully exposing the inner workings of the *s*-process nucleosynthesis code, we believe that it is possible to elucidate to some extent which effect belongs to each supposition.

For this reason we find very valuable the creation of a post-processing *s*-process nucleosynthesis code for the stellar evolutionary code ATON (e.g., Ventura et al. 2008). This is because ATON stands apart from other stellar evolutionary codes in that it uses the Full Spectrum of Turbulence (FST) convective scheme (Canuto et al. 1996), as well as the Blöcker AGB mass loss prescription (Blöcker 1995). These choices, among others, produce notable differences in different nucleosynthesis mechanisms such as the HBB strength, the TDU efficiency, the number of TPs, etc. It is natural then to inquire how these differences affect the heavy *s*-process element nucleosynthesis, and if a more profound knowledge of the present subject can be derived.

In order to provide ATON with *s*-process nucleosynthesis capabilities, a post-processing nucleosynthesis code may be written specifically for it, allow-

ing the Rome group, the developers of the ATON code, to contribute more extensively to our present understanding on AGB evolution and nucleosynthesis with its multiple applications to several astrophysical topics like the interstellar medium enrichment, chemical evolution of galaxies and globular clusters, among others.

Furthermore, the *s*-process nucleosynthesis calculations are notoriously difficult, requiring efficient codes to carry on the simulations within a reasonable period of time with given computationally constrains. Therefore, we understand that the developing of this kind of complex numerical code as an opportunity to experiment with different solutions and optimization paths for the nucleosynthesis problem (see Chapter 2).

These optimizations may gain more relevance when the research moves to stellar evolutionary codes in higher dimensions. This shift is highly attractive because of its explanatory power. A 3D hydrodynamic simulation, for example, requires fewer assumptions and is a more powerful tool to broaden our understanding of certain physical processes such as convection (see e.g., Müller & Janka 2015; Tremblay et al. 2013; Magic et al. 2013). The problem is that, for higher dimensions the computational cost rapidly multiplies, requiring symmetry considerations along with smaller simulation ranges and raw computing power to solve in a reasonable amount of time. In a first order of magnitude approximation, a factor of 2 acceleration for the nucleosynthesis calculations can then become a factor of 8 optimization for a 3D model that attempts to solve the nucleosynthesis equations in each dimension.

1.4 Thesis outline

In this thesis we develop SNUPPAT, a *s*-process post-processing AGB nucleosynthesis code for ATON. We do this to allow for the calculation of heavy *s*-element nucleosynthesis predictions in low- and intermediate-mass stars for that code, which may give us new insight into the *s*-process nucleosynthesis on AGB stars.

In Chapter 2 we describe the nucleosynthesis problem along with our preferred method for solving it. We also include two apparently powerful optimization techniques developed during this PhD work that allow us to perform *s*-process simulations in a much shorter time than what other codes manage to do. We end the chapter by performing some simple sanity checks on the selected methods to ensure that an accurate integration of the nucleosynthesis equations can be carried on by them.

Chapter 3 is devoted to the description of the mixing algorithms (both convective mixing and convective overshooting), and how those algorithms affect

the abundances calculated by the code. We also briefly study the effect of the mesh resolution in the ^{13}C neutron source, and describe our attempt at a basic parallelization technique. Finally, we test the whole code including the mixing algorithms using ATON to check the extent of the consistency between the evolutionary and post-processing codes.

In Chapters 4 and 5 we present the ATON-SNUPPAT solar metallicity 3-5 $M_{\odot}$ stellar surface abundance predictions along with a comparison among them. We also compare them with the results from other known *s*-process nucleosynthesis codes.

Finally, Chapter 6 contains a summary of the main conclusions of this thesis work, while in Chapter 7 we detail a handful of possible avenues for future work.

2

SNUPPAT: Solving the nucleosynthesis equations

This chapter contains the description of the post-processing code SNUPPAT. Specifically, we discuss its implementation for solving the *s*-process nucleosynthesis in ATON stellar models for low- and intermediate-mass AGB stars. We also mention the challenges we had to tackle while doing so and the solutions we found.

2.1 Introduction

The study of stars is, like other fields of Astrophysics, challenging to approach with the traditional scientific method. Many of the hypotheses formulated about stellar objects cannot be tested in a laboratory in which one may manipulate the parameters of the experiment. Therefore, stellar physics must be pieced together from known physics, suppositions and observations. In this context, the basic theoretical tool to study the structure and evolution of stars is a stellar model.

A stellar model consists of a snapshot of the star structure at a given instant. It contains information about the chemical composition, temperature, density, luminosity, and other physical parameters as well as global values like its age. Stellar models do not need to be numerical in nature but the complexity of the differential equations describing the stellar structure means that an analytical solution is usually not achievable.

The simplest and most common numerical models are one dimensional. These models suppose radial symmetry, simplifying and speeding up the calculations. Being one dimensional, both the analytical equations and the numerical models usually divide the star in shells defined by the radius or enclosed mass,

both strictly monotonically increasing with the distance to the center of the star.

As it has been pointed out above, in this work we deal with the one dimensional stellar models of the code known as ATON (Ventura et al. 2008). Our main interest is to describe the chemical evolution of heavier than iron species in low- and intermediate-mass AGB stars through the neutron capture reaction chains known as the *s*-process. In order to solve the chemical evolution equations associated with this process in the ATON models, we have developed the post processing code SNUPPAT[1] (***s***-process **nu**cleosynthesis **p**ost **p**rocessing code for **At**on). In the next two chapters we describe how this code works in detail.

This first chapter is concerned with the discussion around the solution to the nucleosynthesis problem. In essence, this problem can be mathematically described as an initial value problem for a system of stiff ordinary differential equations. We devote the first pages of this chapter to understand the kind of problem we are tackling, and how the method used to solve it must behave. We then describe the method of our choice along with a proposed optimization before conducting a simple series of tests to ensure its accuracy.

2.2 Nucleosynthesis problem

The abundance change of a species i molar fraction (dY_i) in an AGB star due to nucleosynthesis can be described mathematically by a nonlinear system of ordinary differential equations (hereafter ODE). Using the Longland et al. (2014) notation, this system can be written as:

$$\begin{aligned}\frac{dY_i}{dt} = &\sum_j N_i \lambda_j Y_j + \sum_{jk} \frac{N_i}{N_j! N_k!} \rho N_A \langle \sigma v \rangle_{jk} Y_j Y_k + \\ &+ \sum_{jkl} \frac{N_i}{N_j! N_k! N_l!} \rho^2 N_A^2 \langle \sigma v \rangle_{jkl} Y_j Y_k Y_l,\end{aligned} \tag{2.2.1}$$

where the molar fraction Y_i is related to the mass fraction X_i through the atomic mass A_i by the expression $\mathrm{Y}_i = \mathrm{X}_i/\mathrm{A}_i$. The other variables in Eq. (2.2.1) are N_i, an integer that represents the number of species i that is produced or consumed in the reaction; λ_i, the decay rate for species i; ρ, the density; N_A, Avogadro's number; and $\langle \sigma v \rangle_{jk}$, the cross section for species j and k in a two-body reaction, with $\langle \sigma v \rangle_{jkl}$ being the equivalent for three species.

These equations depend explicitly on the density and, through the reaction rates, on the temperature. With those two values and the initial abundances we

[1] https://github.com/AndresYague/Snuppat.git

can solve them numerically for any given time interval Δt to find the abundance change.

2.2.1 Stiffness and stability

When describing nucleosynthesis processes, the equations (2.2.1) behave as a stiff system of ODE. While stiffness is an ill-defined concept in theory, in practice it means that the different components of the system evolve with timescales which may differ in orders of magnitude. This, in turn, means that not every numerical scheme is suited to solve it. As a practical definition of stiffness and an illustrative example of why the numerical scheme has to be carefully considered, we briefly study the properties of the Euler method for a simple equation.

In general, to solve the initial value problem

$$\begin{aligned} y(t_0) &= y_0 \\ y' &= f(y), \end{aligned} \tag{2.2.2}$$

the explicit Euler method can be written as

$$\begin{aligned} y_0 &= y(t_0) \\ y_{n+1} &= y_n + hf(y_n), \end{aligned}$$

where h is the chosen, fixed time step for the integration and y_n represents the numerical approximation to the real solution at time $t_n = nh + t_0$. These equations, when applied to the specific ODE

$$y' = f(y) = \lambda y \tag{2.2.3}$$

with $\lambda \in \mathbb{C}$, can be written in the closed form

$$\begin{aligned} y_0 &= y(t_0) \\ y_n &= y_0(1+z)^n \end{aligned}$$

where $z = \lambda h$. This closed form allows for a direct analysis of the numerical solution behavior at the nth step. A clear limitation of the method arises when considering $\mathrm{Re}(\lambda) < 0$[2]. In this case, the analytical solution $y_0 \exp(\lambda \Delta t)$ always

[2]In order to be as general as possible, these analysis are usually conducted considering λ as a complex number. However, once the solution is obtained it is possible to divide it in an oscillating factor, which corresponds to the imaginary part of λ, and in an exponentially growing or decreasing factor, which corresponds to the real part of λ. Given that the stability problems are defined specifically for the decreasing factor, we are only interested in the real part of λ, and only when it is negative.

tends to zero, while the numerical solution may diverge if $|1 + z| > 1$. We can, therefore, establish a working definition of the stability region for the explicit Euler method as those points that are the solution to the inequality

$$|1 + z| \leq 1, \tag{2.2.4}$$

which, when $z \in \mathbb{R}$, restricts the time step h to

$$h \leq h_{max} = \frac{2}{|\lambda|}.$$

These stability considerations are extremely limiting when tackling a stiff system of equations such as Eq. (2.2.1) due to the large disparity in evolutionary times. As an example, in normal conditions ^{14}C decays into ^{14}N following Eq. (2.2.3) with $\lambda \approx -10^{-4}$ years^{-1}, while free neutrons decay with $\lambda \approx -10^{-3}$ s^{-1}. Stability restrictions demand that when following both species simultaneously the smallest h_{max}, which in this case is $h_{max} \approx 2 \times 10^3$s, limits the time step. While this restriction is reasonable when following neutrons, it means that around 10^7 steps are needed to see a drop of a 10% in the ^{14}C abundance from its initial value.

A solution to this obstacle is the use of implicit methods. For example, a similar stability analysis for the implicit Euler method, which can be written as

$$\begin{aligned} y_0 &= y(t_0) \\ y_{n+1} &= y_n + hf(y_{n+1}), \end{aligned}$$

yields the stability requirement

$$|1 - z| \geq 1. \tag{2.2.5}$$

This requirement is trivially met for any $h > 0$ when $\mathrm{Re}(\lambda) < 0$. In this case the time step would only be limited by accuracy considerations and not by the behavior of the solution, as illustrated in Figure 2.1.

It should be noted that even when both Eq. (2.2.4) and Eq. (2.2.5) have been derived from the single linear ODE (2.2.3), their validity for the system of ODE

$$y' = Ay \tag{2.2.6}$$

with A a constant rates matrix, is justified as long as λ represents A eigenvalues with $\mathrm{Re}(\lambda) < 0$. This last assertion is straightforward to prove when A can be transformed into a diagonal matrix D, with Eq. (2.2.6) written as

$$x' = Dx,$$

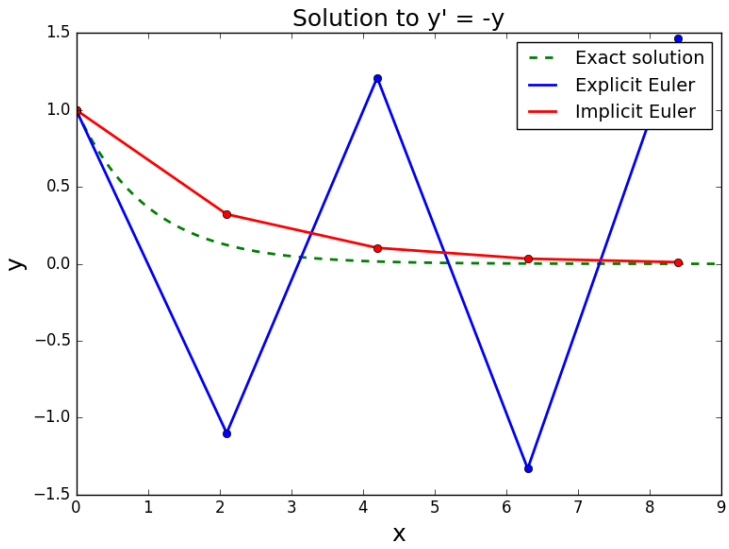

FIGURE 2.1— Solution to $y' = -y$ from both the implicit and explicit Euler methods with $h = 2.1$, which is over the stability limit of $h_{max} = 2$ for the explicit Euler method. It can be seen that the implicit method remains stable, behaving like the analytical solution.

transforming the coupled system of ODE into n independent ODE. The solution for each x_i is given by

$$x_i = x_{i0} e^{\lambda_i \Delta t}$$

where λ_i are the diagonal elements of D or A eigenvalues.

2.2.2 Semi-implicit mid-point scheme

Now that the need for an implicit scheme has been established, we turn to the literature to look for a suitable method for our problem. Among the available schemes (Longland et al. 2014) we have decided to use the Bader-Deuflhard method (Bader & Deuflhard 1983) due to its simple implementation, its automatic time step monitoring, and relative computational inexpensiveness.

The Bader-Deuflhard method (henceforth the BD method) is a semi-implicit mid-point scheme tailored for stiff systems and adapted from the explicit Gragg-

Bulirsch-Stoer (GBS) algorithm (Bulirsch & Stoer 1966). Both the GBS algorithm and the BD method generalize the mid-point scheme, dividing the basic integration step of size H into m equally spaced smaller sub-steps of size $h = H/m$.

For the initial value problem expressed by Eq. (2.2.2), the BD method implementation can be written as (see Bader & Deuflhard 1983)

$$\begin{aligned} \Delta_0 &= (I - hJ_{y_0})^{-1} hf(\eta_0) \\ \Delta_k &= \Delta_{k-1} + 2(I - hJ_{y_0})^{-1}[hf(\eta_k) - \Delta_{k-1}] \\ \Delta_m &= (I - hJ_{y_0})^{-1}[hf(\eta_m) - \Delta_{m-1}] \\ \eta(H,h) &= \eta_m + \Delta_m, \end{aligned} \tag{2.2.7}$$

where $k = 1, ..., m-1$; $\eta_0 = y_0$, $\eta_k = \eta_{k-1} + \Delta_{k-1}$, I is the identity matrix, J_{y_0} is the Jacobian df/dy calculated at y_0, and $\eta(H,h)$ is the approximate solution of Eq. (2.2.2) at $t = t_0 + H$ with time step h.

The BD method stability can be justified from the closed forms derived by Bader & Deuflhard (1983) that arise when applying it to Eq. (2.2.6)

$$\begin{aligned} \eta_{2l-1} &= \frac{1}{1-z}\left(\frac{1+z}{1-z}\right)^{l-1} y_0 \\ \eta_{2l} &= \left(\frac{1+z}{1-z}\right)^{l} y_0 \\ \bar{S}_{2l} &= \frac{1}{(1-z)^2}\left(\frac{1+z}{1-z}\right)^{l-1} y_0, \end{aligned}$$

where $\bar{S}_{2l}$ represents the closed form of the final step[3] $\eta(H,h)$. It can be seen that when $\mathrm{Re}(z) < 0$ all three quantities remain bounded by y_0. Moreover, as $\mathrm{Re}(z) \to -\infty$ we have that $\bar{S}_{2l} \to 0$. This property of the solution is known as strong absolute stability.

Clearly, these closed forms can only be applied when A is constant. When dealing with a nonlinear system such as Eq. (2.2.1) the eigenvalues are a function of the y and, in general, change as the system evolves within a basic integration step. A discussion on the stability of this method for stiff systems can be found in Hairer et al. (1982). These authors prove that the $\bar{S}_{2l}$ remain stable as well for nonlinear systems of equations.

[3] A careful reader will note that the number of steps in Eq. (2.2.7) is actually m + 1. This is due to the extra *smoothing* step $\bar{S}_{2l}$ taken at the end. The rationale for this extra step can be understood from the stability properties described here.

2.2.3 Richardson extrapolation

The BD method is completed by a dynamic order increase and automatic accuracy monitor through the application of a Richardson extrapolation. The underlying idea for this technique comes from the basic assumption that the global discretization error can be written as a polynomial of the time step h. This assumption holds for the BD method, where the numerical approximation to the solution of the initial value problem (2.2.2), $\eta(H,h)$, can be expressed as

$$\eta(H,h) = y(H) + g_1(H)\cdot h^2 + g_2(H)\cdot h^4 + ... \tag{2.2.8}$$

where the g_i are in general functions of H, and $y(H)$ represents the exact solution at $t = t_0 + H$ (see Deuflhard 1983). The idea is then to solve the ODE more than once with different values of h, obtaining a sequence with which the method order can be increased.

As an example, if we solve again for $h' = h/2$, we can express the solution as

$$\eta(H,h/2) = y(H) + g_1(H)\cdot h^2/4 + g_2(H)\cdot (h/2)^4 + ...$$

which, when combined with the previous solution, can be extrapolated to a higher order approximation of $y(H)$

$$\frac{4\eta(H,h/2) - \eta(H,h)}{3} = y(H) + g_2'\cdot (h/2)^4 + ...$$

The above extrapolation is generalized for any sequence of $h_i = H/n_i$ in the expression (see Bader & Deuflhard 1983)

$$T_{ik} = T_{ik-1} + \frac{T_{ik-1} - T_{i-1k-1}}{\left(\frac{n_i}{n_{i-k+1}}\right)^2 - 1}, \tag{2.2.9}$$

where the $T_{i1} = \eta(H,h_i)$ are the solutions given by the numerical scheme, and with each particular choice of coefficients n_i defining a specific extrapolation sequence. For the BD method the authors select the series

$$n_i = \{2,6,10,14,22,34,50,70,...\}$$

due to numerical considerations. With the basic assumption that the high order approximations are more accurate than the lower order ones, the error of the extrapolation T_{kk-1} is taken as the difference between itself and its successive extrapolation

$$\epsilon_k = ||T_{kk-1} - T_{kk}|| \tag{2.2.10}$$

where the choice of the scaled norm to be applied is left to the user.

This error is then used to predict the size of the following time step as (see Longland et al. 2014)

$$H_k = H \left(\frac{\text{eps}}{\epsilon_k} \right)^{\frac{1}{2k+1}}, \tag{2.2.11}$$

where eps represents the required accuracy by the user. An intuitive explanation to the expression above is that when $\epsilon_k < \text{eps}$, it means that the code is over performing for the required accuracy, taking more steps than necessary and wasting computing cycles. Therefore, we are interested in increasing the time step H in order to reduce the steps taken to a minimum compatible with the imposed accuracy.

Further consideration is given by Deuflhard (1983) and Longland et al. (2014) to the computational effort needed to complete an integration with the H_k calculated above so as to select the optimal order k. We find this consideration useful even when one of our methods is functionally non-deterministic in the number of operations used. Therefore, we briefly describe it in Subsection 2.2.5.

Finally, we can now check the stability properties of the T_{ik}. We already saw that for a general, nonlinear system, the $\bar{S}_{2l} = T_{i1}$ were proven stable by Hairer et al. (1982). This means that we can move our attention to the stability properties of the remaining extrapolations T_{ik} with $1 < k \leq i$. Fortunately, Hairer et al. (1982) also prove that T_{22}, T_{32}, and T_{33} are always stable for any H. Furthermore, they manage to prove that the remaining T_{ik} are stable as long as H is not *too small*, with the limiting value depending on the system of equations being solved. Although this condition may seem arbitrary, we should remember that if H is small enough we may find a solution within our accuracy criterion by T_{33}. Otherwise, the unstable nature of the subsequent extrapolations will prevent convergence, forcing us to lower the time step H until an accurate enough solution is found by the third order.

2.2.4 Gauss-Seidel method

Before detailing the algorithmic realization of the BD scheme, we briefly discuss the merits of using the Gauss-Seidel (GS) iterative method in SNUPPAT. The GS method (Seidel 1874) can be used under specific circumstances to solve for the array x in the linear system

$$Ax = b$$

without operating on the matrix A. Our interest in this method stems from the fact that a large fraction of SNUPPAT computation effort is spent in the solution of the linear system

$$(I - hJ_{y_0})x = b,$$

which appears in Eq. (2.2.7), with a different array b per step. In fact, the general step for Δ_k can be written as

$$(I - hJ_{y_0})(\Delta_k - \Delta_{k-1}) = 2[hf(\eta_k) - \Delta_{k-1}].$$

The method itself consists on the successive updates of an array solution u (Trujillo & Fabiani 1995)

$$u_i^{new} = u_i^{old} + \frac{1}{a_{ii}}\left(b_i - \sum_{j=1}^{i-1} a_{ij}u_j^{new} - \sum_{j=i}^{N} a_{ij}u_j^{old}\right) \tag{2.2.12}$$

until a desired level of accuracy given by the difference $\epsilon = ||Au - b||$ is achieved.

Knowledgeable readers may point out that a LU decomposition[4] is preferable for this kind of problem over an iterative procedure. This kind of decomposition is particularly useful when one wants to solve a number of linear systems with the same matrix A and a changing array b. The basic idea is to factorize the matrix A into two matrices: a lower triangular matrix L and an upper triangular matrix U. After performing the decomposition, the two linear systems

$$\begin{aligned} Ly &= b \\ Ux &= y \end{aligned}$$

can be trivially solved with

$$\begin{aligned} y_i &= \frac{1}{l_{ii}}\left(b_i - \sum_{j=1}^{i-1} l_{ij}y_j\right) \\ x_i &= \frac{1}{u_{ii}}\left(y_i - \sum_{j=i+1}^{N} u_{ij}x_j\right). \end{aligned} \tag{2.2.13}$$

Because the L and U matrices depend only on A, as long as it remains unchanged one does not need to compute again the costly factorization operation

[4]The name comes from the lower (L) and upper (U) matrices in which A is factorized into, expressed by A = LU. Hence, LU decomposition.

and may apply the cheap backwards and forwards substitution for any desired b. This objection is strengthened by noting that Eqs. (2.2.12) and (2.2.13) perform roughly the same number of operations on a dense matrix. Therefore, if the GS method takes too many iterations to converge, the total number of operations may offset those of the LU decomposition including the factorization.

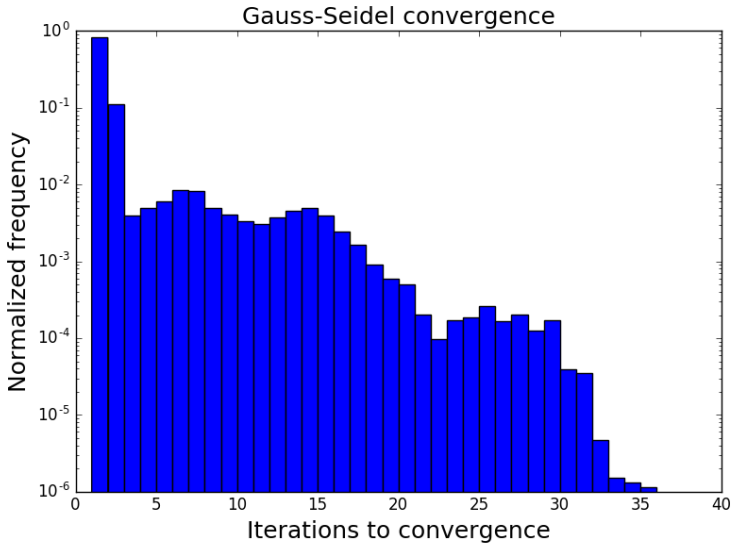

FIGURE 2.2— Histogram of normalized iterations needed by the GS method to reach convergence during a thermal pulse. In 90% of the cases this method manages to converge with less than 3 iterations, with the great majority of these (∼89%) being just one iteration. The total sample is comprised of 5.3 million iterations.

At this point in the discussion it becomes necessary to have a rough idea on the number of iterations required by the GS method to reach convergence. With that objective we set our code to solve the nucleosynthesis equations during a thermal pulse (TP) and count the number of iterations needed by the GS algorithm. The TP is selected for being the period in which the BD method needs the most steps (Longland et al. 2014). The results of this simple experiment are shown in Figure 2.2, where it can be seen that in most of the cases the GS method needs just one iteration to reach the desired accuracy.

Therefore, most of the time using the GS scheme over the LU factorization results in a less time consuming integration.

Up to this point we have compared both methods under the assumption that we were operating on a dense matrix. However, the Jacobian of the system (2.2.1) is sparse, which means that most of the matrix consists of zeros with only a handful of nonzero terms (which in our case, are usually near the main diagonal). Intuitively, most of the species rates would only depend on the nearest ones[5], with the exception of neutrons, protons and alpha particles. This means that when solving both Eqs. (2.2.12) and (2.2.13), the number of operations grows with $\sim mN$, with m being a rough estimation of the number of nonzero elements in each line of the matrix. This becomes important when considering that when doing a LU factorization on a sparse matrix there are some initially zero elements that become nonzero during the operation, known as fill-ins. These fill-ins may change the m in the estimation above, potentially making Eq. (2.2.13) more expensive than Eq. (2.2.12).

Finally, as it must be done with every iterative scheme, we discuss the convergence criterion of the GS method. For non symmetric matrices, the sufficient condition for the GS algorithm convergence is strict diagonal dominance (Bagnara 1995). A matrix is defined as strictly diagonal dominant if the inequality

$$|a_{ii}| > \sum_{k \neq i} |a_{ik}|$$

holds for all i. Which when applied to our matrix $A = I - hJ_{y_0}$ requires that

$$|1 - hj_{ii}| > \sum_{k \neq i} |hj_{ik}|$$

for all i. Considering that there are no reactions that depend on element i and produce it at the same time, we know that $j_{ii} \leq 0$. This allows us to factor out h and rewrite the strict diagonal dominance criterion as

$$1 > h \left(j_{ii} + \sum_{k \neq i} |j_{ik}| \right).$$

At first glance this expression appears to impose a limit on h any time the parentheses is positive, seemingly negating the advantages of using an implicit

[5]Near here is meant in the table of nuclides sense. At any rate, the exact structure of the Jacobian is highly sensible to the species ordering in the code. As an example, a good strategy is to pack the most dense rows and columns together. Which can be achieved by indexing neutrons, protium and ^{4}He consecutively.

method as discussed before. However, we must recall that this condition is sufficient but not necessary for convergence. This means that even when the criterion does not hold, which is often, we can use the GS method regardless and simply limit the iterations to a maximum. This approach is no different to the one we take when convergence is guaranteed because the other critical piece of information, convergence speed, needs the costly knowledge of the system eigenvalues. Therefore, the GS method is always tried first until the limit of iterations is reached. When it does, we can either reduce the time step and try again or use the more reliable LU decomposition.

2.2.5 Algorithm

In the interest of clarity, now follows a description of the actual implementation of the BD method in SNUPPAT.

As we have previously discussed, a one dimensional stellar model is usually structured in mass shells, each one with parameters such as the temperature, the density or the chemical composition. These shells are identified by the enclosed mass of the star below and up to it, with the exact center being 0. The evolution of a single star can be followed as the succession of several stellar models. We can understand the age difference between a model and the next one as the time it takes for the star to transition from the state described by the first of these models to the second one. Calling this time H_{tot} we can apply the equation (2.2.1) to each one of the model mass shells individually, following its chemical evolution.

In order to apply the scheme (2.2.7), the algorithm starts by calculating the shell Jacobian for the initial abundance

$$J_{y_0} = \left.\frac{df_i}{dy_j}\right|_{y_0},$$

where f_i represents the rate of species i, or dy_i/dt. Taking into account that most of the rates depend on a handful of species -namely protons, neutrons, alpha particles, and some species with similar mass to i-, the Jacobian is mostly comprised of zeros. In our algorithm we take advantage of this sparsity by keeping an updated record of the indices at which the Jacobian is non-zero and acting only on them in subsequent iterations. This approach saves a considerable amount of time both in floating-point and in memory access operations.

While the Jacobian has to be calculated only once per basic integration step, each one of the refinements $T_{i1} = \eta(H, h_i)$ requires a different h_i and, therefore, the matrix

$$A = I - h_i J_{y_0}$$

must be recalculated at the beginning of each application of Eq. (2.2.7).

After obtaining the first two solutions $\eta(H, h_1)$ and $\eta(H, h_2)$ through the BD method, we can start extrapolating and calculating the associated errors. As the expression (2.2.10) describes, each one of the errors ϵ_k is a scalar quantity obtained from applying a scaled norm to the difference $T_{kk-1} - T_{kk}$. We use an euclidean norm and normalize the error in a similar fashion to Longland et al. (2014)

$$\epsilon_k = \sqrt{\frac{1}{N}\sum_{i=1}^{N}\left(\frac{T^i_{kk-1} - T^i_{kk}}{\max(|T^i_{kk-1}|, y_{scale})}\right)^2} \tag{2.2.14}$$

where y_{scale} represents a minimum considered abundance to avoid numerical problems. It is worth mentioning that we are scaling with T_{kk-1} instead of y_0 to avoid two scenarios: one where the error is not accounted for, if $T^i_{kk-1} << y^i_0$ and other where the error is inflated if $y^i_0 << T^i_{kk-1}$. These scenarios represent a fast decrease or increase, respectively, in the abundance of the species i. Finally, let us briefly consider the extreme in which all errors but one are zero, and analyze the ϵ_k behavior. In this case, calling the scaled error γ, we have that

$$\epsilon_k = \gamma\sqrt{\frac{1}{N}}.$$

For the typical case of the number of species $N \in \{10^2, 10^3\}$, this means that γ is divided by a factor of 10 to 30. Therefore, if asking for an accuracy of eps $= 10^{-5}$, the biggest relative error that Eq. (2.2.14) would not be able to detect can go from a 0.01% to a 0.03% in the unlikely event that every other abundance is exact.

If at any point during the integration $\epsilon_k <$ eps, we stop the calculations and accept the associated T_{kk-1} as the solution for the given H with the value $k_f = k$ as our maximum order. Then, if the solution for H_{tot} has not been yet obtained, we calculate the new H through Eq. (2.2.11) by using the k that is associated with the minimal computational error per unit of time. According to Deuflhard (1983), this work per order W_k can be expressed as

$$W_k = a_{k+1}\sqrt[2k+1]{\frac{\epsilon_k}{\text{eps}}},$$

where the a_k are calculated from the recursion

$$a_1 = c_J + c_{LR} + (n_1 + 1)(c_f + c_s)$$
$$a_k = a_{k-1} + n_k(c_f + c_s) + c_{LR} + c_s$$

with c_f being the cost per f-evaluation, c_J the cost of evaluating the Jacobian matrix, c_s the cost of backward and forward substitution, and c_{LR} the cost of a LU decomposition. Given that we are using an iterative method, most of these coefficients will be an estimation at best. In our case we know $c_{LR} = c_J = 0$. From some numerical experiments we also know that the code spends a 50% of the time in the GS method and a 35% of the time in f-evaluation. Therefore, we have selected $c_f = 7$ and $c_s = 10$.

After calculating the minimum W_k, we can use the associated ϵ_k in Eq. (2.2.11) to estimate the next time step. If the selected k is k_f, then we consider the possibility of an order increase. This is done by estimating the ϵ_{k_f+1}, for which Deuflhard (1983) provides us with

$$\epsilon_{k_f+1} = \mathrm{eps}^{\frac{a_{k_f+1}-a_1+1}{a_{k_f+2}-a_1+1}}. \tag{2.2.15}$$

This estimated error is then used in Eq. (2.2.11) only if $a_{k_f+1} \cdot \epsilon_{k_f+1} > a_{k_f+2}$.

On the other hand, if at no point during the integration there is an ϵ_k which goes below eps, H is reduced and the integration is tried again. This procedure is followed as well if there is a convergence problem during the GS method or any of the Δ_k or $\eta(H, h_k)$ contains a clearly divergent value.

2.2.6 Unconditionally stable explicit Patankar-Euler algorithm

We now briefly describe what appears to be a powerful and simple algorithm rarely used in stellar nucleosynthesis calculations. So much so that our specific application does not appear to be described in the literature. Because the algorithm we are describing here has the same structure as the BD method, we focus on describing the differences in the only three expressions that change.

The first expression we have to modify is the core integration method itself. Instead of a semi-implicit take on the modified mid-point rule (2.2.7), we use a scheme from the Patankar family (see e.g., Burchard et al. 2003, 2005). These schemes are well suited to solve systems of production-destruction equations, such as the nucleosynthesis ODE. In particular, we use the method known as the Patankar-Euler scheme, which is described by

$$y_{n+1} = y_n + h\left(K_n - D_n y_{n+1}\right), \tag{2.2.16}$$

where h is the selected time step, and K_n and D_n are the values at y_n of the

functions $K(y)$ and $D(y)$, defined by[6]

$$y' = f(y) = K(y) - D(y)\, y,$$

with $K, D \geq 0$.

By rearranging Eq. (2.2.16) we obtain

$$y_{n+1} = \frac{y_n + hK_n}{1 + hD_n}, \tag{2.2.17}$$

which allows us to readily derive three properties of this method that makes it surprisingly well suited to solve the nucleosynthesis equations.

The first property is that this scheme is absolutely stable, with the stability value being K_n/D_n. Indeed, if we are to take the limit of Eq. (2.2.17) when $h \to \infty$, it is clear that $y_{n+1} \to K_n/D_n$. Additionally, if $y_n = K_n/D_n$, then $y_{n+1} = K_n/D_n$ for any positive value of h. This means that, as long as $D_n > 0$, the method does not diverge.

The second property is that the method is non-negative. Indeed, for any $y_n \geq 0$ and assuming $h > 0$ it is trivial to show that $y_{n+1} > 0$.

The third and most important property is that the Patankar-Euler scheme is explicit in practice, allowing us to avoid the computationally expensive solution of a linear system of equations. The amount of work saved by this fact cannot be overstated (see Figure 2.3), and compensates more than enough for the shortcomings associated with being a derivation of an Euler method. This is, a global discretization error that contains every power of h instead of only odd powers like in the expression (2.2.8), as we explain further in the text.

We can easily extend Eq. (2.2.17) to a multistep scheme by consecutively applying it until a global time step $H = nh$ is reached. Much like with the BD method, we can then compute the solution for an array of values n_i and extrapolate to increase the accuracy through the use of a Richardson Extrapolation.

By employing a bit of algebra in this multistep scheme we find that the numerical solution after a global step H, with the usual assumptions and notation, can be expressed as

$$\eta(H, h) = y(H) + g_1(H) \cdot h + g_2(H) \cdot h^2 + g_3(H) \cdot h^3 + ...$$

The fact that every power of h is present means that we need twice as many steps to arrive to the same order as the BD algorithm. To this end, we have

[6] Here we are modifying the typical notation for Patankar-type schemes, where we assume that the sink term can be expressed in the form $D(y)\, y$. This is always true for the nucleosynthesis equations.

decided to use the Bulirsch-Stoer sequence

$$n_i = \{2, 3, 4, 6, 8, 12, 16, 24, ...\},$$

defined by the iterative expression $n_{i+2} = 2n_i$. This particular sequence was selected in account of it being the fastest one in a handful of empirical tests.

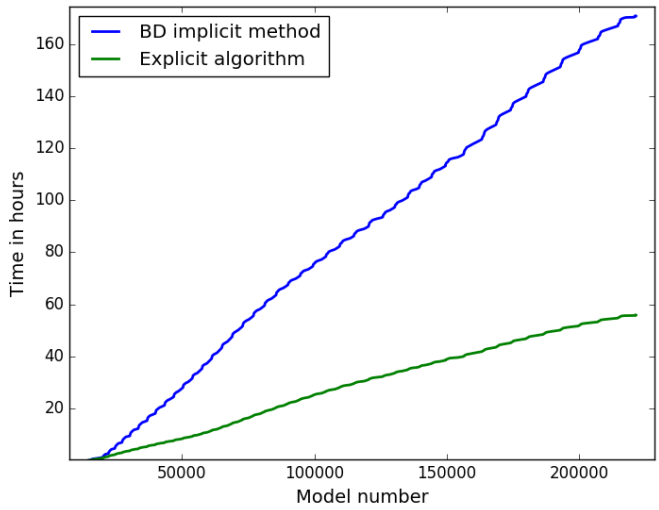

FIGURE 2.3— Comparison between the computation times for the BD method (in blue) and the explicit algorithm described in this Subsection (in green) for a real 4 $M_\odot$ complete simulation. This simulation was run with 10 CPU and a maximum of 8 and 16 substeps per global time step for the BD method and the explicit algorithm, respectively.

From here we only need to tweak two more expressions from the BD method in order to complete the algorithm. The first of these expressions is the rational extrapolation (2.2.9). Here we use instead

$$T_{ik} = T_{ik-1} + \frac{T_{ik-1} - T_{i-1k-1}}{\frac{n_i}{n_{i-k+1}} - 1},$$

with the only difference being that the square in the denominator has disappeared. The second expression is the step size predictor (2.2.11), which trans-

forms into

$$H_k = H\left(\frac{\text{eps}}{\epsilon_k}\right)^{\frac{1}{k+1}}.$$

Although the stability and non-negativity properties translate directly into the multistep form of the scheme, the same cannot be confidently said about the solutions obtained from the Richardson Extrapolation. Indeed, we have not yet explored the stability considerations of the extrapolated values. In practice, however, this algorithm appears to be at least as stable as the BD method.

In Figure 2.3 we show the acceleration factor of this explicit scheme over the DB method with a real simulation of a 4 $M_\odot$ model. From this figure we can see that after an initial period in which both methods are equally fast, they soon diverge, with the DB method being consistently slower than the explicit algorithm by a factor of around 3.

Although we still lack a comprehensive theory backing the stability considerations of the extrapolated solutions, it is clear that a more profound analysis of this scheme and the Patankar type methods is more than justified.

2.3 Tests

Even with a solid theoretical background, every code must be tested to check that it delivers the correct solutions to the problems it aims to solve. Of course, to completely test a code that probes our understanding is difficult to say the least. However, we can test its individual parts to check that they work correctly. If they do, we expect the whole process to yield an accurate representation of reality.

2.3.1 Bader-Deuflhard test

The first thing we must test is the integration method. In order to do that we are going to solve two stiff systems of equations for which we have the analytical solution. First, we are going to solve the linear system of equations

$$\begin{aligned}\frac{dx}{dt} &= -\lambda x \\ \frac{dy}{dt} &= \lambda x - \gamma y\end{aligned} \tag{2.3.1}$$

with λ, $\gamma > 0$. This system represents the evolution of the decaying species x and y with the first decaying into the second. We know that the solution to

this system is

$$x = x_0 \mathrm{e}^{-\lambda t}$$
$$y = \frac{\lambda}{\gamma - \lambda} x_0 \left(\mathrm{e}^{-\lambda t} - \mathrm{e}^{-\gamma t} \right) + y_0 \mathrm{e}^{-\gamma t},$$

where $x_0 = x(0)$ and $y_0 = y(0)$. Among the many cases we may study, we have chosen one in which $\lambda >> \gamma$. With this choice we are intuitively looking for a fast initial transition period followed by a slower exponential decay in order to gauge the code response to such situations. In fact, under this assumption we have that the solution to the system reduces to

$$x = x_0 \mathrm{e}^{-\lambda t}$$
$$y = x_0 \left(\mathrm{e}^{-\gamma t} - \mathrm{e}^{-\lambda t} \right) + y_0 \mathrm{e}^{-\gamma t}.$$

If we suppose that the whole x evolution takes place fast enough that there is no time for y to evolve, we can describe y evolution as an exponential grow from y_0 to $x_0 + y_0$ at the rate of λ followed by an exponential decay to 0 at the rate γ. Giving us the test we were looking for.

In Figure 2.4 we can see a numerical solution by the BD method to the system (2.3.1) with $\lambda = 300$ and $\gamma = 1$, represented along the analytical one. We have to bear in mind that the BD method was tasked with solving the system for $t = 1$. Consequently, all the intermediate points between $t = 0$ and $t = 1$ are there because the method was not able to solve the system for the time step provided within the imposed relative accuracy of 10^{-5}. More precisely, the second point is the first for which the method was able to converge within the accuracy. The subsequent points are predictions of the method for the next converging time step. We can see that the time step becomes increasingly larger the smaller $|y'|$ and $|x'|$ become.

To complete this test we take a look at the relative difference between the numerical solution and the real solution, commonly referred to as the relative error. In Figure 2.5 we represent this error for each one of the numerical approximations given by the BD method. We can see that the maximum error appears to be around the same region where the method had to take the smaller time steps, as expected. Moreover, the value of this maximum ($\sim 2 \times 10^{-5}$) is compatible with the imposed accuracy of 10^{-5} for the global average relative error, due to the fact that the error of the other function is negligible throughout the whole integration.

For the second test of the BD method, we are going to apply it to a non-linear system of ODE; this aims to try the semi-implicit nature of the method.

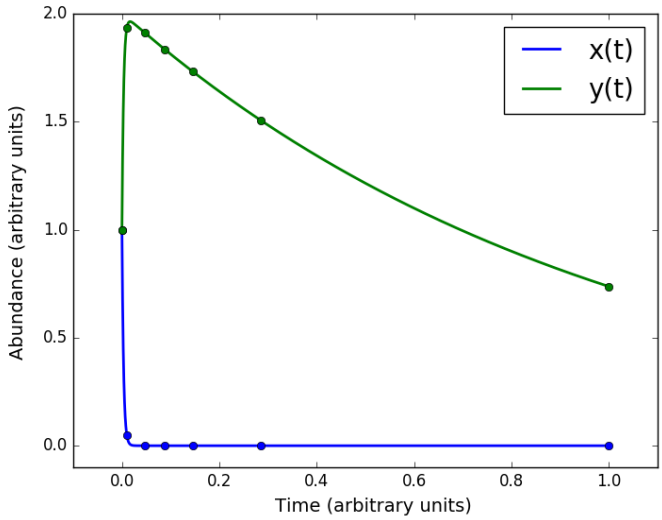

FIGURE 2.4— Solution to the system (2.3.1) with $\lambda = 300$ and $\gamma = 1$. The solid lines represent the analytical solution, while the dots mark the numerical solution obtained with the BD method.

Although the Jacobian changes throughout the whole integration, we consider it constant within each basic integration step. For this we have selected the system

$$\begin{aligned} \frac{dx}{dt} &= -\lambda x \\ \frac{dy}{dt} &= -\sigma y x. \end{aligned} \tag{2.3.2}$$

This system does not represent a physical process that we may find inside an AGB star. However, it is not the verisimilitude of the process what is of interest to us, but its non linearity. In fact, the Jacobian for this system has the determinant

$$|J(x, y)| = \lambda\sigma x,$$

which, as expected, depends on at least one variable.

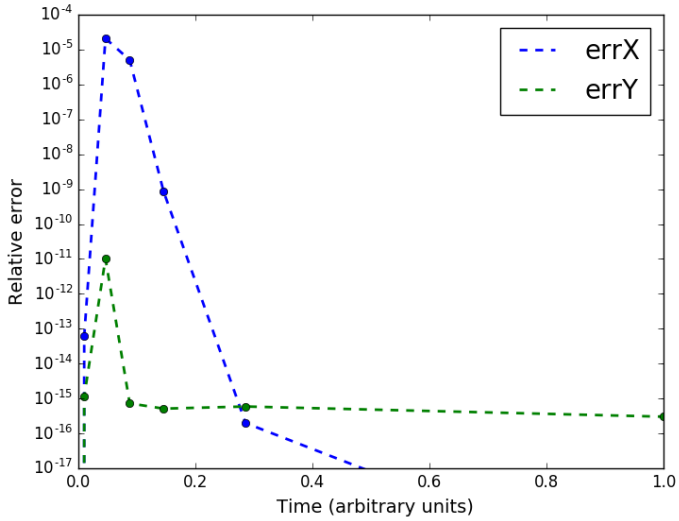

FIGURE 2.5— Relative error associated with the solution presented in Figure 2.4. The imposed accuracy for this run was 10^{-5}.

To test how the method behaves with a variable Jacobian, we set up λ so as to make x change fast within the integration. Because x' depends only on λx, we set $\lambda = 25$ and $\sigma = 5$. This way y evolves slower than x, so the change in the Jacobian can be seen on it. Both the analytical and numerical solutions for this choice are shown in figure 2.6, with the expression to the analytical solution being

$$x = x_0 \mathrm{e}^{-\lambda t}$$
$$y = y_0 \mathrm{e}^{\frac{\sigma}{\lambda} x_0 (\mathrm{e}^{-\lambda t} - 1)}.$$

As it has been already stated, the Jacobian is only calculated again after the method converges. There are four intermediate convergences during the evolution and the values of the Jacobian determinant in these points are $|J(x_0, y_0)| = 500$, $|J(x_1, y_1)| \approx 3.4$, $|J(x_2, y_2)| \approx 2 \times 10^{-1}$, and $|J(x_3, y_3)| \approx 2 \times 10^{-4}$. Moreover, the global relative error never grows above 5×10^{-6} as can be seen in Figure

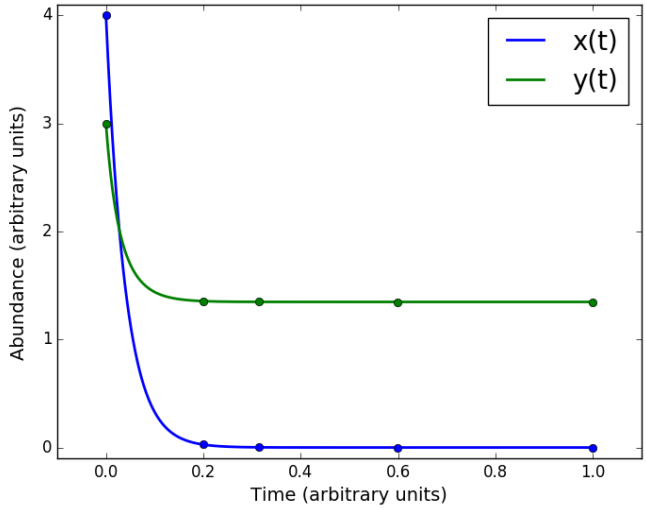

FIGURE 2.6— Solution to the system (2.3.2) with $\lambda = 25$ and $\sigma = 5$. The solid lines represent the analytical solution, while the dots mark the numerical solution obtained with the BD method.

2.7, showing that even when considering constant a fast varying Jacobian, the method works reasonably well.

2.3.2 Benchmark nucleosynthesis test

After the ideal cases with analytical solutions, we set out to test the method in a real nucleosynthesis simulation. That is, we are interested in studying how the SNUPPAT code behaves during an integration of a single radiative shell in relation to other nucleosynthesis codes. This step was made possible thanks to the help of Dr. Maria Lugaro, who provided us with the results of a 3 $M_\odot$ stellar simulation at a metallicity of z = 0.02 with ^{13}C pocket formation. These results come from the same models used by Karakas (2010) and Buntain et al. (2017), with an integration method adapted from Cannon (1993). We will refer to these results as the benchmark case hereafter.

For this test we have selected a total of 70 thousand years to be followed

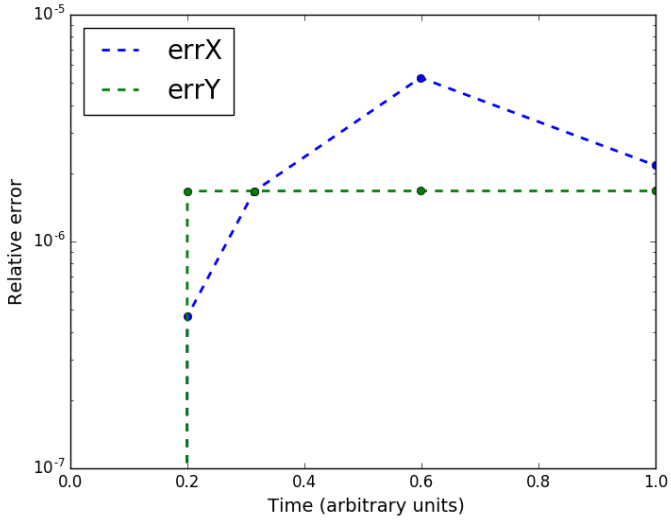

FIGURE 2.7— Relative error associated with the solution presented in Figure 2.6. The imposed accuracy for this run is 10^{-5}.

through 120 models into the formation and disappearance of a ^{13}C pocket and beginning of *s*-process nucleosynthesis. Out of a pool of 182 models, these 120 have been selected for the simple reason that beyond model 120 the pocket region is engulfed into the PDCZ, adding a convective mixing process that sits outside the scope of this test.

The integration was carried out by selecting a specific mass inside the ^{13}C pocket, and then calculating the temperature, density, and abundances by linear interpolation to that mass. After the first model, the abundance in SNUPPAT is advanced purely by integration through the BD method with the given abundances used only for comparison purposes. In figure 2.8 the relative abundance differences between the benchmark models and SNUPPAT output for the last model are shown. In that figure, it can be seen that a total of 11 species out of the 320 in the network appear to have a relative difference with the benchmark above the 50% threshold. Among these 11 species, only 3 present a difference greater than one order of magnitude: ^{54}Fe, ^{58}Ni and ^{59}Ni.

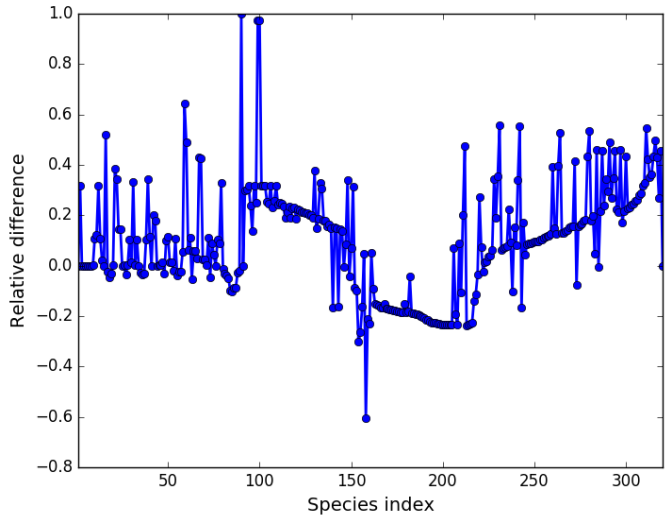

FIGURE 2.8— Relative difference between SNUPPAT results and the benchmark abundances for the last model during the test run. The species above a 0.5 absolute relative difference are ^{15}O, ^{36}Ar, ^{54}Fe, ^{58}Ni, ^{59}Ni, ^{96}Zr, ^{148}Pm, ^{155}Eu, ^{171}Tm, ^{183}Ta and ^{204}Tl. The structure present in the difference stems from the coupled nature of the abundances.

To understand where this difference may come from, we consider ^{54}Fe, which is the species with the highest relative difference. Its evolution, plotted in Figure 2.9, shows a growing discrepancy between SNUPPAT results and the benchmark value. There are only two reactions that affect ^{54}Fe in the network: $^{54}\text{Fe} + \text{n} \rightleftharpoons {}^{55}\text{Fe}$ and $^{54}\text{Fe} + \alpha \rightleftharpoons {}^{58}\text{Ni}$. Of these two reactions, only the first one in the forward direction is relevant at this temperature. There are then only two possibilities regarding the difference between the SNUPPAT and the benchmark evolutions. The first and most worrying one is that SNUPPAT may be integrating incorrectly. The second one is that the calculations are correct but the rates for the benchmark and SNUPPAT may be different enough to explain the differences.

In order to discard the first possibility, we look for evidence pointing to the second possibility. First, as a consistency test we can check the sum of the

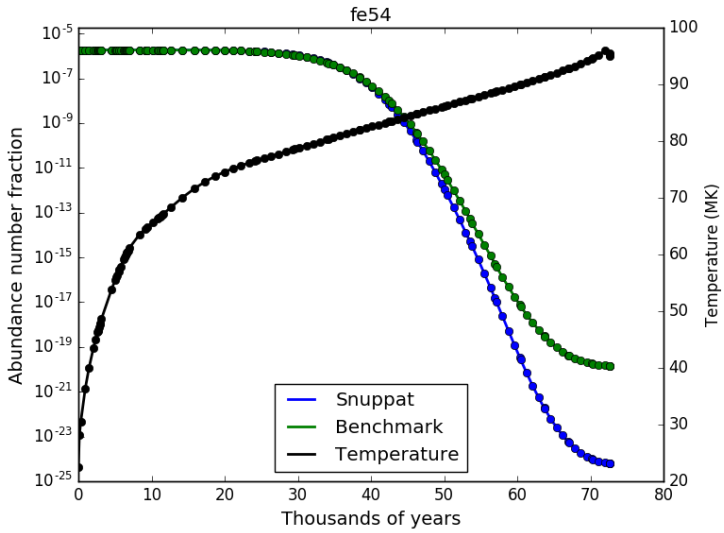

FIGURE 2.9— Evolution of ^{54}Fe during the nucleosynthesis tests. The individual dots mark the actual models.

mass fractions. From its definition, we know that this sum must be constant and equal to one throughout the whole integration. Due to numerical errors, however, this value is rarely found to be one. Nevertheless, a good indication of a consistent integration is one in which this number changes as little as possible.

In Figure 2.10 we have displayed the change in mass fraction sum throughout the whole simulation for both the benchmark and SNUPPAT results. Both curves in this Figure give us interesting information. On one hand we have that SNUPPAT results appear constant at the scale of 10^{-7}. In fact, albeit invisible due to the scale in Figure 2.10, after an initial change of 10^{-10} in the first model the SNUPPAT results show no greater deviation than 2×10^{-14}. On the other hand, the benchmark values vary within 3×10^{-7} without apparent structure. Disregarding the possibility of an incorrect integration in the benchmark code, we are left with a difference in the interpolation scheme used. That is, given that the sum of mass fractions need not to be the same in each mass coordinate, it is plausible that the shift in mesh points combined with different interpolation

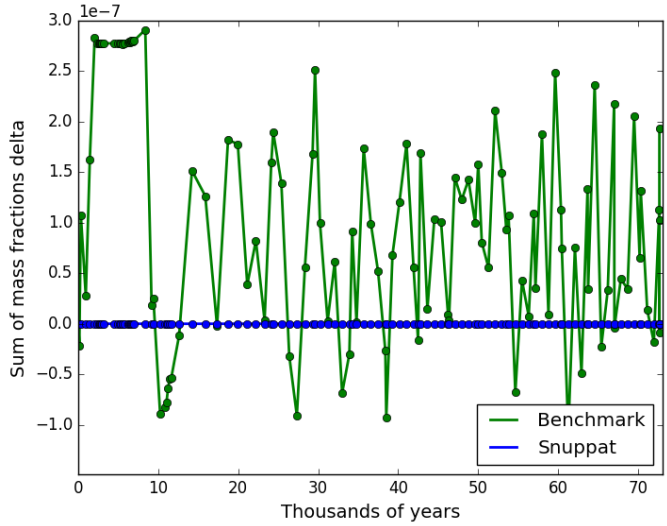

FIGURE 2.10— Evolution of the sum of mass fractions during the nucleosynthesis tests. The green benchmark line behavior is most likely due to the different interpolation techniques used.

approaches end up giving the pattern seen in the figure. Indeed, changing the interpolation method from a linear one to a third order polynomial (Steffen 1990), gives us a different pattern with a higher variation in the mass fractions sum as can be seen in Figure 2.11.

Once shown how the abundances may differ depending on of the interpolation method used, it is straightforward to argue that the same effect may be taking place with the temperature and density. As an example, the cross section for the reaction p + ^{12}C $\rightleftharpoons$ ^{13}N changes a factor 10^4 in the first six models of the simulation due to the temperature going from 22 MK to 43 MK. A small difference in this and other reaction rates may result in a change of the neutron abundance, which may help in explaining the differences seen in Figure 2.9 on the ^{54}Fe abundance.

Finally, we follow the evolution of the proton abundance for the first few models of the test and see how well SNUPPAT conforms to the theory. We

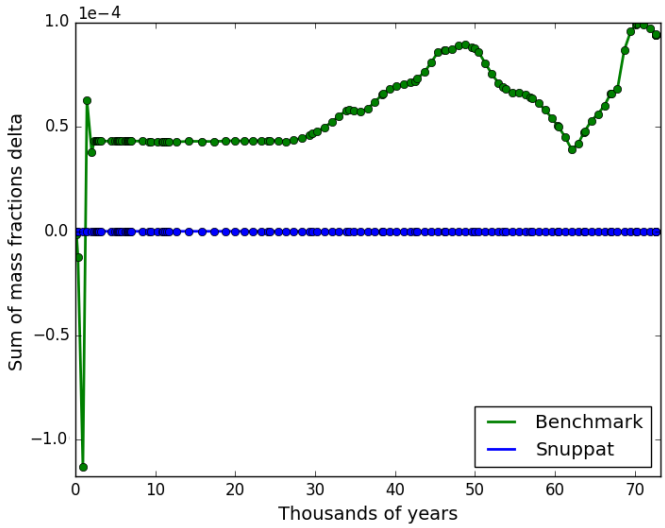

FIGURE 2.11— Evolution of the sum of mass fractions during the nucleosynthesis tests. Here we are using a third order polynomial instead of a linear function to interpolate between mass shells and models.

have selected to follow the protons for three main reasons. The first one is that the exact evolution of this species is critical for the formation of the ^{13}C and ^{14}N pockets and, therefore, for the neutron abundance available for *s*-process nucleosynthesis. The second reason is that for these steps the proton abundance depends mainly on only two reactions, p + ^{12}C $\rightleftharpoons$^{13}N and p + ^{13}C $\rightleftharpoons$^{14}N. The third reason is that, as can be seen in Figure 2.12, the benchmark and SNUPPAT values differ significantly between the fifth and eighth steps. Therefore, if there is an error on how SNUPPAT performs its calculations, it would be easier to find it there.

For these reasons we are analyzing the SNUPPAT integration from the fifth to the sixth steps of the simulation. In order to do that, we must describe in detail all the values pertinent to the test. First, the cross sections we are using are fitted to the parametrization found in, for example, Cyburt et al. (2010) for the JINA REACLIB database. This function is described by a set of seven

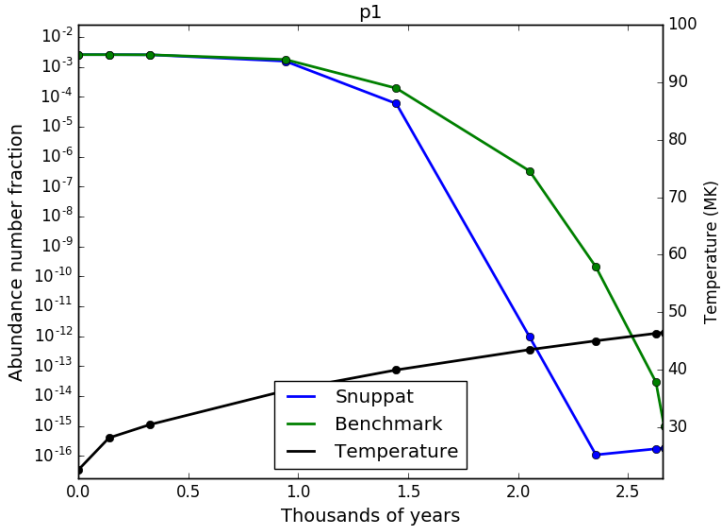

FIGURE 2.12— First few steps of the proton evolution during the nucleosynthesis test. The integration from the fifth to the sixth step is analyzed in the text.

parameters and, given a temperature, the cross section can be calculated with

$$\sigma = \exp(a_1 + a_2 T_9^{-1} + a_3 T_9^{-1/3} + a_4 T_9^{1/3} + a_5 T_9 + a_6 T_9^{5/3} + a_7 \ln T_9)$$

where the a_i are the fitted function coefficients and T_9 is the temperature in units of GK. For the proton capture reaction by ^{12}C, the coefficients we are using are a_i = {17.1, 0, -13.7, -0.0231, 4.44, -3.16, -0.667}. For the proton capture by ^{13}C, the coefficients we are using are a_i = {18.5, 0, -13.7, -0.0450, 3.70, -1.71, -0.667}.

The final pieces we need to do the calculation by hand are the ^{12}C and ^{13}C abundances, as well as the time step, the density and temperature. The $Y_{^{12}C}$ remains fairly constant during the integration, with similar values to those of the benchmark simulation. Specifically, we have that $Y_{^{12}C} = 0.02$ mol/g. On the other hand, $Y_{^{13}C}$ changes during the integration and, depending on the selected values for temperature and density, may have a different initial value at the fifth step. Regarding the temperature and density values we already

T_6	ρ	$Y_{^{13}C}$	σ_1	σ_2	Theory	SNUPPAT
40.1	14.0	1.82×10^{-3}	1.12×10^{-9}	3.66×10^{-9}	3.71×10^{-5}	3.71×10^{-5}
40.5	14.6	1.84×10^{-3}	1.25×10^{-9}	4.10×10^{-9}	1.47×10^{-5}	1.47×10^{-5}
40.8	15.3	1.86×10^{-3}	1.40×10^{-9}	4.57×10^{-9}	4.99×10^{-6}	5.01×10^{-6}
41.2	15.9	1.86×10^{-3}	1.56×10^{-9}	5.10×10^{-9}	1.43×10^{-6}	1.44×10^{-6}
41.6	16.5	1.86×10^{-3}	1.73×10^{-9}	5.68×10^{-9}	3.36×10^{-7}	3.38×10^{-7}
41.9	17.1	1.86×10^{-3}	1.93×10^{-9}	6.32×10^{-9}	6.30×10^{-8}	6.36×10^{-8}
42.3	17.7	1.86×10^{-3}	2.14×10^{-9}	7.02×10^{-9}	9.21×10^{-9}	9.30×10^{-9}
42.6	18.4	1.86×10^{-3}	2.38×10^{-9}	7.79×10^{-9}	1.01×10^{-9}	1.02×10^{-9}
43.0	19.0	1.86×10^{-3}	2.64×10^{-9}	8.64×10^{-9}	7.98×10^{-11}	8.12×10^{-11}
43.3	19.6	1.86×10^{-3}	2.92×10^{-9}	9.57×10^{-9}	4.41×10^{-12}	4.50×10^{-12}

TABLE 2.1— Test with theoretical calculations for proton evolution from the fifth to the sixth models divided in ten sub-steps in which the temperature and density have been linearly interpolated. The fields are: temperature in MK (T_6), density in g/cm^3 (ρ), ^{13}C abundance in mol/g ($Y_{^{13}C}$), cross section for ^{12}C proton capture (σ_1), cross section for ^{13}C proton capture (σ_2), proton abundance derived from Eq. (2.3.3) in mol/g (Theory), and proton abundance yielded by SNUPPAT in mol/g (SNUPPAT). All columns represent the value used for the integration except the last two, which are the results. The starting proton abundance Y_p for the test is given in the text.

know that the final result depends strongly on our particular choice of the cross section value. Therefore, we are considering three different possibilities for this choice. The first one, which corresponds to Figure 2.12 and is detailed in Table 2.1, follows the change of temperature and density for ten sub-steps with a linear interpolation between them. The second and third ones, detailed in Table 2.2, use only one value for temperature and density in both cases. One of them selects the average between both steps and the other one always selects the earlier value. In all of these cases, the benchmark proton abundance starts at $Y_p = 1.92\times10^{-4}$ and ends at $Y_p = 3.32\times10^{-7}$ in mol/g. Meanwhile, the proton abundance for SNUPPAT at the beginning of the fifth model is, per case, 8.19×10^{-5}, 1.23×10^{-4} and 7.99×10^{-4}, also in mol/g, with the difference between them due to the previous steps in the simulation.

T_6	ρ	$Y_{^{13}C}$	σ_1	σ_2	Theory	SNUPPAT
41.7	16.8	1.80×10^{-3}	1.83×10^{-9}	5.99×10^{-9}	2.38×10^{-11}	2.17×10^{-11}
40.0	13.7	1.39×10^{-3}	1.06×10^{-9}	3.46×10^{-9}	7.82×10^{-7}	5.42×10^{-7}

TABLE 2.2— Same as Table 2.1, but each row represents a different one-step test. The first one takes the average value for temperature and density between every pair of models, while the second one is obtained by taking the earliest of these two values.

Once one has the cross section, the density and the abundances, the rates $\lambda_1 = \sigma_1 \rho Y_{^{12}C}$ and $\lambda_2 = \sigma_2 \rho Y_{^{13}C}$ can be calculated and the proton evolution approximated by

$$Y_p(t) = Y_p(t_0) \mathrm{e}^{-(\lambda_1+\lambda_2)(t-t_0)}, \tag{2.3.3}$$

where we are assuming that the rates remain constant during the integration. The time step for the second and third calculations is $\Delta t = 1.91 \times 10^{10}$ seconds, with the first calculation having each of the ten sub-steps with a tenth of that value.

As we can see, in the first case the theoretical values follow closely the SNUPPAT results, while the second and third cases show some disagreement between both. The differences, however, can be explained by either rounding errors in the first case or by recalling that we are supposing the rates as perfectly constant when applying equation (2.3.3), while SNUPPAT takes into account the variations in the ^{13}C abundance in the second and third cases. The main effect of considering the rates constant is that, as the ^{13}C abundance increases during the integration, making the rate to increase, the theoretical value will lag behind (meaning higher proton abundance) with the effect being more apparent the further away we start from the equilibrium value of $\sim 1.86 \times 10^{-3}$ mol/g. Finally, it should be pointed out that even when one of the cases ends with a very similar abundance to that of the benchmark, $Y_p = 3.32 \times 10^{-7}$ mol/g, this is just a coincidence for this particular step, it soon diverges again.

In short, after these tests we are confident that SNUPPAT can correctly integrate a real case scenario with stellar abundances and rates. Moreover, we have shown that nucleosynthesis calculations can be extremely sensitive to the discrete nature of stellar models. Depending on how the temperature and density are selected or which interpolation method is used, the abundances may vary wildly. This effect is greater the farther away the species are from the equilibrium value. It is no coincidence that most of the differences between SNUPPAT and the benchmark values, such as the late ^{54}Fe or the early ^{1}H curves, happen to appear when the species are subject to large changes.

2.4 Conclusions

In this chapter we have shown that the BD method belongs to the family of numerical schemes able to solve the equations necessary to simulate the *s*-process nucleosynthesis. We have also described an explicit method based on the Patankar-Euler scheme which may be expanded in the future. This scheme appears to be faster than the BD method for our simulations, although we have much to test yet before claiming its preferability on a more general scale.

In the same vein, we have found that the GS method is an adequate alternative to an LU factorization when solving the sparse system of linear equations that arise during the application of an implicit method when applied to our AGB nucleosynthesis simulations. Albeit this approach is not universally better than the LU factorization, the situations in which one method is preferable to the other are understandably tied to the physical and chemical structure of the mass shell being solved at each given time. The consequence of this fact is that neighboring shells favor the same method, making the best approach to take easy to predict a number of shells forwards. In practice, if we find that the GS method lags behind the LU factorization for a given shell, we proceed to use the LU factorization for the next 10 shells before trying the GS method again.

Finally, we have made sure that the method we are using is adequate for solving the nucleosynthesis equations. First by testing it against a handful of ideal cases, and then exploring its behavior with a valid benchmark provided to us. The comparison with the benchmark has been particularly interesting on account of the sensibility shown by the results, related to reasons that may very well be outside of the scope of the numerical method chosen in particular.

3

SNUPPAT: Mixing and parallelization

This chapter contains the description of the mixing processes that had to be included in the post-processing code SNUPPAT, as well as the specific difficulties arising from the evolutionary model structure. We also briefly discuss the code parallelization, and make a final test of the code by comparing its behavior to that of a fully-fledged stellar evolution simulation.

3.1 Introduction

In this chapter we continue the line of work laid out in the previous one, completing the code description by tackling the mixing mechanisms that affect the *s*-process nucleosynthesis, such as convection and overshooting.

Because any mixing mechanism must deal directly with the stellar model structure, we also describe in this chapter the challenges that this structure posed to us in the pursuit of an accurate description of the nucleosynthesis process, as well as our proposed method of parallelization.

Finally, we must test the complete code to ensure that the interplay between the nucleosynthesis and mixing mechanisms is working as intended in our interest to accurately portray the *s*-process nucleosynthesis, as well as the impact on the evolution of the stellar surface chemistry. For this we have chosen ATON, the very same evolutionary code we wish to apply post-processing to, understanding that consistency with it is essential for our objective.

3.2 Mixing

Before now we have centered our discussion around equation (2.2.1), which describes the change in abundances due to decay processes and reactions such as neutron captures. This description is incomplete in the context of the AGB chemical evolution, as we are not accounting for the changes due to mixing between different layers of the stellar structure. From all the possible mechanisms for interlayer mixing (see Chapter 1) we have selected the two considered by ATON: convection and overshooting.

3.2.1 Convection

The modelling of convection is a difficult task even in one dimension, and several techniques and approximations such as instantaneous mixing, mixing length theory (MLT), and the full spectrum of turbulence (FST, Canuto et al. 1996) may be used. In fact, one of the defining characteristics of ATON over other evolutionary codes is the use of the FST prescription for convection. However, given that our main objective in the development of the SNUPPAT code is the post-processing of the *s*-process nucleosynthesis on given input physics, we are not concerned with an exact reproduction of physical mechanisms. In particular, we are more interested in the practical effects that convection has in the *s*-process abundances than in the physically correct implementation of convective mixing. As long as we accurately reproduce these abundances, we consider the simulation a success.

There are two important convective regions for the *s*-process during the AGB evolution (see Figure 3.1 for a visual representation of these regions in the stellar structure). The first one is the convective region that develops during a TP in the intershell, mixing the nucleosynthesis products from both the ^{22}Ne and ^{13}C neutron sources. This region is known as the "pulse driven convection zone" (PDCZ) or "Inter-Shell Convective Zone" (ISCZ) in AGB evolution theory. The second one is the convective envelope itself, which during the helium burning phase penetrates into the helium intershell, mixing its contents to the stellar surface. Our main interest is to understand the effects that these convective regions have in our nucleosynthesis processes.

Out of the two main neutron sources, the ^{13}C(α, n)^{16}O reaction is the easiest to assess because this reaction takes place during the interpulse period in the radiative intershell. Therefore, the convective mixing effect is decoupled from the reaction itself. On the other hand, the ^{22}Ne(α, n)^{25}Mg neutron source is active at the same time that the PDCZ appears, which means that there is a potential interplay between both mechanisms at those moments. Specifically, the most pressing question for us is how do the evolutionary scales of both

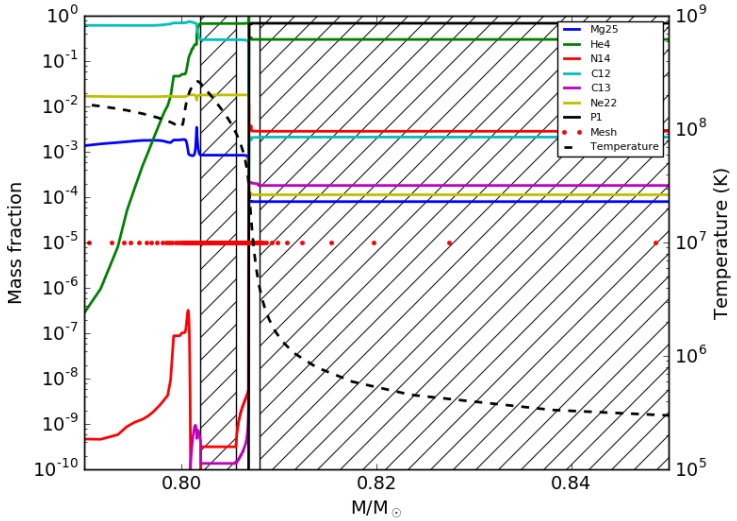

FIGURE 3.1— Stellar interior of a 4 $M_\odot$ AGB star during a TP zoomed in the helium intershell. The regions where the Schwarzschild's stability criterion is not met appear shaded. This criterion establishes whether a given medium is stable against convection. In ATON and many other codes, a region which fails to meet the Schwarzschild criterion is usually regarded as convective. The shaded region to the right represents a fraction of the convective envelope. To the left appears the shaded PDCZ inside the helium intershell, and part of the radiative CO core.

processes compare.

An instantaneous homogenization approach is actually adopted in the literature (see e.g., Marigo et al. 2013). This approach supposes that the mixing mechanism in the PDCZ is faster than the ^{22}Ne(α, n)^{25}Mg reaction. In order to test the validity of this assumption for SNUPPAT, we turn to the available ATON models and check the timescales of the mixing mechanism and the ^{22}Ne(α, n)^{25}Mg reaction in a region inside the PDCZ with a temperature greater than 300 MK. With the temperature and density values, as well as the abundances, we can calculate the reaction rate for the ^{22}Ne neutron source. At the same time, we may roughly estimate the diffusion rate in the PDCZ through the convective velocity and its size using a simple analysis of the schematic

diffusion equation

$$\frac{\partial Y}{\partial t} = D\frac{\partial^2 Y}{\partial x^2}$$

in which, by taking $dt \sim \tau_{diff}$ and $dx \sim L$ gives us

$$\frac{1}{\tau_{diff}} \sim \frac{D}{L^2} \sim \frac{vL}{L^2} = \frac{v}{L}$$

where we have used the approximation $D \sim vL$ (Herwig et al. 1997).

If we take the ATON $6M_{\odot}$ model, the higher temperatures in a PDCZ are around 350 MK, with a typical density of 3500 g/cm^3 and a ^{4}He abundance of $\sim$ 0.2 mol/g. Using these values in the cross section for the ^{22}Ne(α, n)^{25}Mg reaction at this temperature of $N_A\langle\sigma v\rangle = 1.42 \times 10^{-9}$ cm^3/(mol·s) we get a reaction rate for ^{22}Ne of

$$\frac{1}{\tau_{^{22}Ne}} \approx 10^{-6}\mathrm{s}^{-1}.$$

At the same time, the PDCZ in which this reaction takes place extends for 6×10^8 cm, having convective velocities in the range $v \in [10^4, 10^6]$ cm/s. With this we have that the diffusion rate for the PDCZ is in the range

$$\frac{1}{\tau_{diff}} \in [1 \times 10^{-5}, 2 \times 10^{-3}]\mathrm{s}^{-1},$$

or between 10 and 2000 times faster than the reaction rate in one of the worst case scenarios.

With the results of this analysis at hand, we have thus decided to treat both convective zones as instantaneous. Introducing instantaneous mixing in the SNUPPAT code is straightforward, and we simply take an average of the abundances weighted with the shell mass for every shell affected by convection and assign that average to the whole convective region.

3.2.2 Overshooting

When studying *s*-process nucleosynthesis in AGB stars, the exact nature of extra-mixing is one of the strongest debated issues in the theoretical community. It is known that there must be some sort of mixing outside of the convective boundaries given by the Schwarzschild criterion because otherwise the ^{13}C pocket would not form (Herwig 2000). The exact mechanisms responsible for this extra-mixing mechanism and how much each one of them contributes to it are still relatively unknown. In fact, the usual procedure is to make the

extra-mixing dependent on a free parameter (in our case, the overshooting parameter) which is then calibrated with observations or knowledge gained from parameter-free simulations[1]. Furthermore, taking into account that SNUPPAT is a post-processing code we should only consider extra-mixing consistent with ATON and that affects *s*-process nucleosynthesis.

With this in mind, we have added a convective overshooting mechanism to SNUPPAT. The overshooting mechanism is basically understood as the traveling of material beyond the Schwarzschild stability limit due to inertia, which mixes with the stable surrounding environment (Herwig 2000). Like with convection, the exact implementation of the overshooting mechanism is secondary to the effect it has on the *s*-process abundances. However, the main difference with convection is that the overshooting should introduce a profile in abundance instead of being a homogenization mechanism. Moreover, looking for consistency during the post-processing, we need to make the overshooting mechanism time-dependent. Otherwise, we could end up with the same profile for wildly different timescales.

A common approach to this problem (e.g., Herwig et al. 1997; Mazzitelli et al. 2000) is to use an exponentially decaying velocity field such as

$$v = v_b \left(\frac{P}{P_b} \right)^{\pm 1/\omega} \tag{3.2.1}$$

where v_b is the velocity in the convective boundary, ω is a free parameter[2], and the sign is chosen such that $|v| \leq |v_b|$. Then, this velocity is paired with the physical distance to define a coefficient to use in a diffusive equation. Although a diffusion scheme is not strictly physically correct (Lattanzio et al. 2017), from a pragmatic point of view it means that the mixing beyond the convective unstable region is exponentially slower the further away from the convective boundary we go, with the rate of change of a given abundance in an individual shell depending on how close its value is to its neighboring ones. Mathematically, it is usually expressed as

$$\frac{\partial Y}{\partial t} = \frac{\partial}{\partial M_r} \left[(4\pi r^2 \rho)^2 D \frac{\partial Y}{\partial M_r} \right], \tag{3.2.2}$$

with $D \propto v$.

Leaving aside all pretense of an accurate physical description of the process, we keep this idea with a further simplification: Instead of making the rate of

[1] Such as 3D hydrodynamic simulations in which the convection and overshooting stem naturally from the solution to the hydrodynamic equations.

[2] In Mazzitelli et al. (2000) the parameter used ζ is the inverse of ω. We prefer to use ω as a higher value results in a more efficient overshooting. See Fig. 3.2.

change depend on the neighboring abundances, we make it exclusively dependent on the convective region abundance. Our rationale for this decision is that, by supposing a stronger dependence with the convective shell, we simplify the calculations of the extra-mixing while keeping a similar time dependence of the abundances. That is, we set to solve the equations

$$\begin{aligned} \frac{dY^b}{dt} &= \sum \tau_j (Y^j - Y^b) \\ \frac{dY^j}{dt} &= \xi_j (Y^b - Y^j), \end{aligned} \tag{3.2.3}$$

where the superscript b marks values in the convective boundary and j marks values in a given stable shell affected by overshooting. The coefficients are related by conservation of mass with $\tau_j = (m_j/m_b)\xi_j$, where m_b is the mass of the convective region. The ξ_j are given by

$$\frac{1}{\xi_j} = \int_{r_b}^{r_j} \frac{dr}{v_b \left(\frac{P(r)}{P_b}\right)^{\pm 1/\omega}} = \int_{r_b}^{r_j} \frac{dr}{v(r)},$$

where we are intuitively linking the mixing rate with the time it takes for the material to reach the j shell. It is worth to note that the ξ_j can be evaluated inexpensively. For example, with the simple quadrature

$$\int_a^b f(x)dx \sim \sum_{j=a+1}^{b} f(x_j)(x_j - x_{j-1})$$

one obtains the recurrence relation

$$\frac{1}{\xi_j} = \frac{1}{\xi_{j\pm1}} + \frac{|r_j - r_{j\pm1}|}{v(r_j)},$$

where $j \pm 1$ symbolizes the adjacent shell closer to the convective boundary.

Taking a specific Y^j and supposing a constant Y^b, which is not unreasonable when $m_j/m_b << 1$, we can easily solve Eq. (3.2.3) to get

$$Y^j = Y^b(1 - \mathrm{e}^{-\xi_j \Delta t}) + Y_0^j \mathrm{e}^{-\xi_j \Delta t}.$$

As was our objective, a first glance to this solution shows a behavior compatible with Eq. (3.2.2) in which one of the boundaries has a constant value and the other boundary has negligible diffusivity. That is, the abundance distribution approaches an homogeneous Y^b, with shells further from the constant value boundary arriving at Y^b exponentially slower. Finally, the reach and efficiency

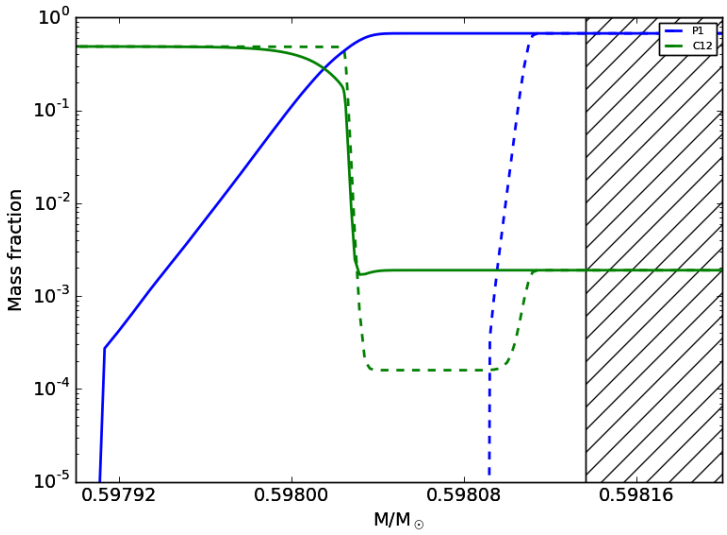

FIGURE 3.2— Superimposed images of two 3 $M_\odot$ simulations differing only on the overshooting parameter. The effect of the extra-mixing is most clearly seen in the proton abundance (solid and dashed blue lines), which extends almost five times more in mass by a change in the overshooting free parameter from $\omega = 0.02$ (dashed) to $\omega = 0.08$ (solid) in this example.

of the overshooting mechanism can be tuned through the free parameter ω in Eq. (3.2.1), as shown in Figure 3.2.

To solve the system (3.2.3) we use the simple implicit Euler method with a Richardson extrapolation up to order four. We can write this system as

$$y' = Ay,$$

with A constant. An implicit Euler method iteration for this system has the form

$$(I - hA)y^{n+1} = y^n. \tag{3.2.4}$$

The matrix $(I - hA)$ derived from equation (3.2.3) is extremely simple. Indeed, if considering exclusively downwards overshooting it can be regarded as a block matrix with as many independent submatrices as there are convective

zones. Each one of these submatrices consist of a symmetric distribution of non-zeros arranged in one row, one column, and a main diagonal, making Eq. (3.2.4) extremely straightforward to solve in linear time. Our particular approach is to modify $(I - hA)$ into an upper triangular matrix U through a series of steps symbolized by the product of transformation matrices P_k as

$$\prod_k P_k \, (I - hA) y^{n+1} = \prod_k P_k \, y^n$$

or, by writing the transformation matrix $T = \prod P_k$ explicitly,

$$U \, y^{n+1} = T \, y^n,$$

where T is a lower triangular matrix.

Knowing that during a basic integration step U and T remain constant for all sub-steps and species, we may store and use them repeatedly to save operations. To understand why in this occasion we prefer this scheme to any other including the GS method, we will show the matrices we obtain with a concrete example of a small but representative overshooting region.

Suppose that our overshooting region extends for three meshpoints from the convective region at the top. Our matrix $(I - hA)$ will have the form

$$(I - hA) = \begin{pmatrix} 1 + h\xi_1 & 0 & 0 & -h\xi_1 \\ 0 & 1 + h\xi_2 & 0 & -h\xi_2 \\ 0 & 0 & 1 + h\xi_3 & -h\xi_3 \\ -h\tau_1 & -h\tau_2 & -h\tau_3 & 1 + h\sum \tau_j \end{pmatrix}$$

according to the notation of Eq. (3.2.3). One can then use the diagonal elements of the three first rows to eliminate the non-diagonal elements of the fourth one, forming the upper triangular matrix

$$U = \begin{pmatrix} 1 & 0 & 0 & u_{14} \\ 0 & 1 & 0 & u_{24} \\ 0 & 0 & 1 & u_{34} \\ 0 & 0 & 0 & 1 \end{pmatrix}$$

and the transformation matrix

$$T = \begin{pmatrix} t_{11} & 0 & 0 & 0 \\ 0 & t_{22} & 0 & 0 \\ 0 & 0 & t_{33} & 0 \\ t_{41} & t_{42} & t_{43} & t_{44} \end{pmatrix}.$$

After this, we can efficiently solve $U\,y^{n+1} = T\,y^n$ with the algorithm

$$\begin{aligned} b_4 &= \sum y_j^n\, t_{4j} \\ b_{i<4} &= y_i^n\, t_{ii} \\ y_4^{n+1} &= b_4 \\ y_{i<4}^{n+1} &= b_i - u_{i4}\, y_4^{n+1} \end{aligned}$$

which can be applied to any similar n by n matrix without loss of generality.

As previously stated, these operations are linear with the number of overshooted meshpoints n. We can also see that there are no fill-ins during the solving process, making this algorithm almost as efficient as a GS method that converges always at the first iteration.

3.3 ^{13}C pocket resolution

In this section we briefly discuss a general problem with the ^{13}C neutron source in post-processing codes. Specifically, we describe the link between mesh resolution and s-process nucleosynthesis in the context of the effective ^{13}C pocket to then outline our implementation of a solution.

The concept of the effective ^{13}C pocket is central to the study of s-process nucleosynthesis in stars where the reaction ^{13}C(α, n)^{16}O is the main neutron source. It is defined by Cristallo et al. (2009) as the mass extent in which $X_{^{13}C} > 10^{-3}$ and $Y_{^{13}C} > Y_{^{14}N}$, where X_i is the mass fraction of species i and Y_i is its molar fraction $Y_i = X_i/A_i$. The relevance of this definition stems from the unavoidable creation of a ^{14}N pocket alongside the ^{13}C pocket after a partial mixing zone is formed, as well as the property of ^{14}N as an effective neutron poison, which dampens the neutron capture by Fe seeds affecting the s-process chain (Lugaro et al. 2003).

The importance of discussing the effective ^{13}C pocket in the context of the post-processing code can be better justified by analyzing the mechanism that gives raise to it. In our current understanding, the protons ingested after a TP undergo the reaction chain ^{12}C(p, γ)^{13}N(β^+, ν)^{13}C, which may continue into ^{13}C(p, γ)^{14}N if enough protons are present. Therefore, in order to get an effective ^{13}C pocket, a non-homogeneous proton profile is needed (Buntain et al. 2017), which results in the formation of both a ^{14}N and ^{13}C pockets with their maximum abundances occurring at slightly different mass coordinates, as can be seen in Figure 3.3.

From a post-processing perspective, once the non-homogeneous proton profile is achieved, through partial mixing by overshooting or an ad-hoc prescrip-

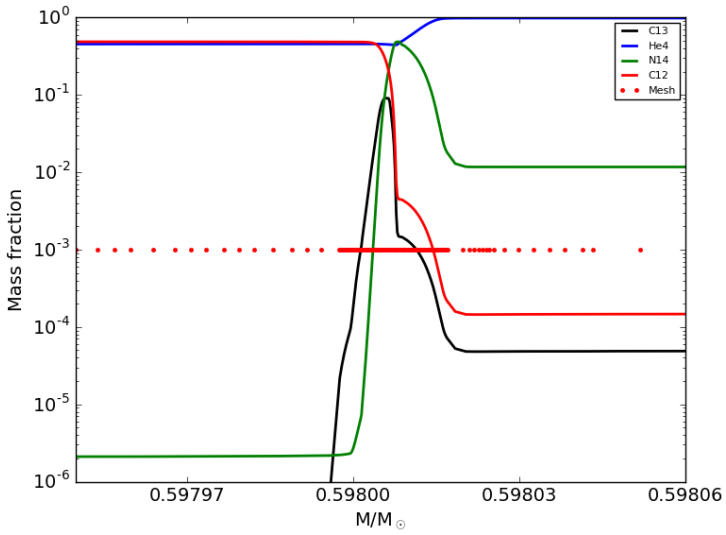

FIGURE 3.3— Model of a 3 $M_\odot$ AGB star interior showing the formation of a small ^{13}C pocket alongside a ^{14}N pocket after a partial mixing episode. Note the large number of meshpoints (∼100) used to correctly resolve the ^{13}C pocket.

tion[3], the only remaining concern is to follow the effective ^{13}C pocket until the nucleosynthesis has taken place. Unfortunately, ATON mesh resolution does not adapt to the creation of these pockets as expected from a code not initially written for *s*-process nucleosynthesis. Keeping the ATON mesh unmodified can artificially shrink the effective ^{13}C pocket, as seen in Figure 3.4.

Therefore, in order to avoid an artificial inhibition of this neutron source we must model the ^{13}C formation region with enough resolution. In SNUPPAT this is managed by identifying this region and increasing the number of meshpoints in it through interpolation. This means that a separate array of "^{13}C shells" with their own chemical information is kept and adjusted for each step of the

[3]As discussed in the introduction, the mechanism surrounding the ^{13}C pocket formation is one of the great unknowns in *s*-process nucleosynthesis simulations. Therefore, instead of introducing a physical mechanisms that results in partial mixing, some groups simply emulate the effect by artificially introducing a partial mixing zone during the third dredge-up phase.

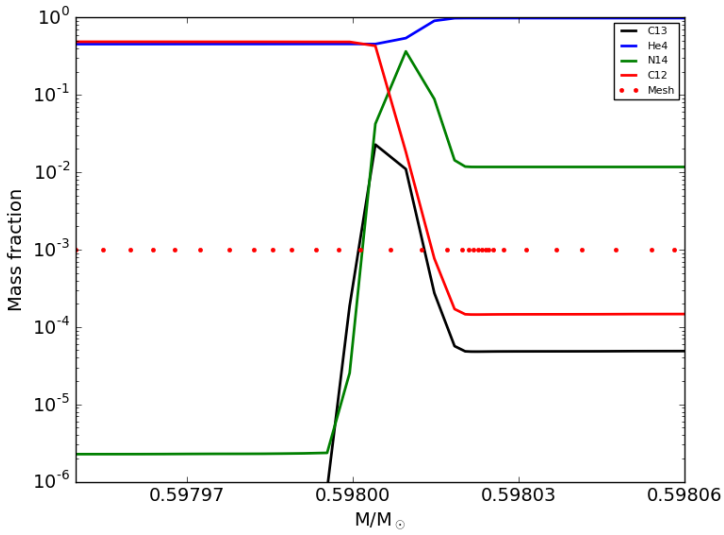

FIGURE 3.4— Same as Figure 3.3 with the only difference being the mesh resolution, which in this case has been taken directly from ATON.

calculation until it is not longer needed which is, interestingly, not when the ^{13}C has been completely consumed. Indeed, after the ^{13}C pocket has disappeared, its products largely linger in the region due to a lack of nucleosynthesis channels (the neutrons and protons are depleted in the zone and the α capture reactions are extremely unlikely). If the enhanced resolution is eliminated before these products are mixed by the next PDCZ, the abundances may change due to a completely artificial interpolation effect.

3.4 Code parallelization

Here we describe how the code has been parallelized to take advantage of multiple CPUs[4], along with a brief overview on how all the pieces we have described up to now fit together to create SNUPPAT.

[4]Although CPU strictly stands for central processing unit, in this section we use the term loosely to abstract any division of the computer processing capabilities.

Parallelization is the process of dividing a long computation into smaller, independent bits to be processed at the same time by more than one CPU. An illustrative example of this would be to handle the multiplication of 342x35 to two people, one in charge of calculating 342x30 and the other 342x5, wait for them to handle their results and add them. Ideally, this process would be twice as fast as one person doing the calculation. In practice, however, this is never achieved. The departure from the ideal case can only come from the extra steps taken to perform the whole calculation. Deciding how to divide the task, communicating the numbers, and gathering the results are the extra steps for this example. These steps are unavoidable and provide an upper limit to the speed up for a given parallelization. We should also consider that one of the multiplications may take more time than the other, halting the whole process until it is done.

The best strategy to implement parallelization is to apply it to the computationally intensive parts of the code. From the beginning of the post-processing to its end, SNUPPAT engages in the following steps. First, it loads the initial physical ATON model and abundance profiles. Second, it loads the next physical model available to derive the time step H for the integration. Third, the need for extra mesh points due to a possible ^{13}C pocket is evaluated and met if positive. A preemptive convective mix is performed to smooth out possible artifacts due to interpolation. Fourth, the integration begins. During this latter step, a chemical integration process and a mixing process take place. In the first one, the equation (2.2.1) is solved by the algorithm discussed in the Subsection 2.2.5. In the second, a homogenization of the convective regions is performed, followed by the solution to Eq. (3.2.3) if necessary, thus accounting for overshooting. After this, everything is repeated from the second step until no more physical models are found.

The bulk of SNUPPAT computations is clearly contained in step four where the chosen method allows for a simple and direct parallelization. First, when solving Eq. (2.2.1) we can see that there is no interdependence between the mass shells. Each one of them is solved separately, which makes it straightforward to divide the calculations among the processes. Considering that some shells take more time to integrate than others and nearby shells have similar integration times, we decided to divide the work as evenly as possible by assigning the shells sequentially to the processes. Second, when solving Eq. (3.2.3) a similar idea is used, splitting this time over the species as the overshooting algorithm acts in several shells simultaneously.

In Figure 3.5 a representation of the parallelization efficiency is shown along with the ideal linear case for a sample of a simulation with extra mixing enabled. In this experiment, the efficiency stays around 100% of the idealized linear case

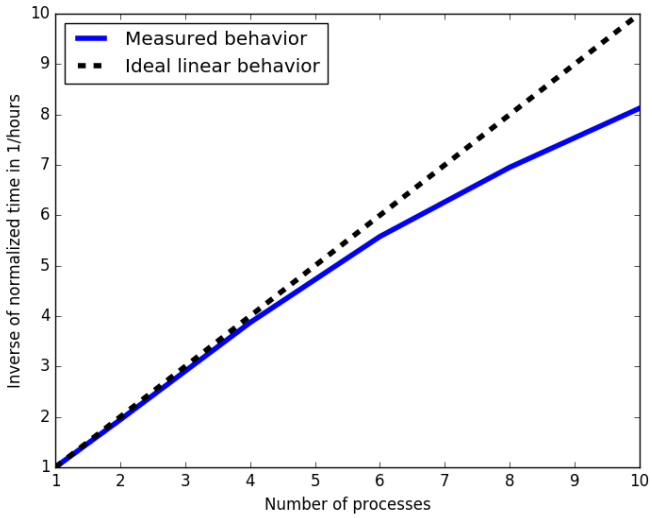

FIGURE 3.5— Sample parallelization experiment for 1 to 10 CPUs with the ideal linear case represented along with the measured behavior.

for the first 4 processes to decrease down to an 80% for the case of 10 processes.

3.5 ATON test

In the previous chapter, the code has been successfully tested for a single radiative shell during an interpulse period. The next natural step, and once introduced the mixing mechanisms to the code, is to test SNUPPAT behavior in a full simulation with several TPs and convective mixing. Because SNUPPAT has been written to work as a post-processing code for ATON, this final test uses ATON results as the benchmark to which compare SNUPPAT abundances.

In order to make this comparison, we limit SNUPPAT calculations to the 30 ATON species, which span from protons to ^{31}P, and relate the species with a total of 68 reactions. We also turn off overshooting both in ATON and SNUPPAT because its effects depend on a free parameter that is explored in Chapter 4. Each trial follows the chemical evolution of a stellar simulation through several

TPs. First, we test SNUPPAT by post-processing the simulation of a carbon star. In ATON, hot bottom burning (HBB) is not seen at solar metallicity until around 3.5 solar masses (see e.g., García-Hernández et al. 2013 and references therein), which makes a 3 $M_\odot$ stellar simulation suitable for this trial. This particular mass has been chosen as well because it is one of the models we extensively use in this work.

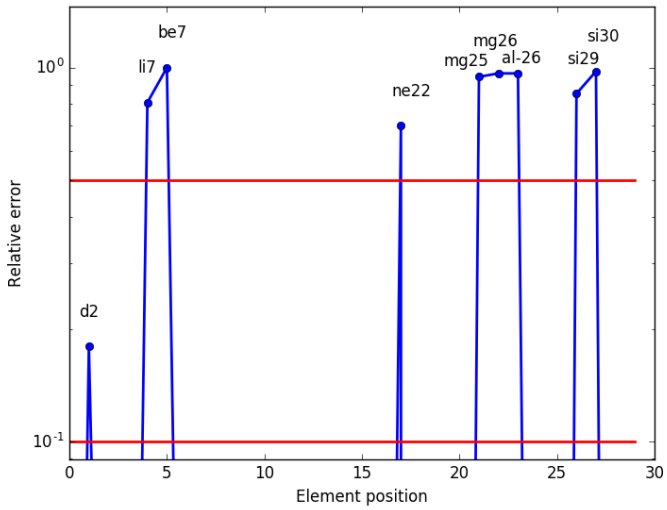

FIGURE 3.6— Relative errors on surface abundance between ATON and SNUPPAT at the end of a 3 $M_\odot$ simulation. The x-axis arranges the species with an arbitrary indexing. The two red horizontal lines mark the 10% and 50% relative error levels.

Out of the 30 species, 7 of them show a relative error (calculated as the difference in mass fraction divided by ATON value) of the surface abundances greater than 50% (see Figure 3.6). Setting aside the ^{7}Li and ^{7}Be isotopes, we know that none of the reactions governing the 5 remaining abundances activate below a temperature of 10 MK when no neutrons are present. Along with the fact that almost all of these species are stable[5], we can safely assume that their

[5]The exception being ^{26}Al which, with a half-life of about 7×10^5 years, can be considered stable inside any pulse or interpulse period.

evolution is mainly contained within the helium intershell.

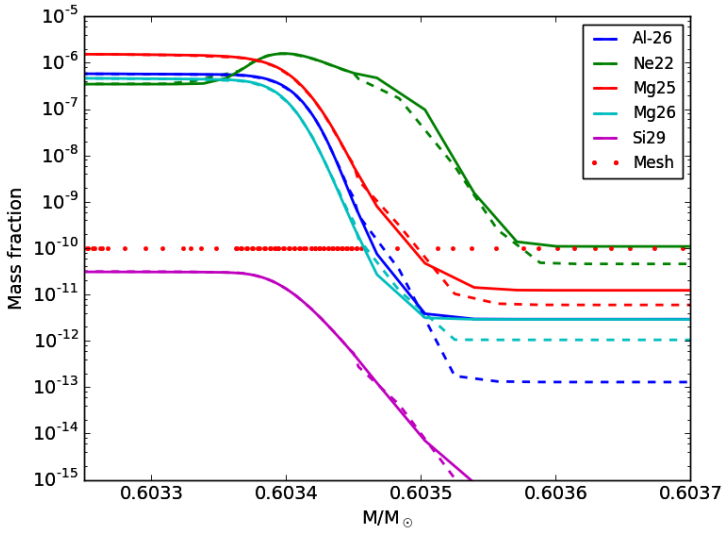

FIGURE 3.7— Chemical profiles for both SNUPPAT (solid lines) and ATON (dashed lines) of the species showing a relative difference greater than 50% in Figure 3.6 at the top of the helium intershell. The ^{30}Si has been left out due to its low value forcing an unclear plot scale. Its behavior is not fundamentally different from that of the other species.

As we know, the dredge-up at the beginning of each TP takes place when the convective envelope penetrates into the helium intershell, mixing the intershell abundances to the stellar surface. Following our previous argument that the evolution of these species is mainly contained in the intershell, we can center our analysis in the specific region of maximum envelope penetration. This region is shown in Figure 3.7, with both the SNUPPAT and ATON chemical profiles after 7.6×10^5 years and 9 TPs of independent chemical evolution. In that Figure we can differentiate two main regions: one in which the profile has no memory of previous pulses, below 0.6036 $M_\odot$ and another one in which disagreements from previous pulses between both codes accumulate, roughly above that mark. The key region to conclude whether SNUPPAT is correctly following the chemical composition is the former one. As we can see, the differ-

ences between both codes in the memory independent region appear, if at all, in places of low meshpoint density. These places are specially prone to inaccuracies when applying interpolation which, as we discuss further in the text, can be a complex subject to deal with.

For testing purposes we now center our discussion on the ^{26}Al intershell abundance. By taking the model of Figure 3.7 and mixing by hand to a depth of 0.6034 $M_\odot$ (the maximum envelope penetration for this TP), the surface ^{26}Al abundance ends up being just 4% lower than the one calculated by SNUPPAT. This difference can be explained by noting two things: First, that the ^{26}Al abundance is very sensitive to the exact meshpoint chosen as the limit for the convective envelope. Second, that the mesh at this model and during the actual mix are different. An illustrative example of the effect this may have comes from taking just one meshpoint deeper into the intershell, representing approximately an extra $\sim 10^{-6}$ solar masses. Through that small change we get a 10% higher surface ^{26}Al abundance than the one calculated by SNUPPAT instead.

Therefore, the differences between SNUPPAT and ATON can be explained by taking into consideration the effects of three factors: The first, explained before, is a consequence of the gradients in the chemical profiles. A small difference in the numerical grid or the chosen meshpoint for mixing can have a noticeable impact on the surface abundances. The second factor is that ATON writes out the physical variables and the chemical abundances in different numerical grids. By using the meshpoints in which the physical variables are stored, SNUPPAT may further diverge from ATON when mixing the abundances to the surface. The third factor is that differences accumulated from previous TPs are stored by the inert convective envelope. As an example, in the ^{26}Al case discussed above, roughly half of the final surface abundance comes exclusively from the envelope.

For the second trial we follow the results on a 4 $M_\odot$ star with both codes. As previously stated, a 4 $M_\odot$ ATON simulation is affected by HBB, allowing us to study SNUPPAT behavior when nucleosynthesis takes place in the convective envelope. Incidentally, one of the consequences of choosing an instantaneous mixing approach is the inability to properly simulate the HBB nucleosynthesis (Lattanzio et al. 1996). Indeed, as represented in Figure 3.8 for the case of ^{12}C, SNUPPAT is clearly unable to do so.

We can more closely simulate the effects of HBB with SNUPPAT by increasing the frequency at which the convective mixing is performed, as represented in Figure 3.9. However, this frequency increase comes at a higher computational cost with no effect on the *s*-process distribution. Therefore, we simply restrict SNUPPAT surface abundance predictions to heavier than iron species

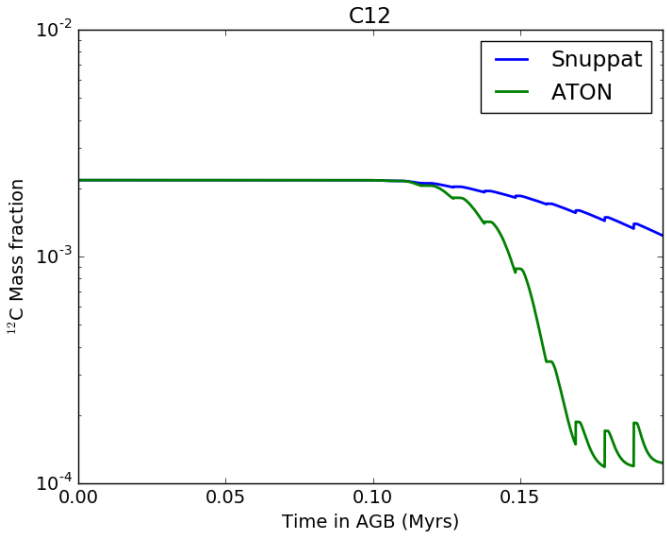

FIGURE 3.8— First 2×10^5 years of AGB surface abundance evolution of ^{12}C for both ATON and SNUPPAT for a 4 $M_\odot$ simulation. After the first 10^5 years, the HBB activates, affecting the ^{12}C surface abundance. SNUPPAT prediction lags behind the more accurate ATON values due to the former simplified convective treatment.

when HBB occurs.

To understand why the presence of HBB should not affect the *s*-process distribution, we must recall that the *s*-process nucleosynthesis takes place in two specific situations: Inside the radiative ^{13}C pocket that appears in the hydrogen burning ashes during an interpulse period, and at the bottom of the PDCZ during a TP. Because the relevant neutron releasing reactions are ^{13}C(α, n)^{16}O and ^{22}Ne(α, n)^{25}Mg, an *s*-process simulation depends, in a first order level, on the abundances of ^{4}He, ^{12}C, and ^{22}Ne in the intershell. With this statement we are not considering other species such as ^{14}N irrelevant for *s*-process nucleosynthesis: we simply state that we do not expect any other of relevant species to be more sensitive to HBB than these.

In Figure 3.10 we show the intershell abundances for both ATON and SNUPPAT after 2×10^5 years of independent simulation, which include 10^5 years of

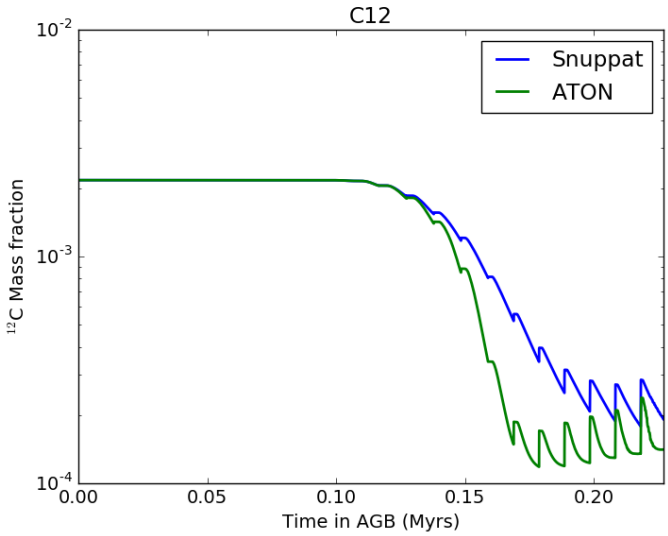

FIGURE 3.9— Same as Figure 3.8 with a change in SNUPPAT mixing frequency of approximately two orders of magnitude. This Figure helps us to corroborate that most, if not all, of the differences in the ^{12}C surface abundance comes from the interplay between the nuclear reactions and mixing processes.

active HBB and a total of 20 TPs. From this figure, it is clear that, although the HBB significantly affects the convective envelope abundances, the products of the hydrogen burning ashes do not depend on the exact envelope composition, which means that the ^{13}C neutron source is effectively unaffected. However, this independence raises the question of why some abundances, such as that of the ^{22}Ne, are again different further into the helium intershell. Given that the abundance of ^{22}Ne can be critical for the *s*-process nucleosynthesis, we now focus our discussion on it.

We have represented in Figure 3.11 what we think is the driver of the difference between SNUPPAT and ATON mass fraction values for ^{22}Ne and other species in the helium intershell. In the top panel of the figure appear the profile abundances during one of the interpulse periods for this simulation. Hydrogen is turning into helium and the envelope is shrinking, with its border effectively

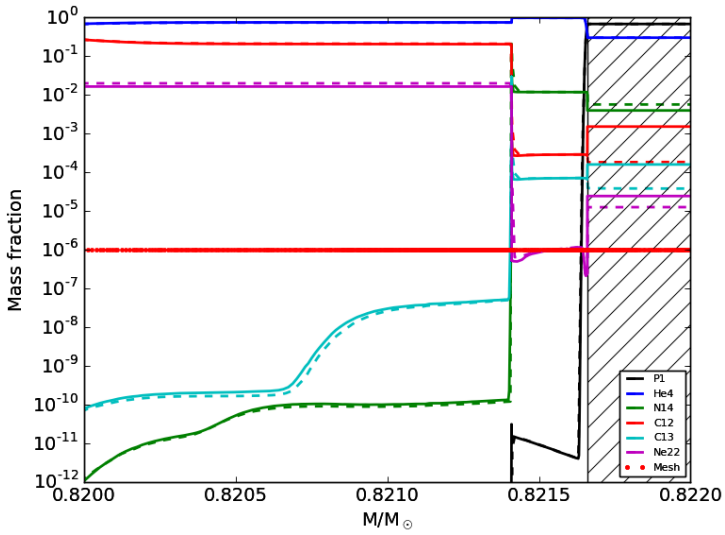

FIGURE 3.10— Intershell abundances for SNUPPAT (solid) and ATON (dashed) with a portion of the convective envelope visible (shaded area) after 2×10^5 years and 20 TPs of independent chemical evolution in a 4 $M_\odot$ simulation. Despite the significant differences in the envelope abundances due to HBB nucleosynthesis, it can be seen that the intershell abundances are extremely similar. The notable exception, discussed in the text, is the ^{22}Ne which presents a 20% relative difference between both codes.

moving upwards in mass. At the same time, the intershell remains relatively inert, showing no meaningful change in any of the drawn abundances, with the exception of ^{13}C, which is destroyed[6] through ^{13}C(α, n)^{16}O. The bottom panel represents the same region of the star at a later time, just before the TP starts. Looking closely at the 0.818 $M_\odot$ mass coordinate, it is clear that from the top to the bottom panel, the ATON ^{22}Ne abundance has changed near that mass coordinate, while the SNUPPAT ^{22}Ne abundance has stayed practically constant. This change, far from being physical, comes from the behavior of the ATON interpolation method when the numerical mesh changes near a vertical

[6]No meaningful neutron density is produced in this stage due to the low ^{13}C mass fraction. Therefore, no *s*-process nucleosynthesis takes place here even though one of the key reactions is activated.

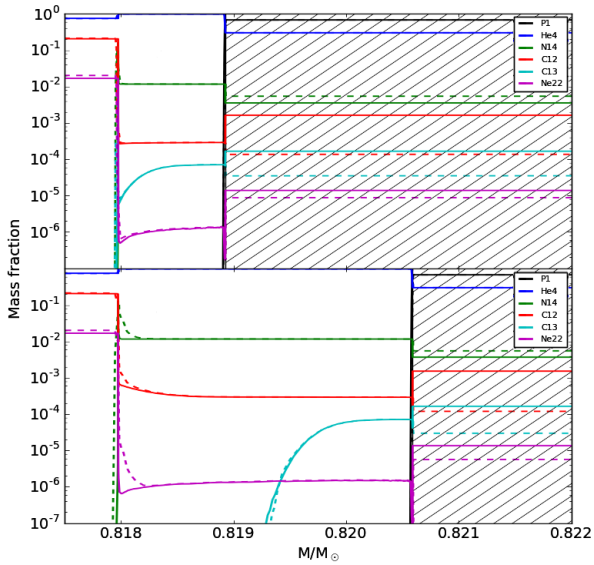

FIGURE 3.11— Comparison of the SNUPPAT and ATON evolution for the helium intershell for a 4 $M_\odot$ stellar mass. The top panel represents the beginning of an interpulse period with the active hydrogen burning shell and the largely inert helium intershell. The bottom panel is the snapshot captured moments before the PDCZ develops. In both panels, the ATON abundances are drawn with dashed lines and the SNUPPAT abundances are drawn with solid lines.

profile. The consequence of this inaccuracy is the creation of extra ^{22}Ne that gets mixed to the intershell during each TP when the PDCZ appears.

Although it is not straightforward to see that the differences between the codes come from the interpolation method, there are some behaviors that point in this direction. The most obvious one is seen when going through adjacent temporal snapshots in quick succession, such as when looking at an animation of the simulation. In this case, the greatest change in several of the abundances in the 0.818 $M_\odot$ mark appears precisely at the same time as a couple of additional meshpoints are added to the region. This behavior is even seen in ^{13}C while being consumed by alpha captures. Another approach to this argument is that the abundance change does not seem to follow the intershell trend. For example,

the ^{14}N and the ^{22}Ne usually go in opposite directions while here they are both being created at the same time.

Finally, an observation can be made that this growing behavior is only found in abundances for which the gradient with respect to the mass coordinate is negative. In a positive gradient situation the abundances are lowered in this region, reinforcing the idea of an artificial change as a consequence of interpolating near an abruptly changing chemical profile. At this point we should draw attention to our preferred method of cubic monotonic interpolation, an algorithm specifically designed by Steffen (1990) to avoid the issues discussed in this subsection, albeit in the field of hydrodynamics. The drawback of this interpolation scheme is that it can lose track of poorly sampled extrema (such as maxima or minima in the profiles), which is not a concern in the highly resolved ATON models.

With this analysis completed we are certain that SNUPPAT is able to correctly follow the *s*-process nucleosynthesis in low and intermediate mass stars. Our main caveat is that the code cannot reproduce the correct HBB abundances, but we have given evidence to show that this fact should not affect our main goal of providing ATON models with accurate *s*-process nucleosynthesis capabilities.

3.6 Conclusions

The most important conclusion of this chapter is that SNUPPAT correctly solves the system of ODE equations associated with the *s*-process nucleosynthesis, along with the mixing mechanisms necessary to modify the stellar surface abundance distribution and for the formation of the ^{13}C pocket. Moreover, we have shown that SNUPPAT is able to follow a much better stablished AGB evolutionary code such as ATON along several TPs, giving the correct intershell abundances for most of the species followed by the computations. In those cases in which we have found significative differences in abundance, outside of the envelope HBB nucleosynthesis, we have concluded that they were a consequence of inaccuracies raising from the use of different interpolation methods in the same numerical mesh.

Although SNUPPAT is clearly successful in the task that we originally set out to solve, several working venues are open for the future. The most interesting one is, without doubt, the possibility of adding a time-dependent convective mixing scheme (such as the MLT or the FST prescriptions) to the code. This should allow us to accurately follow the HBB nucleosynthesis, linking our abundance predictions for *s*-process species and HBB products such as ^{7}Li.

Finally, we have shown that SNUPPAT can be trivially parallelized opti-

mally for up to 10 CPU, considerably speeding up the calculations. Along with the newly described explicit algorithm, this is one of the most interesting areas for us to optimize in the future. The reason behind this assertion is that we have not really delved into the literature of parallelization techniques whatsoever, which opens the gate to more interesting and efficient ways of spreading the work and accelerating the calculations.

4

SNUPPAT results at solar metallicity

In this chapter we take an exhaustive look into the effects our particular extra-mixing implementation has on the *s*-process nucleosynthesis. We also present the SNUPPAT heavy element stellar surface abundances predictions, which we attempt to understand and explain on their own merit.

4.1 Introduction

The scientific method states that the usefulness of any hypothesis can be measured in its ability to obtain predictions that match with reality. In a very real sense, numerical modelling through a specific code is akin to the knitting of a fabric of many such hypotheses. These hypotheses can range from the most intuitive, such as the assumption that the laws of physics apply everywhere in the universe as they are observed on Earth, to some reasonably contested ones, such as that stellar rotation does not affect the production of *s*-process nucleosynthesis.

Beyond what one can actually argue about these hypotheses lies the actual implementation of the code. That is, the code works as an instantiation of the theoretical discussion, freezing the assumptions to a specific distilled prediction. These assumptions forever accompany each set of results and, in particular for a nucleosynthesis calculation, tell the story of the obtained abundance distributions, difficult as it might be to understand the underlying cause for every specific value and ratio.

Three avenues are open to us then to try and validate these hypotheses. The first one, the observations, is constrained by the very nature of our object of interest. The stars are among the farthest things we can study, and only a handful of *s*-process species can actually be observed. To match these is

more often than not a matter of adjusting some parameters and, therefore, although undoubtedly the gold-standard for science, the current observations are not enough to understand the physics behind these processes. The second possibility is to study our set of hypotheses in isolation, looking for internal consistency between them and the already well established theoretical work. The third way is to check our predictions with those of other calculations made in the same field. Knowing that we all start from the same basic hypotheses, the differences that arise must be completely contained in the few conflicting and unproven ideas. That is, supposing an ideal absence of code bugs.

This chapter is dedicated then to an in-depth analysis of SNUPPAT nucleosynthesis predictions and the effect that some evolutionary and post-processing mechanisms have in the stellar surface abundance distributions. In particular, we study the effects that both convection and overshooting have in the stellar surface abundances of *s*-process elements in order to lay the groundwork from where to derive an explanation of the code results. Afterwards, we present said results along with our preferred interpretation for their specific distribution.

4.2 Extra-mixing effects

As previously discussed, the *s*-process nucleosynthesis is highly dependent on extra-mixing mechanisms both at the bottom of the convective envelope and at the bottom of the PDCZ. In the first case, it is the only way we can currently form a ^{13}C pocket to activate the ^{13}C(α, n)^{16}O neutron source (Buntain et al. 2017). In the second case, activation of extra-mixing at the bottom of the PDCZ has different effects depending on if we activate it in the stellar evolution code or in the post-processing code. If activated in the stellar evolution code, it can lead to an increase in the third dredge-up efficiency due to a higher He luminosity (Herwig 2000). When activated in the post-processing code, it can lead to both a more efficient mixing of the ^{22}Ne products and an enhancement of the ^{13}C pocket through the increase of ^{12}C in the intershell (Lugaro et al. 2003).

Both of these extra-mixing processes can be activated in ATON and are, at the same time, simulated in SNUPPAT through the algorithm described in Section 3.2. We now briefly study the effects that these processes have in SNUPPAT general evolution and final *s*-process abundances.

4.2.1 Extra-mixing at the bottom of the PDCZ

As summarized before, there are three main effects derived from applying extra-mixing to the bottom of the PDCZ. The first and most direct one is a more efficient mixing of the nucleosynthesis products from the ^{22}Ne neutron source

into the He intershell from where they are later mixed up to the surface during a TDU episode. The reason is that the relevant temperature maximum during a TP is located just below the lower edge of the PDCZ, as represented in Figure 4.1.

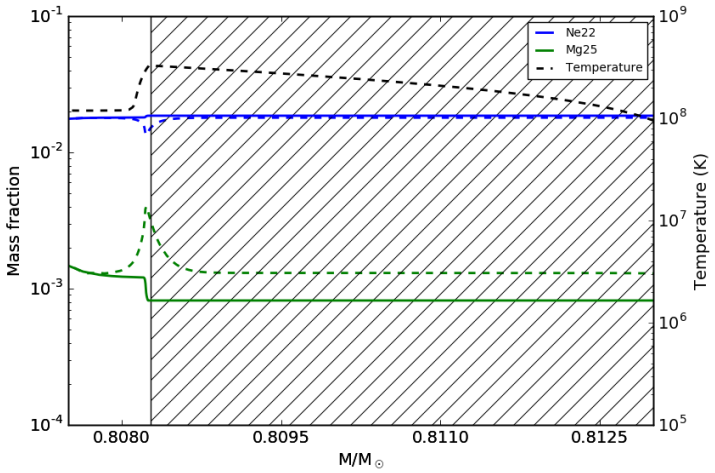

FIGURE 4.1— Two snapshots of a 4 $M_\odot$ AGB simulation during a TP at solar metallicity. The first one while the PDCZ is active and the second one just after the PDCZ disappearance. The temperature (black dashed line) and convective region (shaded area) belong to the first snapshot with solid lines for both the ^{22}Ne and the ^{25}Mg. From the second snapshot, only the chemical profiles in dashed lines for ^{22}Ne and ^{25}Mg are shown. The effects of the ^{22}Ne(α, n)^{25}Mg reaction are visible both as an homogeneous increase of the ^{25}Mg abundance in the convective region, and as chemical profile in the ^{22}Ne and ^{25}Mg abundances in the radiative shells that appear as the PDCZ vanishes

In AGB stars the ^{22}Ne(α, n)^{25}Mg reaction does not efficiently activate below a temperature of 3×10^8K (see e.g., Karakas & Lattanzio 2014). This means that a consequence of having the temperature profile peaking just outside of the PDCZ can leave a significant portion of the ^{22}Ne neutron source nucleosynthesis at the bottom of the He intershell, where it may not be carried up to the surface during the next TDU event.

The second effect is that ^{12}C from the core can be mixed to the intershell, increasing its abundance and thus enhancing the ensuing ^{13}C pocket neutron

exposure (Lugaro et al. 2003) and neutron density. A simple example can be gathered from our simulations and is presented in Table 4.1, where different parameters of PDCZ overshooting are used and the corresponding values for ^{12}C and neutron density are presented for two different TPs. In this table, the effect of the PDCZ overshooting on intershell ^{12}C and neutron density is apparent. In each TP the simulation with PDCZ overshooting presents both more ^{12}C abundance and neutron density.

PDCZ ω	$X^a_{^{12}C}$	n^a	$X^b_{^{12}C}$	n^b
0	0.173	7.67×10^4	0.240	5.67×10^7
0.002	0.189	9.49×10^4	0.369	8.53×10^7

TABLE 4.1— Values for intershell ^{12}C and peak neutron density for a 4 $M_\odot$ simulation at solar metallicity. The values are presented for the 3rd TP (superscript a) and the 15th TP (b). The two simulations were run with the same overshooting parameter for the bottom of the convective envelope. The ^{12}C is expressed in mass fraction and the neutron density is in units of cm^{-3}.

The third effect of having extra-mixing at the bottom of the PDCZ is related to the maximum penetration of the convective envelope into the He intershell. Given that the convective regions used by SNUPPAT are exclusively calculated by the stellar evolutionary code, we are unable to reproduce this effect unless there is an active overshooting region at the bottom of the PDCZ in ATON. Once activated, however, the effect is quite noticeable. As an example, in Table 4.2 we show several dredge-up efficiency measurements for two 4 $M_\odot$ simulations. These simulations are identical with the exception of the activation of extra-mixing at the bottom of the PDCZ with an overshooting parameter $\omega = 0.002$.

Among the selected parameters, the most interesting when considering s-process enrichment of the stellar envelope are the TDU efficiency parameter λ[1] and the ratio of the dredged-up mass to the envelope mass M_D/M_E. The first parameter is a rough indication on the proportion of s-process products generated during the given pulse and mixed up to the surface. This is because, as previously discussed, the s-process nucleosynthesis takes place in the helium intershell, with its products being homogeneously distributed in it by the ensuing PDCZ before the TDU event. The second parameter is an indicator of the impact that the given TDU event has in the envelope abundances. As the

[1] As a reminder, this parameter is defined as the ratio between the extent of the envelope incursion in the core and the core mass gained during the last interpulse period. A value of 0 indicates no incursion of the envelope, while a value of 1 indicates zero core growth for the given TP.

λ_1	λ_2	M_{D1}	M_{D2}	M_{D1}/M_{E1}	M_{D2}/M_{E2}	$L_{3\alpha1}/L_{3\alpha2}$
0.16	0.24	4.2×10^{-4}	7.1×10^{-4}	1.4×10^{-4}	3.0×10^{-4}	1.01
0.19	0.37	5.0×10^{-4}	1.3×10^{-3}	1.6×10^{-4}	4.2×10^{-4}	1.01
0.28	0.44	8.0×10^{-4}	1.6×10^{-3}	2.6×10^{-4}	5.3×10^{-4}	0.97
0.31	0.49	8.6×10^{-4}	1.9×10^{-3}	2.8×10^{-4}	6.2×10^{-4}	0.97
0.38	0.54	1.1×10^{-3}	2.1×10^{-3}	3.6×10^{-4}	7.2×10^{-4}	0.98
0.49	0.44	1.6×10^{-3}	1.3×10^{-3}	5.5×10^{-4}	4.6×10^{-4}	1.01
0.45	0.63	1.3×10^{-3}	2.6×10^{-3}	4.6×10^{-4}	9.5×10^{-4}	1.00
0.47	0.62	1.2×10^{-3}	2.3×10^{-3}	4.6×10^{-4}	8.6×10^{-4}	0.97
0.51	0.55	1.4×10^{-3}	1.7×10^{-3}	5.6×10^{-4}	6.6×10^{-4}	1.08
0.52	0.66	1.5×10^{-3}	1.6×10^{-3}	6.3×10^{-4}	1.1×10^{-3}	1.00
0.58	0.61	1.7×10^{-3}	1.9×10^{-3}	7.5×10^{-4}	8.5×10^{-4}	0.92
0.59	0.71	1.7×10^{-3}	2.8×10^{-3}	8.5×10^{-4}	1.2×10^{-3}	0.81
0.57	0.61	1.7×10^{-3}	2.0×10^{-3}	9.8×10^{-4}	2.1×10^{-3}	0.59
0.53	0.67	1.6×10^{-3}	2.6×10^{-3}	1.1×10^{-3}	1.4×10^{-3}	0.52
0.55	0.63	1.8×10^{-3}	2.6×10^{-3}	1.4×10^{-3}	2.1×10^{-3}	0.90
0.46	0.49	1.4×10^{-3}	1.7×10^{-3}	1.3×10^{-3}	1.6×10^{-3}	0.98
0.44	0.47	1.2×10^{-3}	1.4×10^{-3}	1.4×10^{-3}	1.6×10^{-3}	0.72
0.44	0.60	1.3×10^{-3}	1.9×10^{-3}	1.8×10^{-3}	2.5×10^{-3}	0.70

TABLE 4.2— Quantities related to TDU efficiency in two 4 $M_\odot$ simulations, identical in everything except for the activation of overshooting at the bottom of the PDCZ. The subscript 1 marks the quantities of the simulation without overshooting at the bottom of the PDCZ, while the subscript 2 marks those with an overshoot of $\omega = 0.002$ in that region. Each row indicates a different TDU event, chronologically ordered from earlier to later. The column values are: λ, the TDU efficiency parameter; M_D, the dredged mass in units of solar masses; M_D/M_E, the ratio of dredged mass to envelope mass; and $L_{3\alpha1}/L_{3\alpha2}$ the ratio of the peak helium luminosities in each simulation per TP.

envelope is blown away by the stellar winds, each TDU event has a potentially greater impact on the surface chemistry. For the 4 $M_\odot$ simulation it is clear that the TDU episodes are more efficient when the overshooting is activated at the bottom of the PDCZ in ATON. This behavior has been linked to higher helium flash luminosities (Herwig 2000), which are presented in the Table 4.2 as a ratio. Although the correlation with the TDU efficiency measuring parameters is not direct, which may point towards additional mechanisms for those values, the general trend does hold. We also observe a slight increase in the maximum intershell temperature (not depicted in this table) in the order of the MK for these stellar models. As expected, this TDU enhancing effect depends on the stellar mass, with the less massive 3 $M_\odot$ ATON models showing no significant change in the TDU efficiency after the activation of the PDCZ overshooting.

4.2.2 Extra-mixing at the bottom of the convective envelope

The two main objectives of having an extra-mixing mechanism at the bottom of the convective envelope is to both enhance the TDU efficiency and to form the ^{13}C pocket in which the reaction ^{13}C(α, n)^{16}O can take place. Out of these two objectives, we focus our present discussion on the impact that the simulated overshooting has on the latter. The former, while interesting, is relatively easy to understand: an increase in TDU efficiency mixes more products from the intershell to the envelope, enhancing the stellar surface abundances.

The exact nature of the extra-mixing algorithm is key to the formation of the ^{13}C pocket. Thus, a more detailed description of the overshooting simulation is justified. In that regard we note that, when using an exponential profile for the velocities as described in Section 3.2, there are just two parameters governing the overshooting mechanism as a whole: the parameter ω appears explicitly in the velocity profile (3.2.1) and the cut-off velocity for the overshooting simulation. The former of the two affects the efficiency and penetration of the overshooting mechanism as it directly controls the rate of velocity decay from the convective border. Specifically, a larger ω value keeps velocities closer to those of the convective boundary for a greater extension. In turn, a higher velocity at a given distance is tied with more efficient mixing. On the other hand, the cut-off velocity limits the extension of the partial-mixing zone without affecting its efficiency in the individual mass coordinates. We study first the effects of the cut-off velocity on the ^{13}C pocket formation and *s*-process nucleosynthesis.

In a purely advective situation, the composition of a given mass shell remains constant until an overshooted eddy traveling from the nearest convective region (envelope or PDCZ) arrives and diffuses. This means that the velocity field stemming from the convective zone should extend in a time-dependent fashion. There are, however, two main problems with this approach. The first is one of oversimulation (i.e., attempting to obtain a simulation pointlessly close to reality). Bearing in mind that convection cannot occur in a one-dimensional context, trying to model the extension of the velocity field after the eddy behavior would introduce further unknown free parameters in need of tuning. The second problem is that this purely advective approach completely ignores any other mechanism affecting the composition in those shells. In particular, those that introduce a diffusive component to the overshooting process. The consequence of these considerations is a simplification in the form of a velocity field that reacts instantaneously to changes in the convective border.

We can, however, use a purely advective reasoning to gauge the full extension of this velocity field in our post-processing simulation. The basic idea is to

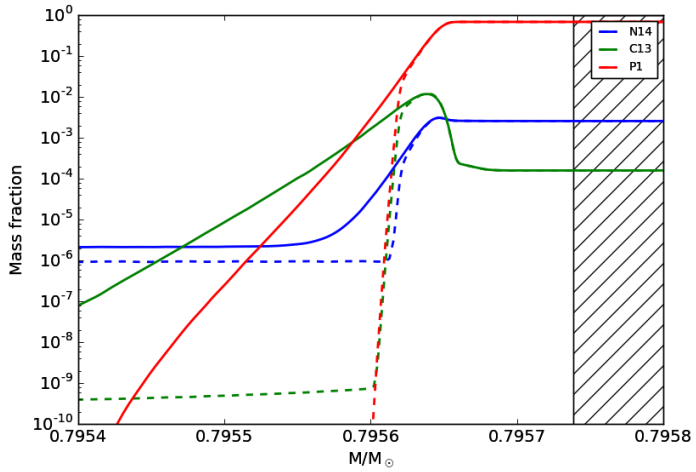

FIGURE 4.2— Two snapshots of the same model in two different 4 $M_\odot$ AGB simulations at solar metallicity during a partial-mixing episode with the same overshooting parameter but different overshooting limit. The dashed lines represent the abundance profiles generated by an overshooting mechanism limited from a purely advective point of view, while the solid lines show the abundances generated by an effectively boundless extra-mixing mechanism. The difference in the proton profiles have a profound implication for the shape of the ^{13}C pocket and the final nucleosynthesis abundances.

limit the extent of the partial-mixing zone to where it is reasonable to expect material from the convective envelope. A simple approximation for obtaining this limit is to move a fluid element through the velocity field, calculating how much time it takes to reach any given shell. We can then limit the overshooting to a shell τ years away from the convective envelope. This quantity τ should represent the maximum time that a given convective border exists unaltered in the same mass shell, such as the maximum envelope penetration during a TDU event, which for a 4 $M_\odot$ simulation is around 1000 years. We call this approach the "bounded" overshooting mechanism. On the other hand, if the overshooting algorithm used is just a proxy for a number of extra-mixing mechanisms taking place in the region, we can limit the overshooting only when its effects become negligible. We call this approach the "boundless" overshooting mechanism.

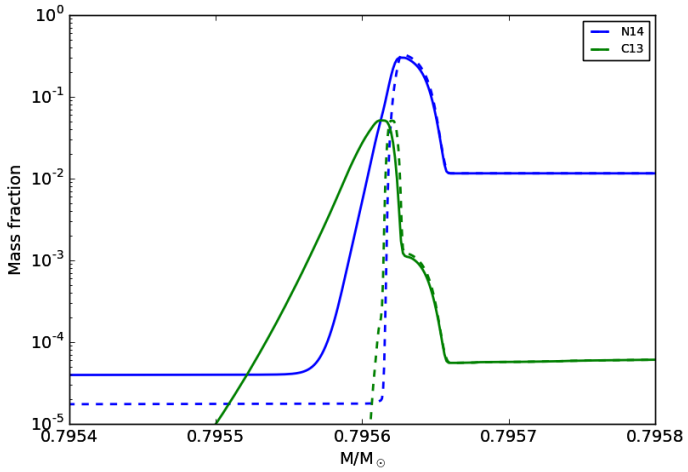

FIGURE 4.3— Same as Figure 4.2 but for a model after all the protons have been captured. The differences in shape and size of the ^{13}C pocket profiles are apparent.

A comparison of the proton profiles formed by each approach during a partial-mixing is represented in Figure 4.2. As expected, a change in the overshooting limit but not in the free parameter (both simulations have $\omega = 0.08$) affects the extent of the proton profile while keeping the values prior to the limit (that is, closer to the convective boundary) largely unmodified. This means that the extension of the ^{13}C pocket, which depends on the $Y_p/Y_{^{12}C}$ ratio being below 0.5 to avoid the formation of the ^{14}N neutron poison (see e.g., Goriely & Mowlavi 2000; Buntain et al. 2017), must be smaller in the bounded case. The shape and size of the ^{13}C pockets formed by each of the proton profiles are shown in Figure 4.3.

While it is clear at a glance that both the shape and span of the ^{13}C pocket are extremely sensitive to the chosen approach for overshooting limit, a more useful tool to understand the differences between the pockets is a representation of the neutron density profile and the mass fraction of the effective ^{13}C pocket. This mass fraction is defined as $X_{^{13}C_{eff}} \equiv 13\,(Y_{^{13}C} - Y_{^{14}N})$ (e.g., Cristallo et al. 2009), and examples of its use can be seen in Buntain et al. (2017). The effective ^{13}C pocket mass fractions for the profiles in the previous figure are

represented in Figure 4.4.

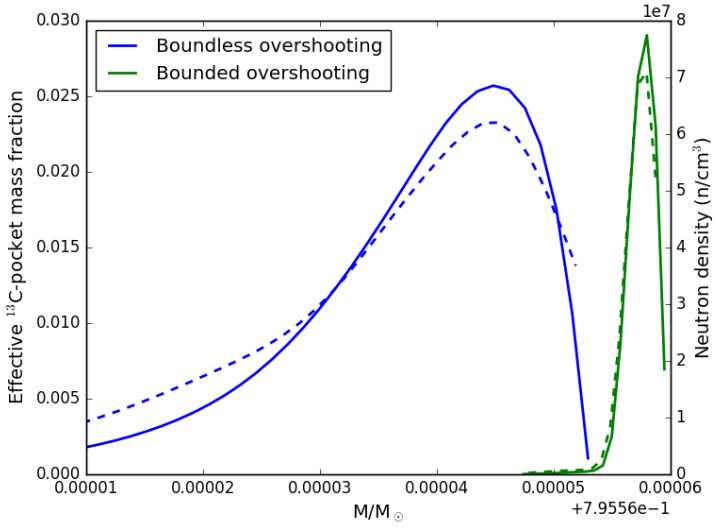

FIGURE 4.4— Mass fraction of the effective ^{13}C pocket at its peak as defined in the text (solid lines) with the maximum neutron density generated by each pocket (dashed lines) for the pockets represented in figure 4.3. The neutron density is the quantity largely responsible along with the neutron exposure for the *s*-process distribution in each mass coordinate to be later dredged-up to the stellar surface.

As expected, the boundless overshooting mechanism produces a wider neutron profile than the bounded case for the same overshooting parameter. This results both in an overall increase of the *s*-process production as well as a change of the abundances distribution. The overall increase stems from the fact that a wider pocket simply affects more mass shells, which in turn gives rise to more material to mix in the PDCZ. The change in abundance distribution has to do with the modification of the neutron density profile. To understand why, we just need to consider that a particular *s*-process distribution in a mass shell depends on the initial abundances, the neutron density, and the neutron exposure in that shell (e.g., Herwig et al. 2003). Given that the initial abundances are usually homogenized and that the ^{13}C pocket is usually small enough for the

temperature to be considered constant, the main drivers for differences in the abundance distribution after a given time span between mass coordinates are the neutron density and neutron exposure profiles over those coordinates.

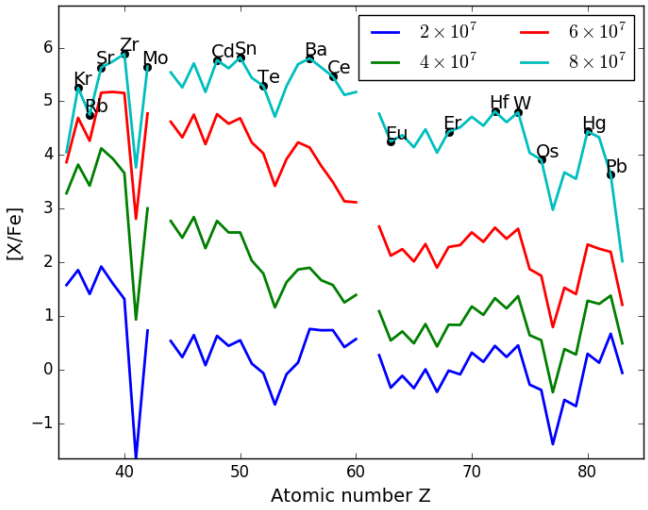

FIGURE 4.5— Section of *s*-process nucleosynthesis abundances at constant neutron density. Every simulation is identical except for the neutron density, which ranges from $2{\times}10^7$ to $8{\times}10^7$ n/cm^3, and the neutron exposure, which is proportional to the neutron density. The calculations are started from solar abundances and run for 1500 years at a temperature of 100 MK with constant neutron density. A number of abundance ratios such as [Sr/Zr], [Cd/Te], [Cs/Ba], and [hs/ls] (roughly the ratio of the averages of the Ba peak and the Zr peak abundances) noticeably depend on the neutron density and exposure considered, as explained in the text. The first blank spot belongs to Tc and the second one to Pm given that the reference values for both elements is 0 due to the lack of stable isotopes.

Idealizing the neutron profile as constant with homogeneous initial abundances and temperature, we can calculate the local *s*-process abundances for a range of neutron densities and a set time span. Such a calculation is shown in Figure 4.5 for a range of values compatible with the neutron density profiles arising from the ^{13}C pockets represented in Figure 4.4. Although the actual stellar surface abundances depend on several factors not considered in this sim-

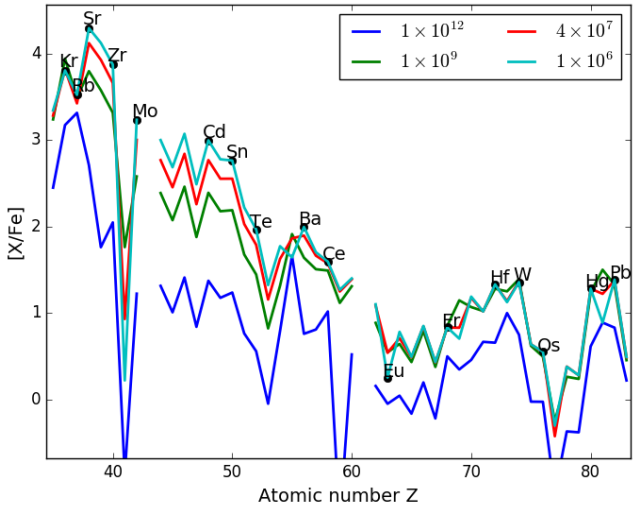

FIGURE 4.6— Similar to Figure 4.5, with a broader range of neutron densities and varying the integration time so that every simulation is subjected to the same neutron exposure of 0.25 mbarn^{-1} as that of the $4{\times}10^{7}$ curve (included here) in Figure 4.5. Note that while [hs/ls] is less sensitive in this case, some elements such as Sr, Y, Zr, Cs or Ba are patently sensitive to the different neutron densities. There is an additional effect taking place for Y, M, Cs, Pr (Z = 59), and Ta (Z = 73), albeit not immediately apparent from this figure. Both effects are described in the text.

ple example[2], we can certainly see how different neutron density profiles have a non-trivial effect on the abundances distribution. It should be noted that in Figure 4.5 both the effects of neutron density and exposure are shown at the same time. Indeed, given that we use the same temperature and temporal span for all the examples, this means that the neutron exposure changes proportionally with the neutron density, with the values being 0.12, 0.24, 0.37 and 0.49 mbarn^{-1}, respectively for the neutron densities of 2, 4, 6, and 8 ($\times 10^{7}$) n/cm^{-3}. Indeed, when the simulation is repeated by adjusting the temporal span to control for the neutron exposure, we can see that the neutron den-

[2]Such as dilution by periodic mixing due to the PDCZ, the fact that neutron density is not constant and that its rate of change depends, among other things, on the ^{13}C abundance.

sity alone accounts for differences in specific abundance ratios, such as [Rb/Sr] or [Cs/Ba], with higher neutron densities turning the ratios from negative to positive. An illustrative example of this can be seen in Figure 4.6.

The first notable difference between Figures 4.5 and 4.6 is that in the latter, the ratio [hs/ls] is more stable than in the former one. This ratio represents the overproduction of the elements in the second *s*-process peak over the first peak ones, that is, the elements in the *s*-process abundance distribution with isotopes containing a magic number of neutrons, such as Rb, Sr, Y, and Zr (first peak, represented by [ls/Fe]) or Ba, La, Ce, Pr, and Nd (second peak, represented by [hs/Fe]). The [hs/ls] ratio depends mainly on the neutron exposure, while the specific element abundance in each peak is dominated by the neutron density.

To understand why does the [hs/ls] depend on the neutron exposure, it is enough to recall that the probability of a given neutron capture in relation to any other is proportional to the neutron density, the target abundance (in number fraction) and the cross section value for the capture itself. For identical neutron densities, the isotopes with a magic number of neutrons require to reach a higher abundance to be able to capture neutrons as a consequence of the lower neutron capture cross section. This means that, as the nucleosynthesis progresses, it will first stop advancing towards heavier elements until it produces enough of the first *s*-process peak, then the second, and lastly the third one (around Pb). Higher neutron exposures mean that there are more free neutrons available for the capture reactions, increasing the overall *s*-process abundance and allowing for the second and third peaks to be reached (Clayton et al. 1961). This ratio depends as well on mass (Karakas & Lattanzio 2014) and metallicity (Busso et al. 2001). The first of these dependences comes from the ^{22}Ne activation, as more massive stars activate this high neutron density and low neutron exposure source, enhancing the production of the first *s*-process peak over the second or third ones. The metallicity dependence is tied to the fact that the ^{13}C abundance is primary (that is, independent of metallicity) while the heavy element seeds that capture the neutrons are not. The consequence is that for similar physical conditions the neutron density is higher, effectively increasing the neutron exposure for *s*-process nucleosynthesis (Clayton 1988).

The dependence of the elemental ratios with the neutron density can be explained by considering the branching points of the *s*-process nucleosynthesis. That is, the isotopes for which the nucleosynthesis path can follow either a neutron capture or a decay with comparable probability. Particularly, for any given unstable isotope it is possible to calculate the probability of a neutron

capture over a decay by applying the expression

$$1 - P_{\rm Decay} = 1 - \frac{\lambda_{\rm Decay}}{n\sigma(T) + \lambda_{\rm Decay}}, \tag{4.2.1}$$

where $P_{\rm Decay}$ is the decay probability, $\lambda_{\rm Decay}$ is the decay rate, and $\lambda_n = n\sigma(T)$ is the neutron capture rate, which depends on the temperature and neutron density. As an example, for ^{87}Rb to be produced, either ^{85}Kr or ^{86}Rb need to capture a neutron before decaying[3] (see e.g., Käppeler et al. 2010). By using Equation (4.2.1) for a temperature of 100 MK, we can obtain the probability for either ^{85}Kr or ^{86}Rb capturing a neutron before decaying for different neutron densities. The probabilities resulting from such calculation are detailed in Table 4.3, where the resulting probabilities along with the low neutron capture cross section of ^{87}Rb (magic number of neutrons n = 50) help to understand the overproduction of [Rb/Fe] over [Sr/Fe] for higher neutron densities.

n/cm^3	^{85}Kr	^{86}Rb
1×10^6	0.67%	0.03%
4×10^7	21.16%	1.05%
1×10^9	87.03%	20.99%
1×10^{12}	99.99%	99.62%

TABLE 4.3— Equation 4.2.1 applied for ^{85}Kr and ^{86}Rb for different neutron densities at a temperature of 100 MK. The low probabilities in the first two rows indicate that these paths can only be significantly activated at higher neutron densities.

Similar branching points to that of the ^{85}Kr exist for other isotopes, such as ^{134}Cs, which is responsible for the Cs peaking over Ba at high neutron densities.

Finally, the remaining differences are explained by the total integration time itself. Specifically, for the 10^{12} n/cm^3 case we had to use an integration time of 0.06 years in order to keep the neutron exposure at 0.24 mbarn^{-1}. Given that there are unstable isotopes with much longer half-lives than 0.06 years, such as ^{90}Sr or ^{135}Cs, this means that the other cases with lower neutron density and larger integration times (from a thousand to a million times higher), have allowed for these unstable isotopes to decay during their production, modifying the resulting abundances distribution. In order to develop an understanding of this mechanism, we modify the experiment for the 10^{12} n/cm^3 case in a similar fashion to the approach taken by Hampel et al. (2016) in which, after

[3] One has to be careful when dealing with ^{85}Kr due to the different decay rates of its ground and metastable states (see e.g., van Raai et al. 2012), while here we are detailing the probabilities for the ground state of ^{85}Kr only.

the neutron capture integration, neutrons are kept to 0 for a period of time to allow for decaying isotopes to evolve. The results of this experiment for a decay time of 6×10^4 years, which is the integration time for the 10^6 n/cm^3 case, are presented in Figure 4.7. In this figure, the effects of the decay processes on several elements are clear, including an increase in both Rb and Nb (Z = 41). We return to this last element behavior in a future section, when comparing our simulations to those of other nucleosynthesis codes.

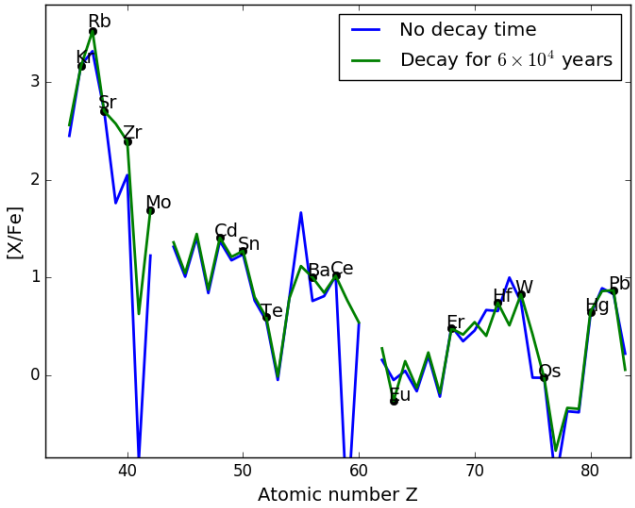

FIGURE 4.7— Similar to Figure 4.6, with the same neutron exposure and a neutron density of 10^{12} n/cm^3 but allowing for a subsequent decay time with a neutron density of 0 for one of the calculations, represented in green.

The latter figures can be used as an additional test for SNUPPAT. Indeed, by looking at Figures 4.5 and 4.6, we find that the ratio [hs/ls] appears to be more sensible to changes in both the neutron density and exposure than to changes in only neutron density. In fact, we can observe how that ratio goes from approximately -1 to almost -2 and up to 0 in the cases for 2×10^7, 4×10^7 and 8×10^7 n/cm^3, corresponding to a neutron exposure of 0.12, 0.24 and 0.49 mbarn^{-1} respectively. These values are very similar to those

found by Herwig et al. (2003), confirming the consistency of the SNUPPAT nucleosynthesis calculations with known results in the literature.

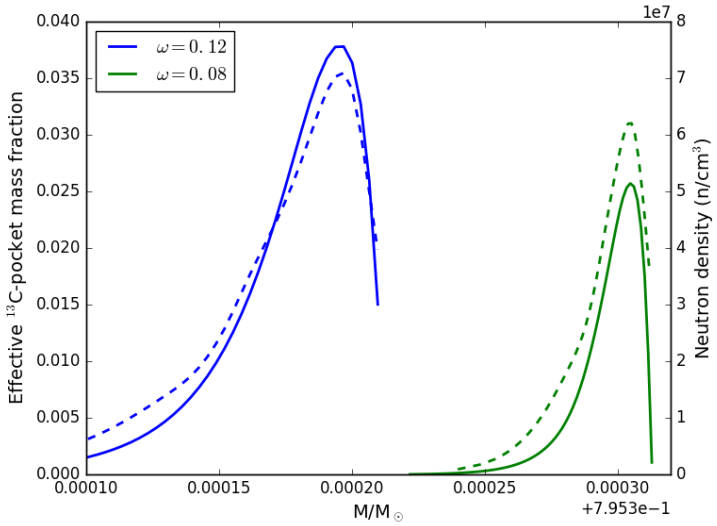

FIGURE 4.8— Mass fraction of the effective ^{13}C pocket as defined in the text (solid lines) along with the neutron density generated by each pocket (dashed lines) for two simulations with different free overshooting parameter ω. The neutron density is the quantity largely responsible for the *s*-process distribution in each mass coordinate to be later dredged-up to the stellar surface.

To analyze the effects of the parameter ω on the ^{13}C neutron source, we display in Figure 4.8 the effective ^{13}C pocket mass fraction of two simulations that only differ in that parameter. We can see that the pocket depth, height, and width increases with the overshooting parameter. This, again, allows us to predict a higher nucleosynthesis production and a change in the abundance distribution on the stellar surface.

The effects of the different overshooting parameters on the final abundances of a 4 $M_\odot$ simulation at solar metallicity can be seen in Figure 4.9. Following the previous analysis we find that, as expected, the boundless case results in higher abundances than the bounded case for the same overshooting parameter. Likewise, the abundances grow as well with ω due to a larger effective ^{13}C pocket

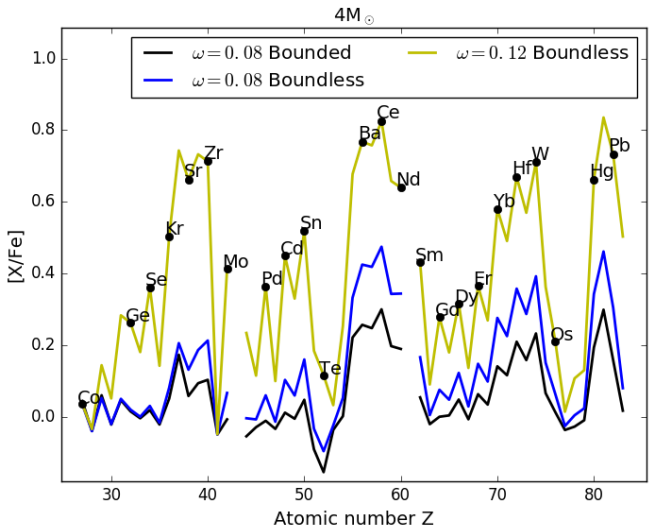

FIGURE 4.9— Final stellar surface abundances for three 4 $M_{\odot}$ solar metallicity simulations used in the previous examples on the cut-off velocity and free parameter values for the extra-mixing algorithm.

and a greater TDU efficiency.

There is a final interaction between the overshooting mechanisms and the formation of an effective ^{13}C pocket (as described by Goriely & Siess 2004), in which the ^{13}C pocket is completely contained inside the ^{14}N pocket if the overshooting parameter is large enough in a high temperature environment. In essence, Goriely & Siess (2004) argue that the ^{13}C pocket formation can take place under two different regimes: one in which the temperature is lower than $\sim$ 50 MK, and another one in which it is higher. In the lower temperature situation, protons are mixed into the intershell leaving a proton profile which can then burn undisturbed by mixing processes, generating the ^{13}C pocket profile we have previously described. On the other hand, if the temperature is high enough the proton burning can take place at the same time that it is being mixed into the intershell. The mixing processes can then modify the ^{13}C and ^{14}N pocket profiles in such a way that the ^{13}C pocket ends up contained

inside the ^{14}N pocket, inhibiting the ^{13}C neutron source altogether. If the overshooting parameter is low enough, then the protons may not be diffused into a high temperature region, allowing for the formation of a smaller ^{13}C pocket.

In the case of SNUPPAT, however, the overshooting mechanism is not modelled via a diffusion equation. This means that the rate of change on a species abundance in a given mass shell does not depend on the local second derivative but on the difference in abundance that particular mass shell has with the convective region. The consequence of this is that, although the mixing and burning do have comparable timescales, the neighboring shells to each pocket maximum can only affect each other after modifying the envelope value. Knowing that the envelope is many times more massive than the overshooted region, this means that each mass shell abundance is essentially independent of its neighbors. This independence ensures that the ^{13}C pocket keeps forming partially outside of the ^{14}N pocket region, allowing for the activation of the ^{13}C neutron source. Nevertheless, we should point out that this process still has a minor effect on our ^{13}C pocket, shrinking it by mixing some of its abundance to the envelope instead of diffusing it into the ^{14}N pocket, as is the case with diffusive overshooting.

Finally, we must consider how much freedom do we have when selecting the overshooting parameters for the extra-mixing processes at the bottom of the convective envelope and the PDCZ. On one hand, ATON applies the same overshooting parameter ($\omega = 0.002$) to every convective-radiative interface. On the other hand, we find no evidence of meaningful ^{13}C pocket formation or surface abundances for such a low value. Given that the extra-mixing at the bottom of the PDCZ has a significant effect in the stellar evolution, we have chosen to experiment exclusively with the overshooting parameter at the bottom of the convective envelope. Indeed, all results presented so far, including those shown in Figure 4.9, have been calculated with the same overshooting parameter for extra-mixing at the bottom of the PDCZ of $\omega = 0.002$. This is the case as well for the remaining of this thesis work unless explicitly stated.

4.3 Results

In this Section we describe the results of *s*-process AGB stellar nucleosynthesis as calculated by SNUPPAT on ATON models of 3, 4, 5, and 6 $M_\odot$ at a solar metallicity of Z = 0.018. These results cover a relatively wide range of trials with different overshooting limits and parameters in SNUPPAT, as well as the presence or absence of PDCZ mixing in the ATON simulations. Out of all these simulations, those more extensively covered are the 3 and the 4 $M_\odot$ models due

to the relatively short time needed for the full calculation. Indeed, the lower limit is marked by the 4 $M_\odot$ runs, which can be completed in a mere 5 to 10 days when parallelizing it with 7 processes for a minimum of 840 hours of CPU time.

Taking into account that a numerical code such as SNUPPAT is under a constant state of improvement and testing, we consider our main results to be the ones arising from the latest batch of runs. However, in this latest group we do not have 6 $M_\odot$ runs, which are present in batches of previous versions. Therefore, we have decided to include the simulations of an older version for that specific mass. The only difference between these 6 $M_\odot$ runs and the previous ones is that the convective envelope overshooting in the 6 $M_\odot$ simulations is always bounded and there is no PDCZ overshooting active either in ATON nor in SNUPPAT.

4.3.1 3 $M_\odot$ simulations

For three solar masses we present a total of five simulations, four of which correspond to the last batch with overshooting at the bottom of the PDCZ and one belonging to the previous batch with overshooting exclusively at the bottom of the convective envelope. Of the four simulations from the last batch, two where calculated with a bounded overshooting, while the other two were calculated with a boundless overshooting[4]. In Table 4.4 we present the parameters common to all of the simulations from the last batch in the 20 TPs that have meaningful TDU events[5]. In this table we have added the dredged-up mass per TDU event as a common entry to all simulations. While strictly speaking the dredged-up mass depends both on the overshooting parameter and the bounded or boundless choice for the limit, in these 3 $M_\odot$ simulations, the difference in the dredged-up mass between the $\omega = 0.08$ model with bounded overshooting and $\omega = 0.14$ with boundless overshooting is just 1.5%, with a geometric average of the last 20 TDU events of about 1.3%. Therefore, we treat all of these simulations as having the same dredged-up mass per TDU event.

[4]Here we keep using the nomenclature introduced in the previous section where "bounded" overshooting means that we limit the overshooting with advective considerations and "boundless" overshooting means that we effectively do not limit the extent of the mixing zone at all.

[5]We classify a TDU event as meaningful by the impact it potentially has in the envelope abundances by looking at the M_D/M_E ratio. From Eq. (4.3.2), we can calculate that for a 3 dex intershell abundance to turn into a 1 dex surface abundance over 30 TDU events, we need a dredged-up mass to envelope mass ratio of at least 3×10^{-4}. With this in mind, we only include in this table TDU events with a dredged-up mass to envelope mass ratio of 10^{-4} or greater. In this case, it means that we leave out of the table the first 10 TPs.

TDU #	Max T	λ	M_D	M_C	M_E	M_D/M_E
1	290	0.23	1.7×10^{-3}	0.61	2.37	7.2×10^{-4}
2	292	0.30	2.3×10^{-3}	0.62	2.35	9.8×10^{-4}
3	293	0.36	2.8×10^{-3}	0.62	2.34	1.3×10^{-3}
4	297	0.40	3.2×10^{-3}	0.63	2.32	1.4×10^{-3}
5	300	0.50	4.0×10^{-3}	0.63	2.30	1.8×10^{-3}
6	302	0.50	4.1×10^{-3}	0.63	2.28	1.9×10^{-3}
7	305	0.62	5.0×10^{-3}	0.64	2.26	2.3×10^{-3}
8	306	0.61	5.3×10^{-3}	0.64	2.23	2.4×10^{-3}
9	310	0.56	4.8×10^{-3}	0.64	2.20	2.3×10^{-3}
10	311	0.63	5.2×10^{-3}	0.65	2.15	2.5×10^{-3}
11	312	0.67	5.5×10^{-3}	0.65	2.10	2.7×10^{-3}
12	315	0.20	1.6×10^{-3}	0.66	2.00	8.2×10^{-4}
13	316	0.08	5.7×10^{-4}	0.66	1.93	2.9×10^{-4}
14	304	0.10	6.0×10^{-4}	0.67	1.85	3.3×10^{-4}
15	305	0.08	4.9×10^{-4}	0.67	1.76	2.8×10^{-4}
16	304	0.09	5.0×10^{-4}	0.68	1.67	3.0×10^{-4}
17	306	0.10	5.5×10^{-4}	0.68	1.55	3.5×10^{-4}
18	307	0.09	4.9×10^{-4}	0.69	1.42	3.5×10^{-4}
19	307	0.09	5.0×10^{-4}	0.69	1.23	4.1×10^{-4}
20	308	0.05	2.8×10^{-4}	0.70	0.95	2.9×10^{-4}

TABLE 4.4— Model parameters common to all 3 $M_\odot$ results from the latest SNUPPAT version, with λ representing the TDU efficiency parameter. The maximum intershell temperature during each pulse (Max T) is expressed in MK. The dredged-up mass M_D, the core mass M_C, and the envelope mass M_E are expressed in solar masses.

This table is a useful tool to understand the relationship between the stellar surface abundances and the nucleosynthesis taking place in the He intershell. As an example, after any TP in which the intershell abundances amount to Y_{IS} and the envelope abundances to Y_E, we can calculate the envelope abundances after the TDU, Y_{Ef} with the simple relation

$$Y_{Ef} = \frac{M_D}{M_E}(Y_{IS} - Y_E) + Y_E. \tag{4.3.1}$$

Bearing in mind that all the runs start with identical Y_{E0} and have the same M_D/M_E at each TDU, the only difference between the envelope abundances will come from the intershell abundances Y_{IS}. By assuming a constant Y_{IS} and M_D/M_E, one can calculate the stellar surface abundance after k TDU events

Y_{Ek} with the relation

$$Y_{Ek} = Y_{IS} + (Y_{E0} - Y_{IS}) \left(1 - \frac{M_D}{M_E}\right)^k .$$

Which, knowing that $M_D/M_E << 1$, can be approximated by

$$\frac{Y_{Ek}}{Y_{E0}} \approx 1 + k \frac{Y_{IS}}{Y_{E0}} \frac{M_D}{M_E}. \tag{4.3.2}$$

For large enough values of the second addend in the right-hand side of the equation (that is, for a surface abundance above 0.7 dex) we can ignore the 1, which allows us to calculate the abundances in the envelope from the abundances in the intershell as

$$\log_{10}\left(\frac{Y_{Ek}}{Y_{E0}}\right) \approx \log_{10}\left(\frac{Y_{IS}}{Y_{E0}}\right) + \log_{10}\left(k\frac{M_D}{M_E}\right). \tag{4.3.3}$$

If we plug in this equation $k = 20$ and the geometric mean of the M_D/M_E from Table 4.4, which is 8×10^{-4}, we then get that the stellar surface abundances should be around 1.8 dex lower than those of the intershell. At any rate, however, this represents an ideal case in which the intershell abundances are the same for each TDU event. Therefore, we must understand Eq. (4.3.3) as a tool for a first order guess on the dredge-up efficiency[6].

The value Y_{IS} itself depends on the abundances generated in the ^{13}C pocket and diluted into the PDCZ where, if the temperature conditions are met, the ^{22}Ne neutron source can be activated as well, modifying them. Given that in most situations not all the mass shells affected by the PDCZ are ingested by the envelope, the dilution produced by that convective mixing prevents a significant fraction of the nucleosynthesis products to be dredged-up to the surface. This situation is accounted for in Eq. (4.3.1) by taking Y_{IS} to be the abundance left after the PDCZ disappears.

A summary of the results for these 3 $M_\odot$ models is presented in Table 4.5, with the complete final stellar surface abundances represented in Figure 4.10. At first glance, we see that all abundances grow with the overshooting parameter ω, both in the intershell and at the stellar surface, as expected. It is worth noting that as the overshooting parameter increases, the [Rb/Sr] ratio decreases, going from a barely positive 0.01 for $\omega = 0.08$ to -0.21 for $\omega = 0.14$. This ratio is indicative of the overall predominant neutron density during the *s*-process nucleosynthesis, with the negative values being characteristic of the low

[6]This calculation can be extrapolated to [X/Fe] values as long as the initial abundance is reasonably homogeneous at the beginning of the simulation.

ω	[Rb/Fe]	[Sr/Fe]	[Ba/Fe]	[Pb/Fe]	[hs/ls]	[Pb/hs]
$0.08^{a,b}$	1.26, 0.06	1.77, 0.06	2.23, 0.31	1.52, 0.11	0.21	-0.19
0.08^{a}	1.28, 0.06	1.77, 0.06	2.26, 0.31	1.58, 0.11	0.21	-0.19
0.10^{a}	1.38, 0.07	1.85, 0.09	2.33, 0.40	1.69, 0.17	0.26	-0.22
0.12	1.58, 0.13	1.97, 0.28	2.44, 0.71	1.88, 0.38	0.35	-0.32
0.14	1.61, 0.16	2.01, 0.37	2.45, 0.82	1.95, 0.49	0.37	-0.32

TABLE 4.5— Final stellar surface abundances for the four 3 $M_\odot$ simulations from SNUPPAT and a comparison run without PDCZ overshooting. The first column lists the overshooting parameter ω used, with the superscript a indicating those simulations in which the overshooting was bounded and the superscript b indicating the simulation without PDCZ overshooting. From the second to the fifth columns, two values for each abundance are present: the intershell value after the PDCZ disappears and the stellar surface abundance. The sixth column lists the surface [hs/ls] values as defined by Karakas & Lattanzio (2014), that is, we take [ls/Fe] to be the average of [Sr/Fe], [Y/Fe] and [Zr/Fe], and [hs/Fe] to be the average of [Ba/Fe], [La/Fe] and [Ce/Fe]. Finally, the seventh column represents the stellar surface value for [Pb/hs].

neutron density distinctive of the ^{13}C neutron source (see e.g., van Raai et al. 2012). This behavior is confirmed in our models as the maximum temperature reached in each TP is barely enough to activate efficiently the ^{22}Ne source. Therefore, the nucleosynthesis products must come predominantly from the ^{13}C neutron source in those simulations with higher overshooting parameter.

In Figure 4.11 we display the evolution of the effective ^{13}C pocket profile for each one of the simulations plotted in Figure 4.10. As expected, the profiles are wider with increasing overshooting parameter, with the widest profile having a size of about 5×10^{-5} $M_\odot$ in the bounded $\omega = 0.08$ simulation to a size of 10^{-3} $M_\odot$ for the boundless $\omega = 0.14$ result. Also, we find that the height of the profiles appears to be independent from the overshooting parameter, while showing a dependence with time. Indeed, the maximum height of the effective ^{13}C pocket changes as the simulation evolves. The relationship of the profile width with time is more complex, as in all cases it appears to begin widening in the first three to five interpulses to then become narrower up to the last 8 interpulse periods, in which it becomes larger again. These differences are linked to a change in the stellar structure, specifically, a change in the pressure gradient of the intershell where the overshooting profile develops. From Eq. (3.2.1) we know that the extent of the overshooting grows with a lower pressure gradient in absolute value.

An additional metric of interest is the [hs/ls] value, positive for all of these simulations. As previously discussed, this ratio measures the relative abundance of the heavy and light *s*-process elements, with the advantage of being reasonably independent of the mixing efficiency into the convective envelope.

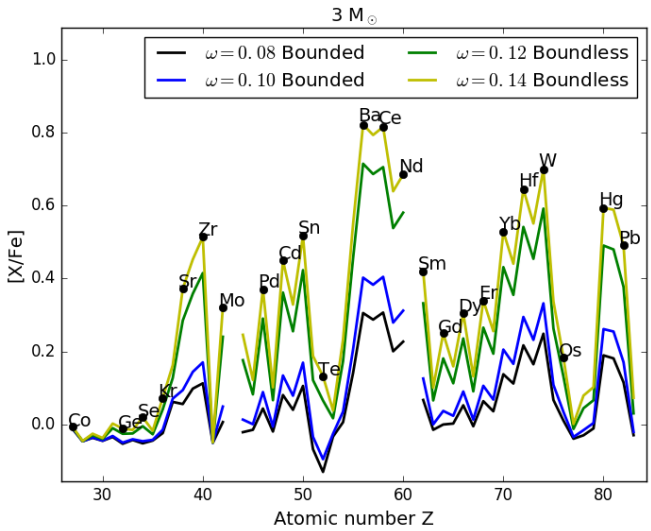

FIGURE 4.10— Final stellar surface abundances for the 3 $M_\odot$ SNUPPAT simulations at solar metallicity presented in Table 4.5. Because both $\omega = 0.08$ results are visually identical, we only present four lines in this figure. The [Rb/Sr] ratio indicates a predominant low neutron density source, compatible with the ^{13}C neutron source. On the other hand, the high [hs/ls] ratio is consistent with a high neutron exposure.

Recalling from before that this ratio is connected to the neutron exposure, with positive values associated with high neutron exposures, we can conclude that for these simulations that must be the case. Furthermore, the [hs/ls] ratio grows mildly when going from bounded to boundless overshooting which, without the presence of the ^{22}Ne neutron source, must only depend on the free neutrons produced by the effective ^{13}C pocket. Seeing from Figure 4.11 that the effective pockets grow the most when going from bounded to boundless overshooting, this behavior of the [hs/ls] ratio is expected.

Finally, we turn our attention to the simulation without PDCZ overshooting, presented in Table 4.5 along with the runs from the last batch. This simulation can be directly compared with the $\omega = 0.08$ run with overshooting at the bottom of the PDCZ to find that, in this case, the activation of PDCZ overshooting does

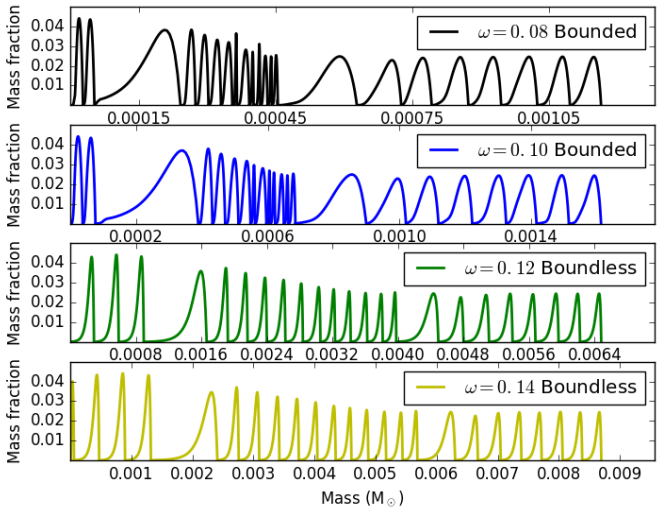

FIGURE 4.11— Evolution of the effective ^{13}C pocket profile in the 3 $M_\odot$ simulations. From each interpulse period, the profile with the highest valued maximum (that is, before the ^{13}C starts to burn) is selected and plotted. The x-axis has been modified to accommodate all pockets within a reasonable scale while at the same time accurately representing their size in units of $M_\odot$. The temporal evolution goes from left to right.

not affect the final abundances. This is expected, as neither the ^{22}Ne source is active in these models nor the TDU efficiency shows a significant change, as previously discussed.

4.3.2 4 $M_\odot$ simulations

The 4 $M_\odot$ simulations are those for which we have run the largest number of SNUPPAT models. The reason for this is that these models are by far the fastest to compute for us and, therefore, have been subject to the great majority of the tests conducted in this PhD work. In this case we present a total of eight results, six of which belong to the latest batch with overshooting at the bottom of the PDCZ. Of these six simulations, two of them were calculated with bounded overshooting while the other four were calculated with the boundless variant.

As in the previously case, we study first the physical variables to gain insight common to all of the six latest runs. A breakdown of these variables by TDU event is shown in Table 4.6. We again treat all dredged-up masses as equal for all the models, because the differences between the minimum and maximum ω usually remain below a 10% per pulse.

TDU #	Max T	λ	M_D	M_C	M_E	M_D/M_E
1	300	0.22	6.3×10^{-4}	0.80	3.12	3.0×10^{-4}
2	305	0.31	9.6×10^{-4}	0.80	3.09	4.2×10^{-4}
3	308	0.42	1.4×10^{-3}	0.80	3.06	5.3×10^{-4}
4	312	0.49	1.8×10^{-3}	0.80	3.02	6.2×10^{-4}
5	316	0.54	2.1×10^{-3}	0.81	2.97	7.2×10^{-4}
6	319	0.43	1.3×10^{-3}	0.81	2.89	4.6×10^{-4}
7	323	0.49	1.5×10^{-3}	0.81	2.79	9.5×10^{-4}
8	326	0.62	2.4×10^{-3}	0.81	2.69	8.6×10^{-4}
9	329	0.55	1.7×10^{-3}	0.81	2.58	6.6×10^{-4}
10	332	0.60	1.9×10^{-3}	0.81	2.45	1.1×10^{-3}
11	335	0.61	1.9×10^{-3}	0.81	2.28	8.5×10^{-4}
12	339	0.67	2.4×10^{-3}	0.82	2.02	1.2×10^{-3}
13	341	0.61	1.9×10^{-3}	0.82	1.68	2.1×10^{-3}
14	343	0.62	2.1×10^{-3}	0.82	1.46	1.4×10^{-3}
15	348	0.63	2.6×10^{-3}	0.82	1.24	2.1×10^{-3}
16	346	0.49	1.6×10^{-3}	0.82	1.04	1.6×10^{-3}
17	341	0.46	1.3×10^{-3}	0.82	0.89	1.6×10^{-3}
18	348	0.59	1.8×10^{-3}	0.82	0.74	2.5×10^{-3}

TABLE 4.6— Same as Table 4.4 for the 4 $M_\odot$ runs with PDCZ overshooting.

A first look to Table 4.6 tell us that there are important differences with respect to the 3 $M_\odot$ simulations. First, the maximum temperature in the intershell is higher in the 4 $M_\odot$ models, leaving no doubt on the activation of the ^{22}Ne neutron source. There are also less TPs with a meaningful TDU event and, although it dredges-up less mass in total, the rapid decrease of the envelope mass means that the average M_D/M_E ratio is remarkably similar, with a geometric mean of 9.4×10^{-4}. Thus, when applying Eq. (4.3.3), we obtain a very similar result with approximately 1.8 dex less in the surface abundances when compared with the intershell ones.

Table 4.7 summarizes the intershell and surface chemistry for the selected 4 $M_\odot$ runs. Comparing these abundances with those in Table 4.5, the ratio [Rb/Sr] is clearly higher than in the 3 $M_\odot$ results, spanning the range from 0.03

ω	[Rb/Fe]	[Sr/Fe]	[Ba/Fe]	[Pb/Fe]	[hs/ls]	[Pb/hs]
$0.02^{a,b}$	1.55, 0.15	1.41, 0.02	1.06, 0.02	0.70, 0.00	-0.02	-0.01
$0.08^{a,b}$	1.66, 0.19	1.57, 0.06	1.77, 0.19	1.39, 0.06	0.11	-0.13
0.08^{a}	2.02, 0.24	2.03, 0.21	2.23, 0.20	1.99, 0.12	0.01	-0.08
0.08	1.94, 0.21	1.86, 0.13	2.25, 0.42	2.05, 0.24	0.26	-0.14
0.10^{a}	2.07, 0.26	1.99, 0.13	2.36, 0.32	2.07, 0.22	0.18	-0.11
0.10	2.16, 0.33	2.10, 0.27	2.35, 0.56	2.22, 0.27	0.27	-0.13
0.12	2.41, 0.74	2.56, 0.66	2.55, 0.77	2.44, 0.73	0.08	-0.05
0.14	2.55, 1.16	2.75, 1.04	3.04, 1.29	2.89, 1.19	0.13	-0.08

TABLE 4.7— Same as Table 4.5 for the eight selected 4 $M_{\odot}$ simulations. The superscript *a* indicates those simulations with bounded overshooting and the superscript *b* indicates those simulations without PDCZ overshooting.

to 0.13. In contrast, in the 3 $M_{\odot}$ models, the highest [Rb/Sr] ratio is 0.01 while the lowest one reaches a value of -0.21. This fact indicates that higher neutron densities are attained in the stellar interior, as a consequence of the ^{22}Ne neutron source activation. Moreover, in at least four of the simulations (the two runs without overshooting in the PDCZ, and both the simulation with $\omega = 0.12$ and the one with $\omega = 0.14$), the [hs/ls] ratio is lower as well, which indicates that for those 4 $M_{\odot}$ runs the neutron exposure is lower than in the less massive ones. In the 4 $M_{\odot}$ case, the neutron exposure is the overall contribution of both neutron sources, which combines the low neutron exposure from the ^{22}Ne neutron source with the high neutron exposure from the ^{13}C neutron source. The explanation for this difference in the [hs/ls] ratio can be separated in two broad cases: i) for the high convective envelope overshooting parameter cases, such as the $\omega = 0.12$ and the $\omega = 0.14$ ones, the larger ^{14}N pocket is mixed with the ensuing PDCZ, boosting the ^{22}Ne abundance and increasing the production of this low exposure neutron source; and ii) conversely, for the simulations without PDCZ overshooting we propose that the difference is produced by smaller effective ^{13}C pockets, a consequence of the change in the stellar structure linked to this overshooting process. The smaller effective ^{13}C pockets combined with the generally poor nucleosynthesis (i.e., low overproduction factors) associated with bounded overshooting parameters lower than $\omega = 0.10$, produce the low [hs/ls] values obtained.

Further differences between the 3 $M_{\odot}$ and 4 $M_{\odot}$ simulations can be observed in Figure 4.12, where we plot the total stellar surface abundances for the runs summarized in Table 4.7. The activation of the ^{22}Ne neutron source is confirmed by the differences in a number of abundance ratios such as the already discussed [Rb/Sr] ratio but also others like the [Kr/Sr], [Pb/Hg], and [Cs/Ba] ratios,

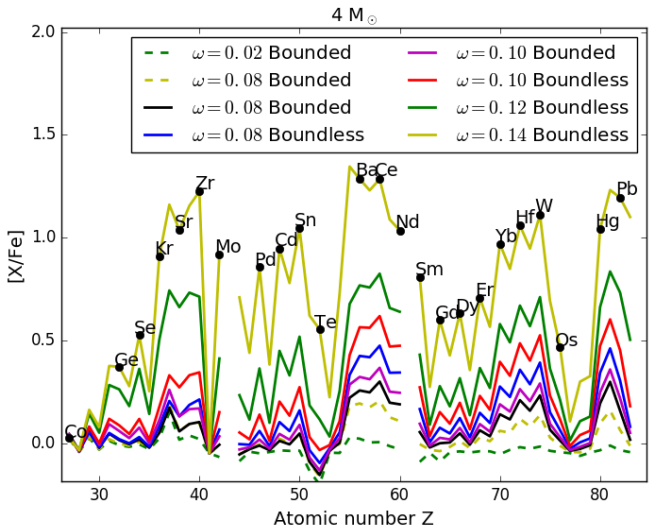

FIGURE 4.12— Final stellar surface abundances for the models summarized in Table 4.7. The dashed lines correspond to those simulations performed without PDCZ overshooting.

which directly depend on the neutron density at the *s*-process site. For example, Liu et al. (2014) associate a [Cs/Ba]> 0 with the ^{22}Ne neutron source and we find that a neutron density of 10^9 n/cm^3 or higher is needed for this ratio to be positive. Interestingly, as Figure 4.7 shows, the precise value for the [Cs/Ba] ratio depends not only on the neutron density but also on the time allowed for decay after the isotopes formation. Therefore, we find that the [Cs/Ba] is not only a good indicator of the total neutron density, but also of the time between thermal pulses and the total AGB lifetime.

The Figure 4.13 shows the effective ^{13}C pocket profile variations with each interpulse for a selected subset of the 4 M$_\odot$ simulations. In particular, we have included the values for one run with bounded overshooting mechanism and its boundless counterpart, as well as the two simulations yielding the highest stellar surface abundances. We observe once more in this Figure the expected correlation between profile width and overshooting parameter, with a 48% increase in its average from $\omega = 0.10$ to $\omega = 0.12$ and a 43% increase when going from

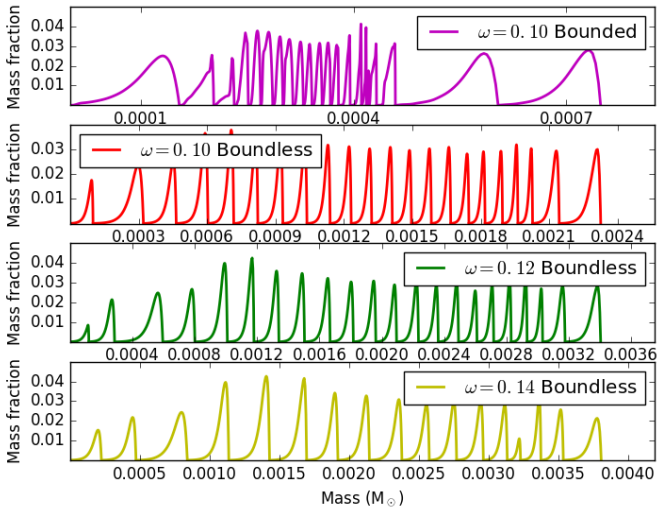

FIGURE 4.13— Same as Figure 4.11 but for the 4 $M_\odot$ simulations.

$\omega = 0.12$ to $\omega = 0.14$. This time, however, we find a dependence of the profile height with the overshooting parameter in some specific interpulse periods. It is to be noted here the subtle difference between the ^{13}C pocket profiles for 4 $M_\odot$ simulations and those found for the 3 $M_\odot$ ones (see Figure 4.11). Indeed, for the same overshooting parameter the effective ^{13}C pocket profiles are larger in the 3 $M_\odot$ simulations than in the 4 $M_\odot$ ones. For example, the average pocket size for the $\omega = 0.14$ runs is about 3.6×10^{-4} in the former and 2.2×10^{-4} in the latter.

Contrary to the 3 $M_\odot$ simulations, in the 4 $M_\odot$ case there is a significant difference when an extra-mixing mechanism at the bottom of the PDCZ is used. In particular, by comparing the $\omega = 0.08$ run with no PDCZ overshooting with the two other $\omega = 0.08$ runs, both in Table 4.7 and in Figure 4.12, the former shows lower abundances of the heavy *s*-process products [Ba/Fe] and [Pb/Fe], as well as a lower [hs/ls] ratio. Most of the differences can be explained by the contribution of smaller effective ^{13}C pockets and lower general dredged-up mass, which in both cases appear to be connected to the PDCZ overshooting,

as already explained. We note that one of the [hs/ls] in this trio of results is noticeably low. Specifically the $\omega = 0.08$ case with bounded convective overshooting and PDCZ overshooting. In this case the [hs/ls] ratio decreases with respect to the $\omega = 0.08$ case without PDCZ overshooting due to an enhance of the first *s*-process nucleosynthesis peak. We link this enhancement to a more efficient ^{22}Ne neutron source, linked with the PDCZ overshooting.

4.3.3 5 $M_\odot$ simulations

TDU #	Max T	λ	M_D	M_C	M_E	M_D/M_E
1	314	0.56	1.7×10^{-3}	0.87	3.62	4.7×10^{-4}
2	317	0.30	5.3×10^{-4}	0.87	3.52	1.5×10^{-4}
3	320	0.32	5.6×10^{-4}	0.87	3.38	1.7×10^{-4}
4	324	0.52	1.3×10^{-3}	0.88	3.19	4.0×10^{-4}
5	326	0.38	6.7×10^{-4}	0.88	3.02	2.2×10^{-4}
6	329	0.57	1.3×10^{-3}	0.88	2.80	4.8×10^{-4}
7	332	0.55	1.2×10^{-3}	0.88	2.55	4.9×10^{-4}
8	443	0.71	2.4×10^{-3}	0.88	2.24	1.1×10^{-3}
9	369	0.79	2.5×10^{-3}	0.88	2.02	1.3×10^{-3}
10	400	0.71	2.5×10^{-3}	0.88	1.77	1.4×10^{-3}
11	327	0.55	1.7×10^{-3}	0.88	1.56	1.1×10^{-3}
12	321	0.58	2.1×10^{-3}	0.88	1.42	1.4×10^{-3}
13	322	0.52	1.5×10^{-3}	0.89	1.32	1.1×10^{-3}
14	324	0.46	1.1×10^{-3}	0.89	1.22	8.8×10^{-4}
15	326	0.27	4.6×10^{-4}	0.89	1.13	4.1×10^{-4}
16	330	0.54	1.4×10^{-3}	0.89	1.04	1.4×10^{-3}
17	330	0.59	1.6×10^{-3}	0.89	0.95	1.7×10^{-3}
18	337	0.53	9.9×10^{-4}	0.89	0.87	1.1×10^{-3}
19	335	0.58	1.7×10^{-3}	0.89	0.79	2.1×10^{-3}
20	293	0.49	9.2×10^{-4}	0.89	0.72	1.3×10^{-3}

TABLE 4.8— Same as Table 4.4 for the 5 $M_\odot$ simulations.

We present a total of four simulations for the 5 $M_\odot$ models. Three with overshooting at the bottom of the PDCZ and one without it. All simulations with overshooting at the bottom of the PDCZ were conducted with boundless overshooting, with the other one having a bounded overshooting mechanism. Additionally, of the three simulations with overshooting at the bottom of the PDCZ, two of them were modified in order to disable the ^{13}C neutron source, following the analysis by Goriely & Siess (2004). For the first one, we chose

to suppress the formation of the ^{13}C pocket by disabling the extra-mixing at the bottom of the convective envelope, while for the second one we opted for modifying the reaction ^{13}C(α, n)^{16}O so that no neutrons were produced by it. Out of these two choices, the one more similar to the results from Goriely & Siess (2004) ought to be the second one, as the ^{14}N pocket is still formed and may potentially affect the ^{22}Ne neutron source. The parameters common to each simulation with PDCZ overshooting[7] are listed in Table 4.8.

We find a similar picture to that of the 4 $M_\odot$ simulations, with more relevant TDU events but lower M_D/M_E values in general, with an average of 7×10^{-4} that gives a factor between intershell and stellar surface abundances of about 1.9 dex. The main difference between the 4 and 5 $M_\odot$ stellar models is the maximum intershell temperatures. In the 5 $M_\odot$ models there are only three TPs with a maximum temperature higher than the maximum temperature reached by the 4 $M_\odot$ models. However, these three TPs do not substantially affect the final stellar surface abundances, which are very similar to those from the 4 $M_\odot$ simulations. The reason for this is that from the point at which the temperature peaks, there are 10 additional TPs with a temperature very similar to that found in the 4 $M_\odot$ case. In consequence, although some species from the first peak reach their maximum intershell value during these three TP and the [hs/ls] ratio arrives at its minimum, the subsequent pulses dilute this effect.

ω	[Rb/Fe]	[Sr/Fe]	[Ba/Fe]	[Pb/Fe]	[hs/ls]	[Pb/hs]
0.00	1.30, 0.10	1.18, -0.01	0.81, -0.03	0.82, -0.04	-0.02	-0.01
0.12^c	1.06, 0.08	0.93, -0.03	0.34, -0.03	0.21, -0.04	-0.01	0.00
0.08^{a,b}	2.02, 0.15	1.84, 0.03	1.95, 0.14	1.89, 0.08	0.09	-0.06
0.12	1.96, 0.41	2.00, 0.30	2.38, 0.55	2.14, 0.37	0.18	-0.18

TABLE 4.9— Same as Table 4.5 for the seven selected 5 $M_\odot$ simulations. The superscripts *a*, *b*, and *c* indicate the simulations with bounded overshooting, without PDCZ overshooting, and with the ^{13}C neutron source disabled, respectively.

Table 4.9 shows the stellar surface abundance summary for the four 5 $M_\odot$ simulations. By considering that at high overshooting parameters the ^{13}C pocket does not form, these four simulations allow us to evaluate the consequences of suppressing or allowing this neutron source for the final stellar surface abundances. In particular, we can see that the two models without the ^{13}C neutron source present an extremely low overproduction of *s*-process elements at the stellar surface. Interestingly enough, for the $\omega = 0$ simulation the signature of a higher exposure neutron source can be seen in the intershell.

[7] Except for the simulation without overshooting at the bottom of the convective envelope ($\omega = 0$). In this case, we expect a lower TDU efficiency.

We associate this with the formation of an extremely thin effective ^{13}C pocket of the order of 10^{-6} $M_{\odot}$ during the last 20 TPs. Finally, in the two simulations with ^{13}C pocket the [hs/ls] becomes positive and the overproduction of *s*-process elements is much higher, indicating an overall neutron exposure larger than in the simulations without the ^{13}C neutron source.

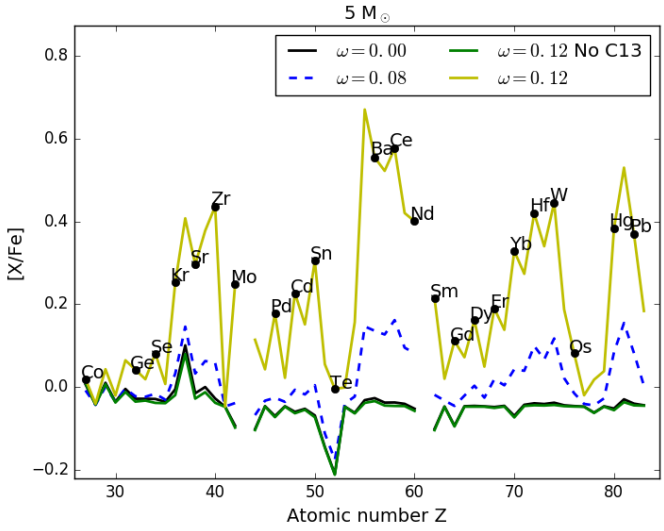

FIGURE 4.14— Final stellar surface abundances of the 5 $M_{\odot}$ SNUPPAT simulations at solar metallicity. The solution labeled with "No C13" refers to the simulation in which the ^{13}C neutron source was disabled. The dashed curve shows the abundances distribution for the simulation without PDCZ overshooting.

In Figure 4.14 the final stellar surface abundances for all elements above Fe are plotted for the four simulations discussed in this subsection. The similarities between the runs with no meaningful ^{13}C neutron source (black and green curves in Figure 4.14) are clear, along with the observation that no element beyond the first *s*-process peak is produced. Moreover, from these two curves we can say that the additional ^{14}N being introduced into the PDCZ from the mixing of the ^{14}N pocket in the $\omega = 0.12$ simulation does not boost the ^{22}Ne source neutron exposure enough to offset the small ^{13}C pocket generated in the $\omega = 0$

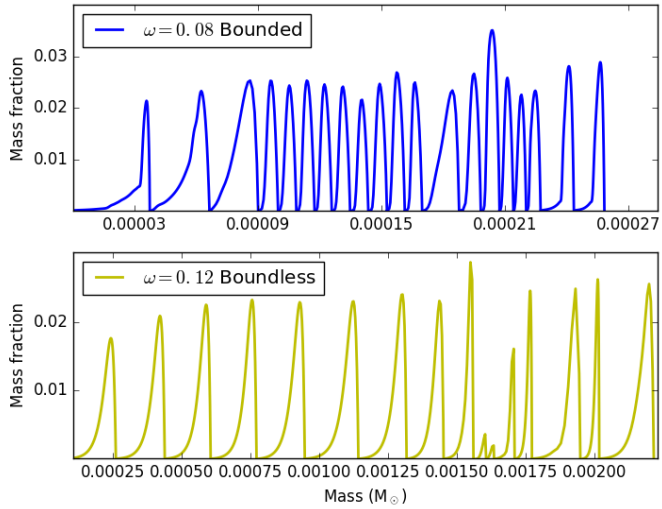

FIGURE 4.15— Same as Figure 4.11 but for the 5 $M_\odot$ simulations.

run.

For the two simulations in which the ^{13}C neutron source has not been eliminated, a higher *s*-process elements overproduction is clear, particularly in the second and third *s*-process peaks. The $\omega = 0.12$ overshooting case predicts a negative [Rb/Sr] ratio and an a remarkably high [Cs/Ba] ratio, which, as previously discussed, depends on the maximum neutron density and on the characteristic TP timescale and AGB lifetime. It is then reasonable to link the lower [Cs/Ba] ratio in the $\omega = 0.08$ simulation to a lower maximum neutron density than in the $\omega = 0.12$ case, which may be explained by the mixing of a smaller ^{14}N pocket into the PDCZ. Finally, we note that the *s*-element overproduction values for similar overshooting parameters in the 5 $M_\odot$ models are lower than in the 4 $M_\odot$ case. As a clear example, the [Sr/Fe] ratio at the stellar surface value goes from 0.66 to 0.30 dex in the $\omega = 0.12$ simulations for the 4 and 5 $M_\odot$ simulations, respectively. This brings the overproduction of the first *s*-process peak for the 5 $M_\odot$ simulation more in line with the 3 $M_\odot$ value of 0.28 dex for the same overshooting parameter.

In Figure 4.15 we have plotted the evolution of the effective ^{13}C pocket profile for a selection of the 5 $M_\odot$ simulations. Specifically we have left out the simulation without overshooting as well as the simulation in which the ^{13}C neutron source is switched off. First, we notice as usual the correlation between the profile width with the overshooting parameter. The average for the $\omega = 0.04$ case is 2.5×10^{-5} $M_\odot$ while for the $\omega = 0.12$ case is 1.3×10^{-4} $M_\odot$. We find as well that the 4 $M_\odot$ simulation with $\omega = 0.12$ has an average effective ^{13}C pocket profile width of 1.5×10^{-4}, slightly larger than the 5 $M_\odot$ case. In this occasion, we observe that both the height and width of the profiles are strongly affected by the overshooting parameter and evolutionary time, with almost no similarities between the $\omega = 0.08$ and the $\omega = 0.12$ runs.

4.3.4 6 $M_\odot$ simulations

We present a total of three simulations for the 6 $M_\odot$ models. These three runs were performed without overshooting at the bottom of the PDCZ and with bounded extra-mixing. As with previous cases, we present first the common parameters to all the simulations in Table 4.10.

TDU #	Max T	λ	M_D	M_C	M_E	M_D/M_E
1	334	0.17	5.0×10^{-4}	0.90	4.68	1.1×10^{-4}
2	329	0.38	6.3×10^{-4}	0.90	4.56	1.4×10^{-4}
3	324	0.29	3.8×10^{-4}	0.90	4.47	8.5×10^{-5}
4	324	0.36	5.2×10^{-4}	0.90	4.30	1.2×10^{-4}
5	327	0.41	6.1×10^{-4}	0.90	4.10	1.5×10^{-4}
6	332	0.43	6.4×10^{-4}	0.90	3.87	1.7×10^{-4}
7	373	0.48	7.4×10^{-4}	0.90	3.55	2.1×10^{-4}
8	340	0.44	7.2×10^{-4}	0.90	3.11	2.3×10^{-4}
9	335	0.48	6.2×10^{-4}	0.90	2.85	2.2×10^{-4}
10	340	0.41	5.6×10^{-4}	0.91	2.60	2.2×10^{-4}
11	340	0.44	6.1×10^{-4}	0.91	2.36	2.6×10^{-4}
12	344	0.43	6.4×10^{-4}	0.91	2.16	3.0×10^{-4}
13	350	0.70	1.7×10^{-3}	0.91	1.98	8.6×10^{-4}
14	342	0.53	9.0×10^{-4}	0.91	1.81	5.0×10^{-4}
15	362	0.35	5.1×10^{-4}	0.91	1.63	3.1×10^{-4}
16	352	0.42	7.0×10^{-4}	0.91	1.51	4.6×10^{-4}
17	278	0.41	5.8×10^{-4}	0.91	1.38	4.2×10^{-4}

TABLE 4.10— Same as Table 4.4 for the 6 $M_\odot$ simulations.

The main differences between this mass and the others are the temperature

ω	[Rb/Fe]	[Sr/Fe]	[Ba/Fe]	[Pb/Fe]	[hs/ls]	[Pb/hs]
0.02	2.09, 0.11	1.85, -0.01	1.62, 0.01	1.71, -0.01	0.01	-0.02
0.06	2.14, 0.14	1.95, 0.02	1.82, 0.09	1.99, 0.10	0.07	0.00
0.08	2.19, 0.15	2.06, 0.04	2.03, 0.14	2.19, 0.14	0.10	-0.01

TABLE 4.11— Same as Table 4.5 for the three 6 $M_\odot$ simulations.

and the dredge-up efficiency. In particular, almost every late TDU event has a maximum intershell temperature above 340 MK. At the same time the ratio M_D/M_E is the lowest of all the masses, with a geometric mean of 2×10^{-4} which, coupled with the low number of TDU events, nets us a 2.5 dex decrease from intershell to stellar surface abundances, assuming that such abundances are large enough to apply Eq. (4.3.3). This sharp decrease in the TDU efficiency comes from a combination of different factors such as a lower λ value, a smaller He intershell and, a larger envelope mass (see e.g., Karakas & Lattanzio 2014).

It should be noted here the high envelope mass at the end of the simulation. This is due to a halting of the evolutionary code arising from convergence problems in the AGB models. These convergence problems appear to be linked to the basic assumption that the stellar structure can be described by an hydrostatic equilibrium, and are not unique to ATON (see e.g., Lau et al. 2012). As a consequence of this halting, we expect for these runs to show considerably lower stellar surface abundances with respect to the other masses. Nevertheless, the intershell abundances are insightful enough to justify this Subsection.

Table 4.11 shows a summary of the intershell and final stellar surface abundances for the 6 $M_\odot$ simulations. The most similar of the previous simulations to these are, perhaps, those summarized in Table 4.9 for the 5 $M_\odot$ run without overshooting at the bottom of the PDCZ. Indeed, the stellar surface abundances for the species in Table 4.9 are close to the 6 $M_\odot$ values (Table 4.11). By considering the limitations of the 6 $M_\odot$ simulations mentioned above, this suggests that higher intershell abundances must be attained, as it seems to be the case. Moreover, the high intershell abundances for the 6 $M_\odot$ simulations are comparable to the intershell abundances found in simulations with higher ω values for lower masses. For example, for the 3 $M_\odot$ simulations, the intershell values for [Rb/Fe] and [Pb/Fe] are smaller in the $\omega = 0.14$ simulation with boundless overshooting than in the $\omega = 0.08$ 6 $M_\odot$ simulation with bounded overshooting. This behavior can be observed also in the 4 $M_\odot$ case, where we have to go to the $\omega = 0.10$ bounded case to find similar intershell results for Rb, Sr, and Pb.

4.4 Conclusions

In this chapter we have studied the repercussions of our extra-mixing implementation on the *s*-process nucleosynthesis, both for the ^{13}C and the ^{22}Ne neutron sources. We have also presented the SNUPPAT predictions as stellar surface overabundances.

First, we have studied the effect of extra-mixing at the bottom of the PDCZ. Given that this extra-mixing into the stellar core has an impact on the energy production of the star and, in consequence, the stellar evolution, we have studdied its effects both in the stellar evolutionary code ATON and in our post-processing code. We can divide the most important changes for the *s*-process nucleosynthesis that this mechanism introduces into those arising from the evolutionary code and those that directly impact the post-processing code. In the first group we find mainly the increase of the λ parameter and M_D/M_E TDU efficiencies. In the second group, the inclusion of core ^{12}C into the He intershell can enhance the ^{13}C neutron source.

After that, we have tackled the impact of convective envelope overshooting on the ^{13}C neutron source, and we have confirmed the well known result that without a convective envelope extra-mixing process, the main *s*-process component cannot activate even in carbon stars. We have described the free parameter ω and the overshooting limit, along with their impact on the formation of the effective ^{13}C pocket. We have also confirmed that our effective ^{13}C pocket does not disappear on its own in the more massive stellar models, explaining how this is a consequence of the choice of an advective overshooting mechanism instead of a diffusive one (Goriely & Siess 2004). We have also shown how deactivating this mechanism or the ^{13}C neutron source has clear impact on the stellar surface abundances distribution.

Finally, we have presented the SNUPPAT results for solar metallicity, and analyzed them on the basis of the introductory extra-mixing discussion. In this case we have been able to settle for an $\omega = 0.14$ *boundless* overshooting for the bottom of the convective envelope, by calibrating it with the expected [Ba/Fe] overproduction of ~ 1 dex in carbon AGB stars (Abia et al. 2002). These results have helped us confirm that the ^{22}Ne neutron source is active for relatively low-mass AGB models for the ATON-SNUPPAT simulations, when compared to other codes (see Chapter 5). Indeed, the activation of this source occurs at some point between the 3 and 4 $M_\odot$ cases.

5

Comparison with other nucleosynthesis codes

In this chapter we compare our results with those of other well known nucleosynthesis codes and attempt to give an explanation for the observed differences. The selected codes for this comparison are the MONASH code, FUNS/FRUITY and mppnp/NuGrid.

5.1 Introduction

This chapter places SNUPPAT results in context among other theoretical nucleosynthesis codes. In particular, we aim to compare our predictions with those from other *s*-process nucleosynthesis codes. Although no definitive knowledge on the real world can be gained without a comparison with astronomical observations (see Chapter 7), this exercise allows us to understand the place that SNUPPAT holds in the general theoretical paradigm to which we intend to contribute.

For this task we have decided to compare SNUPPAT with each code separately. We start with the MONASH version of the Mount Stromlo Sellar Structure Program (Karakas & Lugaro 2016), followed by the stellar surface nucleosynthesis abundances from the FRUITY database[1], and finally those from the NuGrid project (Pignatari et al. 2016).

5.2 MONASH

As previously stated, we start our comparisons with the MONASH stellar surface abundances. In order to conduct a meaningful conversation on the differ-

[1]The relevant references and database can be found at http://fruity.oa-abruzzo.inaf.it/

ences in nucleosynthesis results, we find it useful to present first the differences in the stellar evolution and post-processing treatments. In particular, in regards to the stellar evolutionary simulations, ATON uses the Blöcker mass loss during the AGB evolution (Blöcker 1995) while in MONASH the Vassiliadis & Wood (1993) mass loss is used. The other notable difference between ATON and other stellar evolution codes like MONASH is the convection method utilized, with the ATON models using the FST prescription (Canuto et al. 1996) complemented by a diffusive overshooting mechanism. On the other hand, in Karakas & Lugaro (2016) the mixing-length theory (MLT) recipe for convection is used with a solar calibrated parameter $\alpha = 1.86$ and no special overshooting treatment is applied[2].

From a post-processing point of view, the nuclear network used by Karakas & Lugaro (2016) is similar to ours, because it was Dr. Lugaro who provided us with the network used in SNUPPAT. The main difference is that since then, they have updated the network to include eight additional species, which may modify the behavior of isotopes from *s*-elements such as Hf, Cs or Eu. On the subject of overshooting, the SNUPPAT approach has been already described in detail in Chapter 3 and Section 4.2, while for the MONASH post-processing they use a partial-mixing zone (PMZ) method described in, for example, Buntain et al. (2017).

These differences translate to a variety of effects in the simulations. ATON models show Hot Bottom Burning (HBB) at a lower initial mass ($\sim$ 3.5 $M_{\odot}$, see Mazzitelli et al. 1999; Ventura et al. 2013) than the MONASH ($\sim$ 4 - 4.5 $M_{\odot}$, see Karakas & Lattanzio 2003) ones, lower parameter λ, and a similar to lower number of TPs. As a consequence of these differences, there is no unique correspondence between the range of stellar models presented in Karakas & Lugaro (2016) and the SNUPPAT results. Therefore, we have decided to match the models that show interesting similarities or differences, listing the simulation parameters and subsequently discussing the results. In order to conduct this systematic comparison, we subdivide our analysis by the SNUPPAT initial mass (i.e., 3, 4, and 5 $M_{\odot}$).

It is useful for us to describe now the parameter space in the Karakas & Lugaro (2016) models. Each model is characterized by four distinct parameters: initial mass, metallicity, M_{mix} and N_{ov}. The first two parameters are self-explanatory, and in this comparison we will fix the metallicity parameter to Z = 0.014, which is the closest available to our own Z = 0.018 metallicity value.

[2]In a few low-mass models, a direct extension of the convective border is sometimes applied as a first order overshooting mechanism, however. We explain why this mechanism is unimportant for us further in the text.

The M_{mix} parameter controls the extent of the PMZ below the convective envelope. The proton profile is calibrated in such a way that at the highest point of the PMZ, $X_p(0)$, equals the envelope value (~ 0.7) and at the bottom of the PMZ it has a value of $X_p(M_{mix}) = 10^{-4}$. In the standard case and when represented in a logarithmic scale, this profile is a straight line connecting these two points (Buntain et al. 2017). Knowing that the effective ^{13}C pocket is confined roughly to the region where $10^{-4} \leq X_p \leq 10^{-2}$ (see e.g., Goriely & Mowlavi 2000, Cristallo et al. 2009), it is reasonable then to expect the effective ^{13}C pocket to have an extension of roughly half the M_{mix} value.

Finally, the N_{ov} parameter controls the extent of the convective overshooting in pressure scale heights. The overshooting mechanism used in these models is a straightforward extension of the convective envelope by the amount indicated by the N_{ov} parameter (Kamath et al. 2012), and it is functionally independent of the PMZ. Nevertheless, this N_{ov} parameter is different than 0 in only a handful of low-mass cases ($M < 2\ M_\odot$), which are not used in the comparison. We have only included its description here for completeness.

In Figure 5.1, we display the two SNUPPAT 3 $M_\odot$ runs with higher overshooting parameters together with the most similar MONASH results both absolute abundance values and abundance distributions. The three selected MONASH models appear listed in Karakas (2014), were we find that the number of TPs on each model is 28, 23, and 41 for the 3, 4 and 5 $M_\odot$ models, respectively. With the same correspondence, the λ_{max} are 0.80, 0.96, and 0.95. On the other hand, the 3 $M_\odot$ ATON evolutionary model used in the SNUPPAT simulation displayed has a total of 30 TPs, of which around 23 form an effective ^{13}C pocket in SNUPPAT, and has a λ_{max} of 0.67.

The first thing that we should point out is that the three MONASH models presented here have a $M_{mix} = 10^{-4}\ M_\odot$. As we have previously discussed, this value should form effective ^{13}C pockets of size $\sim 5 \times 10^{-5}\ M_\odot$. This contrasts with the SNUPPAT average effective ^{13}C pocket sizes, which are $2.8 \times 10^{-4}\ M_\odot$ and $3.6 \times 10^{-4}\ M_\odot$, for $\omega = 0.12$ and $\omega = 0.14$ overshooting parameters, respectively.

The larger effective ^{13}C pocket sizes give SNUPPAT a higher neutron exposure, which is reflected in that the [hs/ls] index tends to be lower in the MONASH models, explaining some of the differences in abundance distributions between both codes. On the other hand, although the total *s*-elements overproduction is affected by neutron exposure as well, the larger λ_{max} of the MONASH models appears to compensate this effect in the surface abundances for the 4 and 5 $M_\odot$ cases. The net effect is that both nucleosynthesis codes are in agreement for the first *s*-process peak for the 3 and 4 $M_\odot$ MONASH cases, with the second peak for the 4 and 5 $M_\odot$ MONASH cases, and with the third

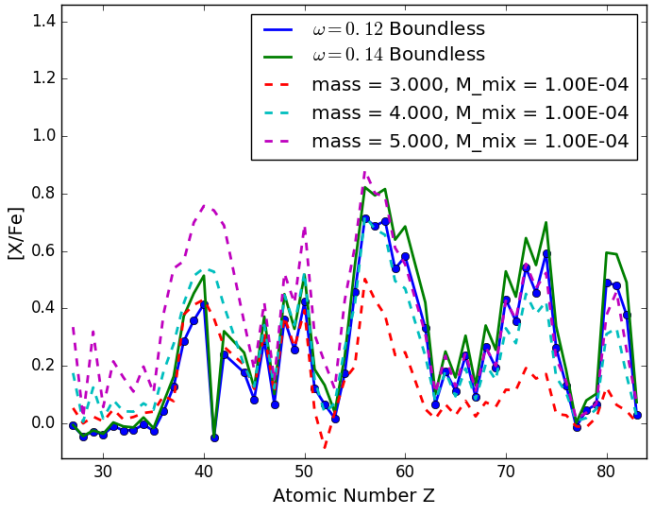

FIGURE 5.1— Final stellar surface abundances for both SNUPPAT (solid lines) and MONASH (dashed lines). The SNUPPAT runs chosen for the comparison correspond to those with higher overshooting parameters ω among the 3 $M_\odot$ simulations. The MONASH models chosen are those with final abundances most similar to SNUPPAT in both absolute abundance values and abundance distributions. Both the mass and M_{mix} labels from the MONASH models are expressed in solar masses.

peak with the 5 $M_\odot$ MONASH case.

Before continuing to the next mass, we now briefly address the remarkable difference in abundance of Nb (atomic number 41) between SNUPPAT and MONASH[3]. This discrepancy comes from the fact that Nb sits outside of the *s*-process path altogether, which goes from ^{90}Zr through to ^{95}Zr where it rapidly decays twice towards ^{95}Mo (see e.g., Figure 29 of Karakas & Lattanzio 2014). The only way to produce the stable ^{93}Nb isotope is through the decay of ^{93}Zr, which has a half-life of about 1.5×10^6 years, in a low neutron density environment (see e.g., Mathews et al. 1986, Bisterzo et al. 2006). The reason why MONASH models shows the ratio [Nb/Zr] ≈ 0 is because the authors have

[3]This difference in Nb is seen for all SNUPPAT and MONASH masses

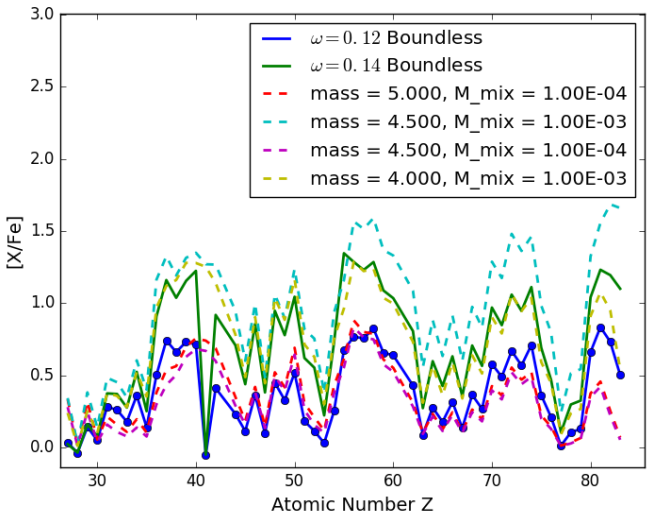

FIGURE 5.2— Same as Figure 5.1 for two SNUPPAT 4 $M_\odot$ simulations.

allowed for the decay of ^{93}Zr before presenting their stellar surface abundances results.

For the 4 $M_\odot$ SNUPPAT case (see Figure 5.2) we find a better agreement with the 4, 4.5, and 5 $M_\odot$ MONASH models. The stellar models have a very similar λ_{max} of about 0.95, with 23, 31, and 41 TPs, respectively. In contrast, the ATON model undergoes a total of 27 TPs, with a λ_{max} of 0.67. Finally, we have found that in this case the MONASH models with a M_{mix} of both 10^{-3} and 10^{-4} $M_\odot$ are close enough to the SNUPPAT results.

Regarding the SNUPPAT $\omega = 0.12$ simulation, we find the 4.5 and 5 $M_\odot$ MONASH models with $M_{mix} = 10^{-4}$ $M_\odot$ to show a similar abundance distribution in the first and second *s*-process peaks. This shows that the SNUPPAT model, with an average effective ^{13}C pocket size of about 1.7×10^{-4} $M_\odot$, may produce enough nucleosynthesis to compensate for the lower λ_{max}. Naturally, a larger ^{13}C pocket should correlate with a higher neutron exposure, which can be clearly seen in the higher SNUPPAT third peak.

Concerning the SNUPPAT $\omega = 0.14$ simulation, it is clear that the MONASH

models with $M_{mix} = 10^{-3}$ $M_\odot$ provide the best match. Both these MONASH models evidence a stark difference in the overall neutron exposure. Indeed, by comparing the first, second, and third *s*-process peaks, we can trivially arrange the three models by neutron exposure: First, the MONASH 4.5 $M_\odot$ case, followed by the SNUPPAT $\omega = 0.14$ simulation and finishing with the MONASH 4 $M_\odot$ case. In more detail, we notice that the first peak is quite similar in all of them, with the first apparent departure happening around the second peak for the 4.5 $M_\odot$ MONASH model. In the same vein, the third peak indicates that the SNUPPAT model has a higher neutron exposure than the 4 $M_\odot$ MONASH model. The differences in neutron exposure could be explained by a handful of mechanisms, such as the greater activation of the ^{22}Ne neutron source, or the diversity in the number of TPs for each model.

In the subject of the ^{22}Ne neutron source, and still dealing with the $M_{mix} = 10^{-3}$ MONASH cases, we can observe that the [Rb/Sr] ratio is lower in their 4 $M_\odot$ model. Particularly, we might recall that this high neutron density source activates during the TP if the He intershell reaches a temperature higher than 3×10^8 K; somewhere in the PDCZ. By noting the established relation between a positive [Rb/Sr] ratio and the ^{22}Ne neutron source, these results indicate that the ATON models reach higher temperatures during the TP at lower masses than the MONASH models. We believe this may correlate with the HBB appearing at a lower mass in ATON evolutionary models.

Finally, for the 5 $M_\odot$ case, we have selected from SNUPPAT a model representing the case with active ^{13}C neutron source and another model without ^{13}C. Accordingly, three MONASH models showing the best match with the SNUPPAT 5 $M_\odot$ simulations have been selected: A 4 and a 5 $M_\odot$ models with a M_{mix} of 10^{-4} $M_\odot$ and a 5 $M_\odot$ simulation with no PMZ. The number of TPs in the MONASH models goes from 23 for the 4 $M_\odot$ simulation to 41 for the 5 $M_\odot$ simulation, while the SNUPPAT simulation sits between the two with 34 TPs in total. Additionally, the 5 $M_\odot$ model with active ^{13}C neutron source has an average effective ^{13}C pocket size of 1.4×10^{-4} $M_\odot$.

From Figure 5.3 it can be seen that there is a clustering of the SNUPPAT and MONASH models around the activation of the ^{13}C pocket in SNUPPAT and the existence of a PMZ in MONASH. In the cases where the effective ^{13}C pocket is active or exists, we find that the MONASH 4 $M_\odot$ model results follows the SNUPPAT abundance distribution closely for the first and second *s*-process peaks. We have added the 5 $M_\odot$ MONASH model to specifically draw attention to the similarities in the [Rb/Sr] ratio, which indicates a relatively high neutron density peak, as already discussed. On the other hand, in the case where there is no PMZ present or the ^{13}C pocket is not active, the only relevant change in surface abundances can be found around Cu (Z = 29) and Te (Z = 52), both

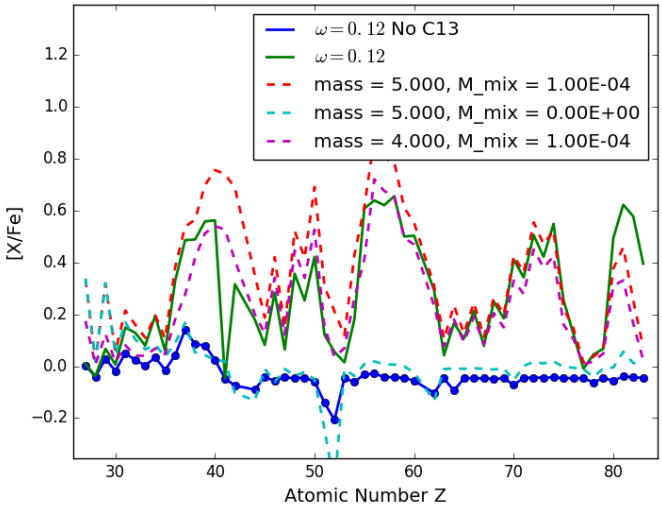

FIGURE 5.3— Same as Figure 5.1 for two SNUPPAT 5 $M_\odot$ simulations. The model marked with "No C13" refers to a simulation in which the ^{13}C neutron generating reaction was disabled.

discrepancies being linked to a difference in the neutron exposures for both types of models.

We focus in the case for Cu, having in mind that the same mechanism applies to elements such as Te and Co[4] (Z = 27). First, we note that this difference is clearly independent of the ^{13}C pocket. Indeed, both SNUPPAT simulations display equal Cu abundances, the same being true for both MONASH 5 $M_\odot$ cases. In the literature we find that the *s*-process nucleosynthesis of these two elements is associated with the ^{22}Ne neutron source (see e.g., Pignatari et al. 2010), which is consistent with its highest stellar surface overabundance appearing in both 5 $M_\odot$ MONASH models. This leaves us with the need to explain the lower production, akin to a MONASH 4 $M_\odot$ model, of these elements by SNUPPAT. In this regard, we have found that a nucleosynthesis numerical experiment with high neutron density is able to reproduce different [Rb/Cu] ratios

[4]Within the regime of low to no neutron exposure.

depending on the total neutron exposure. For example, by taking a neutron density of 10^{10} n/cm^3 at a temperature of 3.2×10^8 K, we find that a [Rb/Cu] ratio of 0.18 can be obtained after integrating for 0.2 years, while a ratio of -0.51 is the result of a one year integration, which translates into a neutron exposure 5 times higher. This behavior of the [Rb/Cu] ratio can be reproduced too at higher neutron densities such as 10^{12} n/cm^3, and temperatures as low as 10^8 K in which the ^{22}Ne neutron source does not activate[5].

The latter considerations lead us to propose that there is a fundamental difference in neutron exposure for the ^{22}Ne neutron source nucleosynthesis in the PDCZ between the SNUPPAT and the MONASH models. A possible explanation could lie in the specific interplay between the nucleosynthesis and convective timescales in this region. Moreover, and although we have in principle discarded this possibility after studying the relevant processes, this difference could arise from our treating of convective processes as an instantaneous mixing. The reason being that ^{22}Ne could be not replaced as frequently as it should during its burning in the PDCZ due to an estimation error on our part.

Finally, we must note that the MONASH models have been computed with a slightly higher metallicity than the one used in ATON and SNUPPAT. According to *s*-process nucleosynthesis theory, the neutron exposure and metallicity are negatively correlated (Clayton 1988). This means that the effect of this difference in metallicity should be one of a lower neutron exposure in the SNUPPAT stellar surface predictions when compared to the MONASH stellar surface abundances. However, we have not mentioned this fact during our previous discussion because the difference in metallicities is too small to have an impact on the surface abundances. We also extend this conclusion to all the other comparisons in the present chapter.

5.3 FRUITY

In this section we turn our attention to the results of the FUNS code (Straniero et al. 2006; Cristallo et al. 2009), which can be found in the FRUITY database. The FUNS evolutionary code follows the whole *s*-process network along with the stellar evolution and, therefore, we must compare it simultaneously to ATON and SNUPPAT. The main differences of this code with ATON are similar to those listed in the MONASH subsection. That is, the use of the MLT scheme for convection and the Vassiliadis & Wood (1993) mass loss prescription. Fur-

[5]It must be noted that we are not suggesting the nucleosynthesis of these elements can efficiently occur at this temperature. We have merely explored the parameter space (density and temperature) to ensure that this ratio is reproduced well within the expected values for these parameters.

thermore, the burning and mixing are decoupled in the FUNS evolutionary code like in SNUPPAT but unlike ATON or MONASH (Cristallo et al. 2015). In regards to the overshooting from the bottom of the convective envelope and the formation of a ^{13}C pocket, the FUNS code uses a very similar approach to the one we have described in this PhD work for SNUPPAT, following an exponential decay of the velocities and mixing each overshooted shell with a time-scale dependent on the velocity at each point (Straniero et al. 2006).

Before delving into a more detailed analysis of the differences between FUNS results and ours, we shall restrict the parameter space we are analyzing. In the FRUITY webpage there is a total of four parameters to choose from when selecting a specific set of nucleosynthesis predictions: Initial mass, metallicity, initial rotational velocity, and the kind of ^{13}C pocket[6]. However, the parameter space shrinks considerably for our preferred metallicity of Z = 0.02. Indeed, once that metallicity is selected, the only models compatible with it have an initial rotational velocity of 0 and a *Standard* ^{13}C pocket (Cristallo et al. 2009).

These differences are realized in four important ways for the actual evolutionary models. First, the FUNS models undergo a significantly lower amount of TPs for the same mass than ATON. Second, the $\lambda_{\max}$ is slightly lower where comparable. Third, the maximum temperature in the He intershell is lower than in SNUPPAT. Fourth, the effective ^{13}C pockets are generally larger (up to, at least, the 4 $M_\odot$ model) than those we obtain in SNUPPAT. For example, their 4 $M_\odot$ model can develop an effective ^{13}C pocket of 6.5×10^{-4} $M_\odot$ (see Figure 16 from Cristallo et al. 2015), clearly higher than the 2×10^{-4} $M_\odot$ average effective ^{13}C pocket from SNUPPAT for the same initial mass. Moreover, their effective pockets profiles fall less abruptly than ours, which affects the total amount of material affected by *s*-process nucleosynthesis.

To understand how all these differences aggregate towards the final surface abundances, we start by comparing the FUNS models with ours in a procedure analogous to the one we carried out with the MONASH models, starting with the 3 and 4 $M_\odot$ SNUPPAT models.

There are two very clear divergences between the SNUPPAT and FUNS results that can be seen in Figure 5.4. The first one is a markedly lower neutron exposure in the FUNS models, probably a consequence of the low number of TPs (14 and 8 for the 3 and 4 $M_\odot$ FUNS models, respectively). This lower overall neutron exposure can be also deduced from both the negative [hs/ls] and [Pb/hs] ratios, as well as the Sr to Rb slope, which is opposite to the

[6]The possibilities for this option cover *Standard* and *Extended*. The *Standard* kind comes from a convective overshooting bounded by the number of pressure scale heights it is allowed to expand, while the *Extended* one has a similar lower limit to our *Boundless* case. That is, practically none.

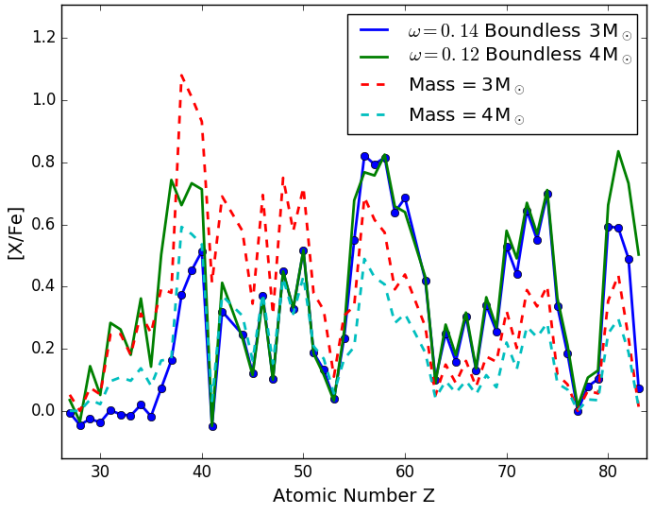

FIGURE 5.4— Final stellar surface abundances for both SNUPPAT (solid lines) and Fruity (dashed lines). The Fruity models chosen are those with the final abundances most similar to SNUPPAT in both absolute abundance values and abundance distributions. The blue solid line corresponds to a 3 $M_\odot$ simulation, while the green solid line corresponds to a 4 $M_\odot$ simulation.

obtained by SNUPPAT. For example, with a numerical experiment in which we integrate with a constant neutron density of 10^7 n/cm^3 at a temperature of 10^8 K, we find that to go from the Sr-Rb slope found in the FUNS 3 $M_\odot$ model to that of the SNUPPAT model displayed, the integration time must increase from around 3 thousand years to somewhere between 10 to 20 thousand years, increasing the neutron exposure a minimum of a threefold.

The second divergence between the two sets of models is the greater over-abundance around the first *s*-process peak of the FUNS 3 $M_\odot$ model, which we attribute to both the larger effective ^{13}C pockets developed in that code and the less efficient SNUPPAT dredge-up. To justify our characterization of SNUPPAT dredge-up as less efficient than that of FUNS in spite of the larger λ_{max} we must take into account the M_D/M_E coefficients for the different TPs. For example, we know that the geometric mean of this quantity for the 3 $M_\odot$

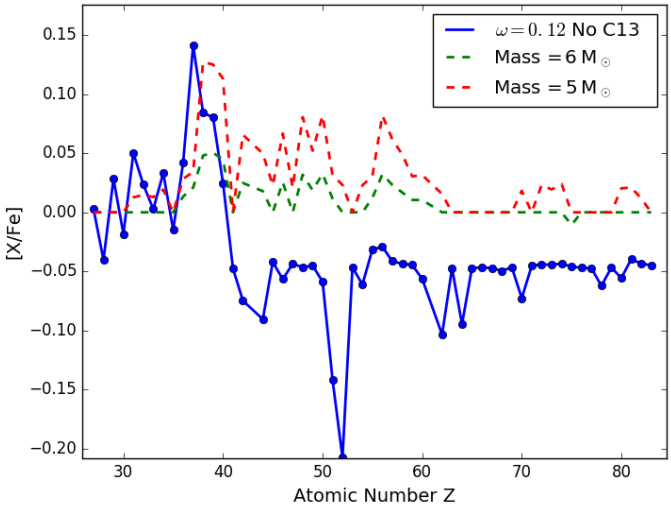

FIGURE 5.5— Same as Figure 5.4 for the SNUPPAT 5 $M_\odot$ model. The "No C13" label retains the same meaning as in Figure 5.3, that is, we have disabled the ^{13}C neutron source reaction for this simulation.

case is 8×10^{-4}, while in the FUNS model for the same mass we find a geometric mean of $\sim 2\times10^{-3}$. Recalling our use of expression (4.3.3), it is intuitive to see how the 14 FUNS TPs can yield comparable surface abundances, even when accounting for the lower $\lambda_{\rm max}$.

We can dig deeper by eschewing the averages and maxima, and looking at some individual TPs given that the surface abundances suffer greater changes towards the end of the TP-AGB evolution. One clarifying comparison comes from the very last pulse in the 3 $M_\odot$ case. For SNUPPAT, this pulse has a $\lambda = 0.05$, with an envelope mass of 0.95 $M_\odot$ and a dredged-up mass of 2.8×10^{-4} $M_\odot$. Contrasting this with FUNS last pulse for the same mass, with a $\lambda = 0.5$, an envelope mass of 0.87 $M_\odot$ and a dredged-up mass of 4.5×10^{-3} $M_\odot$. With this in mind it is not surprising to find that, for the same surface overabundance, SNUPPAT models show a much higher overall neutron exposure.

Finally, as it was the case with the MONASH models, SNUPPAT obtains a

[Rb/Sr] ratio noticeably higher than FUNS for the 4 $M_\odot$ mass model. This, of course, must be connected with the low efficiency of the ^{22}Ne neutron source (if active at all) for the FUNS simulations when compared to the ^{13}C nucleosynthesis overproduction (see also Karakas & Lugaro 2016 for a further discussion).

Turning our attention to the higher mass results (see Figure 5.5), we find again the signs of a much lower overall neutron exposure, to which we point towards the lower number of TPs once more (in this occasion, the number of TPs is 7 and 11 for the 5 and 6 $M_\odot$ FUNS models). More interestingly, we notice how the lower maximum temperatures mentioned before produce profiles incompatible with an efficient activation of the ^{22}Ne neutron source for the FUNS models. That is, the profile is more reminiscent to that of the ^{13}C pocket, with again a remarkably low [Rb/Sr] ratio when compared to SNUPPAT. We can further confirm this assertion when comparing these FUNS results with the MONASH models presented in Figure 5.3 where, for reference, we used the same results for the 5 $M_\odot$ simulation without ^{13}C neutron source.

5.4 NuGrid

In this Subsection we compare the SNUPPAT post-processing results with the NuGrid project data. The aim of this project (Pignatari et al. 2016) is to obtain an internally consistent grid of nucleosynthesis results for a wide range of stellar masses and metallicities. In particular, their so-called Set 1.2 includes nucleosynthesis data for masses between 1.65 and 60 $M_\odot$ for a metallicity of Z = 0.02. These results have been obtained by applying the post-processing code mppnp to the stellar evolutionary models of two different codes: MESA (Paxton et al. 2011) for low- and intermediate-mass stars and GENEC (Eggenberger et al. 2008) for more massive stars. Given that our own results consist of intermediate-mass stars, we focus from now on the MESA chosen physics.

The MESA models used for the NuGrid post-processing calculations are run assuming the Blöcker mass-loss formula, like in ATON. However, the parameter used in ATON is a constant $\eta = 0.02$ for every mass during the TP-AGB phase (for a discussion on the calibration of this parameter, see Ventura et al. 1998), while in the NuGrid case this parameter varies in the range $\eta \in [0.01, 0.08]$ depending on the initial mass and the C/O stellar surface ratio.

For the convective boundaries in the MESA calculations, the diffusive overshooting described by Herwig et al. (1997) is used with a choice of free parameter dependent on whether the code is currently simulating a TDU (when the overshooting is enhanced in order to generate a ^{13}C pocket), or in which the convective boundary is the boundary mixing being applied. For convective mixing these MESA models use the MLT scheme for convection.

Finally, we should point out that the post-processing code mppnp is, as SNUPPAT, a parallelized operator-splitting code in which the nucleosynthesis equations and the mixing processes are solved separately. This method contrast with the MONASH case, in which both processes are solved in the same step. The difference between these two approaches should be unnoticeable if the correct time step is chosen.

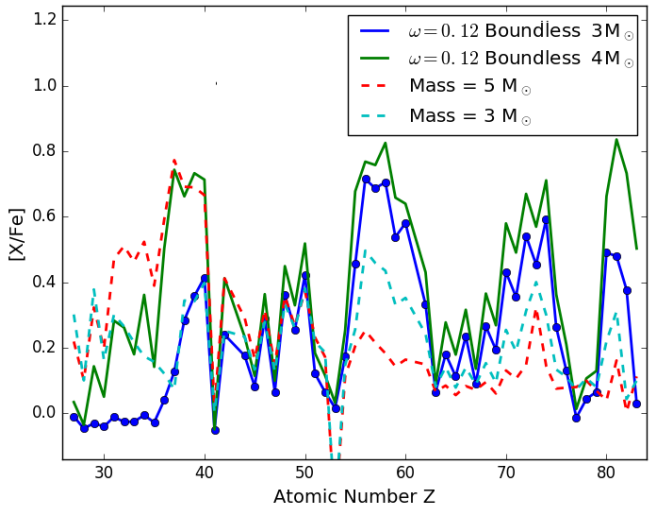

FIGURE 5.6— Final stellar surface abundances for both SNUPPAT (solid lines) and NuGrid (dashed lines). The NuGrid models chosen are those with final abundances most similar to SNUPPAT in both value and distribution profile.

The numerical integration, once finished, gives the NuGrid stellar models a lower to similar number of TP to SNUPPAT of around 20 to 25 for intermediate-mass stars, somewhat cooler PDCZ (5 to 20% cooler attending only to the maximum PDCZ temperatures for the same mass), and a generally larger dredge-up (λ) parameter. In fact, we think that this larger parameter is responsible for the main differences between the set of models for comparison (Figure 5.6). These atypically large λ values can range from 0.4 to 0.9 for the 3 $M_\odot$ model to 0.8 to 1.1 for the 4 $M_\odot$ case, with the 5 $M_\odot$ simulation remaining

in between the extreme values.

In Figure 5.4 we have displayed two SNUPPAT models, of 3 and 4 $M_\odot$ and two NuGrid models of 3 and 5 $M_\odot$. We have decided to skip the 4 $M_\odot$ case for NuGrid because it is essentially identical to the 5 $M_\odot$ case but scaled upwards in total overproduction. Likewise, we have skipped the 5 $M_\odot$ SNUPPAT case because it does not give us additional information on account of what we have just pointed out.

The stellar surface abundances for both nucleosynthesis codes show the already familiar picture of the SNUPPAT simulations being compatible with a higher overall neutron exposure. That is, the second and third *s*-process peaks are lower than in SNUPPAT although the first peak is very similar between both nucleosynthesis codes. This interpretation is reinforced by some abundance ratios such as [Ge/Sr] (Z = 32 for Ge), which are higher for lower neutron exposures in this regime.

Finally, we should point out that the higher average λ parameter along with a lower number of TPs is enough to explain the differences between the SNUPPAT and NuGrid predictions. Such combination, in particular, allows for a lower overall neutron exposure and a comparable first *s*-process peak. Interestingly, the 5 $M_\odot$ NuGrid model, predicts a [Rb/Sr] ratio very similar to that of the SNUPPAT 4 $M_\odot$ simulation. This is consistent with the activation of the ^{22}Ne neutron source, but without a significant change of the neutron exposure as evidenced by their relatively large [Ge/Sr] ratio.

5.5 Conclusions

The comparison between the SNUPPAT simulations and those of other groups has revealed the position our calculations inhabit among the nucleosynthesis codes. The most notable differences are centered around the overall neutron exposure, with SNUPPAT showing, in general, signs of a higher neutron exposure than the results of other groups. This appears to be the consequence of SNUPPAT having less efficient TDU; being reflected both in the λ parameter and in the M_D/M_E ratio. The second notable difference is the higher temperature maxima found in ATON models, which enhance the ^{22}Ne neutron source beyond what can be found in other evolutionary codes for the same mass.

Among the three codes we have selected for our comparison, it is clear that the results belonging to MONASH simulations are the most reminiscent to SNUPPAT surface abundances. This is not surprising as we are not only using almost the same nuclear network but we find also similar effective ^{13}C pocket sizes, λ values, and number of TPs. This fact also confirms that the particular implementation of an overshooting mechanism (be it a PMZ or our

advective approach) is not particularly critical for the *s*-process nucleosynthesis besides the formation of an effective ^{13}C pocket in the more massive objects, as discussed in the previous chapter. This conclusion is in accordance to recent work by Goriely & Siess (2018), where *s*-process abundances were obtained for two different overshooting mechanisms and proven to be fairly consistent for a 2 $M_{\odot}$ stellar simulation of subsolar metallicity. Indeed, the FUNS code uses an extra-mixing simulation analogous to ours, but we find that the other structural differences are more fundamental to the stellar surface abundances distribution.

There are two clear lines of future work that we can draw from the results of this chapter. The first one is an extension of our calculations to more metallicities, and the second one is an exhaustive comparison of both the current solar and future sub-solar metallicities results with observational data on known AGB stars and related objects like post-AGB stars and PNe (see Chapter 7). The latter study could also help the nucleosynthesis community to elucidate which of the SNUPPAT mechanisms should be reworked, as well as which ones are more consistent with reality.

6

Conclusions

6.1 SNUPPAT: The nucleosynthesis code

The complete description and testing of SNUPPAT has been presented. We have described our success at the creation of a *s*-process nucleosynthesis code along with our efforts to optimize it.

The code itself consists mainly of a method for solving a stiff system of ODE, and an overshooting algorithm. For the former, we have decided to use a semi-implicit approach for the modified mid-point rule known as the BD method. This approach combines the order flexibility of a Richardson extrapolation, along with an automatic time step adjustment that attempts to find the largest possible time step that keeps the solution below the imposed accuracy limit. For the overshooting algorithm we have decided to use an advective approach very similar to that of the FUNS code (Straniero et al. 2006), which not only depends on physical parameters of the evolutionary model, but it also makes for a computationally cheap method to solve. The code has been trivially parallelized by dividing the calculation among the shells in the nucleosynthesis step and among the species in the mixing step.

We have studied two different acceleration techniques for the most computationally intensive part of the code, which is the solution to the linear system of equations that arise from using the BD method. The first one is the application of the GS method instead of the LU factorization, which turns out to be an improvement in both speed an accuracy for some of the mass shells. The second acceleration has to do with disposing of the linear system of equations altogether by utilizing the Patankar-Euler algorithm instead of the semi-implicit modified mid-point rule for the BD method. We have also shown that only a handful of expressions must be modified to go from one method to the other,

and the change can result in a three fold speed-up in one particular example.

The main takeaway, however, is that SNUPPAT correctly simulates the AGB *s*-process nucleosynthesis in a post-processing environment. In the three tests conducted, we have shown that it is capable of both accurately integrating a 320 species network with neutron captures from a ^{13}C pocket and of following a real AGB simulation with several TPs while producing the exact abundances at the intershell level. Furthermore, we have discussed that the most significant differences between SNUPPAT and other codes, outside of HBB nucleosynthesis, are consequence of mathematical inaccuracies rather than the code performance. Finally, we have drawn special attention to the sensitivity that the AGB simulations have to the interpolation technique used, and we have proposed our preferred method to avoid some of the problems posed by an adaptive mesh.

6.2 SNUPPAT: Predictions and comparison

We have taken a careful look into the effects of our particular extra-mixing implementation, we have presented the SNUPPAT results as final stellar surface abundances, and we have compared our code with the best known numerical codes for *s*-process nucleosynthesis.

Our study into the extra-mixing effects has made it patently clear that, in both ATON and SNUPPAT, the presence of an overshooting mechanism at either the bottom of the PDCZ or the convective envelope has clear consequences for the final *s*-process nucleosynthesis production at the stellar surface. The case of extra-mixing at the bottom of the PDCZ is specially relevant for the evolutionary code, as it can fundamentally affect the core growth impacting the dredge-up mass and the λ parameter. However, we have seen how it is critical to also apply a consistent overshooting mechanism at the bottom of the PDCZ in the post-processing phase, because it can enhance the ^{13}C neutron source production through the inclusion of core ^{12}C into the He intershell.

On the other hand, the inclusion of an extra-mixing simulation at the bottom of the convective envelope is more readily justified, knowing that no effective ^{13}C pocket ever forms without them. The lack of effective ^{13}C pocket formation is at odds with reality, as there is no other mechanism currently able to explain the *s*-process surface overabundance for low- to intermediate-mass solar metallicity stars. Therefore, in order to find any amount of nucleosynthesis in the less massive C-rich AGB stars, we have decided to adopt a time-dependent advective overshooting approach that takes into account the convective velocities, tying it to the stellar physics at each specific TP. This approach makes the ^{13}C pocket very sensitive to the particular choice of endpoint for the overshooting mechanism, as we have found in our comparison between the *bounded*

and *boundless* cases. Finally, the most important consequence of our preference for an advective mechanism is that the effective ^{13}C pocket does not disappear on its own in the more massive and O-rich AGB stellar models. Therefore, we must manually deactivate this neutron source if we want to obtain the nucleosynthesis products arising exclusively from the ^{22}Ne neutron source, a case some theoretical groups predict should take place for the more massive AGB stars.

We have then connected the previous extra-mixing analysis with the final SNUPPAT results for solar metallicity stars. These results show a comprehensive picture in which the *boundless* overshooting mechanism appears to be the most adequate choice for surface nucleosynthesis in account of the overall *s*-process stellar surface abundances. Among the mass parameter, it is easy to see that the 4 $M_\odot$ simulations return the highest *s*-process yields of all, with a [Rb/Sr] ratio typical of more massive stars when considering other evolutionary codes. For the 5 $M_\odot$ results, we have presented two different kinds of simulations, the first of which allows for neutron production by the ^{13}C neutron source, and the second which does not. For the first case, a picture analogous to that of the 4 $M_\odot$ case appears, with the main differences being more marked effects from the ^{22}Ne neutron source, appearing in the [Rb/Sr] and [Cs/Ba] ratios. When disabling the ^{13}C neutron source, we find a markedly changed abundance distribution with an almost exclusive overproduction in [Rb/Fe]. This can be explained by a low neutron exposure halted by the first peak magic number, with a preference of Rb over Sr due to the higher neutron density product of the ^{22}Ne source. In this case, two different simulations were conducted: one in which the overshooting parameter was set to zero, and another one in which just the ^{13}C neutron source reaction was modified so as to not release neutrons. Here it is important to understand that, although neither of these approaches are a perfect simulation of the mechanism found by Goriely & Siess (2004), there is not a significant difference between these alternatives in the final stellar surface abundance distributions, which means that the change in ^{14}N between both cases does not carry over to the actual nucleosynthesis in the end.

Finally, we were able to contextualize the SNUPPAT results by comparing them with those from the MONASH code and the FRUITY and NuGrid projects. The first notable difference is centered around the overall neutron exposure, which is a consequence of SNUPPAT being less efficient dredging-up, both when measured with the λ parameter or through the M_D/M_E ratio. This means that for the same surface *s*-process overabundances SNUPPAT must produce more nucleosynthesis in the intershell, increasing its overall neutron exposure above that of other *s*-process codes.

The second notable difference is inextricably tied to the stellar evolutionary code ATON, which has higher temperature maxima than that of other codes for the same mass and evolutionary stage. The best known consequence is the appearance of HBB for relatively lower masses (Mazzitelli et al. 1999) than in other evolutionary codes. However, for the first time we are able to confirm that ATON does also activate the ^{22}Ne neutron source as efficiently as a MONASH 4.5 $M_{\odot}$ model for a 4 $M_{\odot}$ case. This observation lowers the minimum theoretical mass necessary for a positive [Rb/Sr] ratio.

Among the predictions from the selected numerical codes, SNUPPAT finds a closer similarity to those from MONASH for the range of masses considered at solar metallicity. Coincidentally, MONASH is the nucleosynthesis code out of the three considered that better explains the currently limited observational information about these (3-6 $M_{\odot}$) stars. For the other two codes, the NuGrid case adjusts quite well for the first *s*-process peaks for approximately the same mases as SNUPPAT, and the FRUITY abundances are the most dissimilar among the three. Interestingly enough, FUNS uses an advective approach for overshooting much like ours. Therefore, the stellar surface abundances confirm that, for the *s*-process the precise overshooting mechanism is unimportant. With the exception, as pointed out already, of the formation of an effective ^{13}C pocket for stars above 5 $M_{\odot}$.

7

Future Work

This thesis has been centered around two main topics that work in tandem. On one hand, we have created a new post-processing *s*-process nucleosynthesis code from scratch tailored to the stellar evolutionary code ATON. On the other, we have run this code to obtain our first batch of *s*-process element predictions to compare with other known *s*-process nucleosynthesis codes.

For the first topic, we propose two distinct avenues for future work. The first one is the most intuitive for any calculation that is as computationally expensive as ours to perform. That is, we are interested in optimizing Snuppat further if possible, through both exploration and application of new numerical integration methods and better parallelization routines. Both paths have the potential to not only reduce time and expenses to obtain our particular nucleosynthesis predictions, but also might be applicable to the nucleosynthesis community as a whole. The second avenue we want to tackle in the future of the code is the addition of two alternative models for both convection and overshooting. For the first one, we are interested in introducing non-instantaneous mixing, while for the second one we want to have an alternative module to simulate diffusive overshooting. Our main objective in this case is to answer some of the questions we have encountered while developing this work, as well as extending the range of species and processes correctly simulated by the Snuppat code. For the *s*-process elements this would allow us to decouple the ATON physics effects on heavy *s*-element nucleosynthesis from those arising from our mixing hypotheses.

For the second topic, the future work is a natural extension of what we have done in this PhD work. On one hand, we have to extend our calculations to lower metallicities and a broader range of masses. On the other hand, we

would like to compare our theoretical predictions with the observation of heavy *s*-process elements on several type of objects showing the imprint of AGB stellar nucleosynthesis, such as AGB and post-AGB stars, and planetary nebulae (PNe). However, every one of these objects presents its own challenges in the determination of *s*-process abundances: i) For AGB stars we know that the surface chemistry is still evolving, introducing a great uncertainty factor as it is possible that different masses can arrive to similar stellar surface abundance profiles at different moments in their evolution. Moreover, for many species the TPs near the end of the AGB life (when it is obscured by its own ejected envelope) are the instances in which the surface chemical composition changes the fastest. Additionally, the complex dynamical atmospheres of AGB stars can affect the derived abundances of elements such as Rb in orders of magnitude (see e.g., Zamora et al. 2014; Pérez-Mesa et al. 2017). ii) In the post-AGB stars we avoid the evolutionary uncertainty as the star chemistry is not evolving anymore, and their photospheres are hotter, allowing for more accurate abundance determinations. However, because of their short lifetimes (10^{2-4} years) there are very few of these objects identified in the Galaxy, and the observations are heavily biased towards the longer lived low-mass progenitors (1-2 $M_{\odot}$). iii) Finally, the PNe present the same advantages as post-AGB stars, along with being brighter and covering a wider range of stellar parameters (such as initial masses). The downside is that many key elements of the PNe to understand AGB evolution have to be observed in either high-resolution optical/near-IR spectra or UV spectra, both of which present their own observational challenges.

Hopefully, we expect for this situation to change in the near future thanks to the data of large surveys, the increasing identification of *s*-elements in PNe, etc.

Bibliography

Abia, C., Domínguez, I., Gallino, R., Busso, M., Masera, S., Straniero, O., de Laverny, P., Plez, B., and Isern, J. 2002, ApJ, 579, 817

Abia, C., Busso, M., Gallino, R., Domínguez, I., Straniero, O., and Isern, J. 2001, ApJ, 559, 1117

Bader, G., and Deuflhard, P. 1983, Numer. Math., 41, 373

Bagnara, R. 1995, SIAM Rev., 37, 93

Bisterzo, S., Gallino, R., Straniero, O., Ivans, I. I., Käppeler, F., and Aoki, W. 2006, MmSAI, 77, 985

Blöcker, T. 1995, A&A, 297, 727

Boothroyd, A. I., Sackmann, J. I., and Ahern S. C. 1993, ApJ, 416, 762

Bulirsch, R., and Stoer, J. 1966, Numer. Math., 8, 1

Buntain, J. F., Doherty, C. L., Lugaro, M., Lattanzio, J. C., Stancliffe, R. J., and Karakas, A. I. 2017, MNRAS, 471, 824

Burchard, H., Deleersnijder, E., and Meister, A. 2003, Appl Numer Math, 47, 1

Burchard, H., Deleersnijder, E., and Meister, A. 2005, Ocean Dyn, 55, 326

Busso, M., Gallino, R., and Wasserburg, G. J. 1999, ARA, 37, 239

Busso, M., Gallino, R., Lambert, D. L., Travaglio, C., and Smith, V. V. 2001, ApJ, 557, 802

Cannon, R. C. 1993, MNRAS, 263, 817

Canuto, V. M., Goldman, I., and Mazzitelli, I. 1996, ApJ, 473, 550

Cameron, A. G. W. 1955, ApJ, 121, 144C

Clayton, D. D., Fowler, W. A., Hull, T. E., and Zimmerman, B. A. 1961, Ann. Phys., 12, 331

Clayton, D. D. 1988, MNRAS, 234, 1

Cristallo, S., Straniero, O., Gallino, R., Piersanti, L., Domínguez, I. and Lederer, M. T. 2009, ApJ, 696, 797

Cristallo, S., Straniero, O., Piersanti, L., and Gobrecht, D. 2015, ApJS, 219, 40

Cyburt, R. H., Amthor, A. M., Ferguson, R., Meisel, Z., Smith, K., Warren, S., Heger, A., Hoffman, R. D., Rauscher, T., Sakharuk, A., Schatz, H., Thielemann, F. K., and Wiescher, M. 2010, ApJS, 189, 240

Deuflhard, P. 1983, Numer. Math., 41, 399

Eggenberger, P., Meynet, G., Maeder, A., Hirschi, R., Charbonnel, C., Talon, S., and Ekström, S. 2008, Ap&SS, 316, 43

García-Hernández, D. A., García-Lario, P., Plez, B., D'Antona, F., Manchado, A., and Trigo-Rodríguez, J. M. 2006, Sci, 314, 1751G

García-Hernández, D. A., García-Lario, P., Plez, B., Manchado, A., D'Antona, F., Lub, J., and Habing, H. 2007, ApJ, 462, 711

García-Hernández, D. A., Manchado, A., Lambert, D. L., Plez, B., García-Lario, P., D'Antona, F., Lugaro, M., Karakas, A. I., and van Raai, M. A., 2009, ApJ, 705, L31

García-Hernández, D. A., Zamora, O., Yagüe, A., Uttenthaler, S., Karakas, A. I., Lugaro, M., Ventura, P., and Lambert, D. L. 2013, A&A, 555, L3

Goriely, S., and Mowlavi, N. 2000, A&A362, 599

Goriely, S., and Siess L. 2004, A&A421, L25

Goriely, S., and Siess L. 2018, A&A609, A29

Hairer, E., Bader, G., and Lubich, CH. 1982, BIT, 22, 211

Hampel, M., Stancliffe, R. J., Lugaro, M., and Meyer, B. S. 2016 ApJ, 831, 171

Herwig, F., Blöcker, T., Schönberner D., and El Eid, M. 1997, ApJ, 324, L81

Herwig, F. 2000, A&A, 360, 952

Herwig, F., and Langer, N. 2000, MmSAI, 72, 277H

Herwig, F., Langer, N., and Lugaro, M. 2003 ApJ, 593, 1056

Herwig, F. 2005 ARA&A, 43, 435

Iben, I. 1991 ApJS, 76, 55

Käppeler, F., Gallino, R., Bisterzo, S., and Aoki, W. 2011, RvMP, 83, 157

Kamath, D., Karakas, A. I., and Wood, P. R. 2012, ApJ, 746, 20

Karakas, A. I., and Lattanzio, J. C. 2003, PASA, 20, 393

Karakas, A. I. 2010, MNRAS, 403, 1413

Karakas, A. I., and Lattanzio, J. C. 2014, PASA, 31, 30K

Karakas, A. I. 2014, MNRAS, 445, 347

Karakas, A. I., and Lugaro, M. 2016, ApJ, 825, 26

Lambert, D. L., Smith, V. V., Busso, M., Gallino, R., and Straniero, O. 1995, ApJ, 450, 302

Lattanzio, J. C., Frost, C., Cannon, R., and Wood, P. R. 1996, MmSAI, 67, 729

Lattanzio, J. C., Tout, C. A., Neumerzhitckii, E. V., Karakas, A. I., and Lesaffre, P. 2017, MmSAI, 88, 248

Lau, H. H. B., Gil-Pons, P., Doherty, C., and Lattanzio, J. 2012, A&A, 542, A1

Liu, N., Savina, M. R., Davis, A. M., Gallino, R., Straniero, O., Gyngard, F., Pellin, M. J., Willingham, D. G., Dauphas, N., Pignatari, M., Bisterzo, S., Cristallo, S., Herwig, F. 2014, A&A, 786, 66

Longland, R., Martin, D., and José, J. 2014, A&A, 563, A67

Lugaro, M., Herwig, F., Lattanzio, J. C., Gallino, R., and Straniero, O. 2003, ApJ, 586, 1305

Magic, Z., Collet, R., and Asplund, M. 2013, EAS, 63, 367M

Marigo, P., Bressan, A., Nanni, A., Giardi, L., and Letizia Pumo, M. 2013, MNRAS, 434, 488

Mathews, G. J., Takahashi, K., Ward, R. A., and Howard, W. M. 1986, ApJ, 302, 410

Mazzitelli, I., D'Antona, F., and Ventura, P. 1999, A&A, 348, 846

Mazzitelli, I., D'Antona, F., and Ventura, P. 2000, MmSAI, 71, 729M

Müller, B., and Janka, H. Th. 2015, MNRAS, 448, 2141

Palmerini, S., La Cognata, M., Cristallo, S., and Busso, M. 2011, ApJ, 729, 3

Paxton, B., Bildsten, L., Dotter, A., Herwig, F., Lesaffre, P., and Timmes, F. 2011, ApJS, 192, 3

Pérez-Mesa, V., Zamora, O., García-Hernández, D. A., Plez, B., Manchado, A., Karakas, A. I., and Lugaro, M. 2017, A&A, 606, A20

Pignatari, M., Gallino, R., Heil, M., Wiescher, M., Käppeler, F., Herwig, F., and Bisterzo, S. 2010, ApJ, 710, 1557

Pignatari, M., Herwig, F., Hirschi, R., Bennett, M., Rockefeller, G., Fryer, C., Timmes, F. X., Ritter, C., Heger, A., and Jones, S. 2016, ApJ, 225, 24

Qian, Y. Z. 2003 PrPNP, 50, 153Q

Seidel, P. 1874, Münch Abh., 2(3), 81

Stancliffe, R. J., Dearborn, D. S. P., Lattanzio, J. C., Heap, S. A., and Campbell S. W. 2011, ApJ, 742, 121

Steffen, M. 1990, A&A, 239, 443

Straniero, O., Gallino, R., and Cristallo, S. 2006, Nuclear Physics A., 777, 311S

Straniero, O., Cristallo, S., and Gallino, R. 2009, PASA, 26, 133

Tremblay, P. E., Ludwig, H. G., Steffen, M., and Freytag, B. 2013, A&A, 559, A104

Trujillo Bueno, J., and Fabiani Bendicho, P. 1995, ApJ, 455, 646

van Raai, M. A., Lugaro, M., Karakas, A. I., García-Hernández, D. A., and Yong, D. 2012, A&A, 540, A44

Vassiliadis, E., and Wood, P. R. 1993, ApJ, 413, 641 van Raai, M. A., Lugaro, M., Karakas, A. I., García-Hernández, D. A., and Yong, D. 2012, A&A, 540, A44

Ventura, P., D'Antona, F., and Mazitelli, I. 2008, Ap&SS, 316, 93

Ventura, P., Zeppieri, A., Mazzitelli, I., and D'Antona, F. 1998, A&A, 334, 953

Ventura, P., Di Criscienzo, M., Carini, R., and D'Antona, F. 2013, MNRAS, 431, 3642

Zamora, O., García-Hernández, D. A., Plez, B., and Manchado A. 2014, A&A, 564, L4

A

Tables with the final stellar surface abundances

Name	Z	[X/Fe]	Name	Z	[X/Fe]	Name	Z	[X/Fe]
Co	27	-0.01	Ni	28	-0.05	Cu	29	-0.03
Zn	30	-0.04	Ga	31	-0.01	Ge	32	-0.03
As	33	-0.02	Se	34	-0.01	Br	35	-0.03
Kr	36	0.04	Rb	37	0.13	Sr	38	0.28
Y	39	0.36	Zr	40	0.41	Nb	41	-0.05
Mo	42	0.24	Ru	44	0.18	Rh	45	0.08
Pd	46	0.29	Ag	47	0.07	Cd	48	0.36
In	49	0.26	Sn	50	0.42	Sb	51	0.12
Te	52	0.07	I	53	0.02	Xe	54	0.17
Cs	55	0.46	Ba	56	0.71	La	57	0.69
Ce	58	0.71	Pr	59	0.54	Nd	60	0.58
Sm	62	0.33	Eu	63	0.07	Gd	64	0.18
Tb	65	0.11	Dy	66	0.24	Ho	67	0.09
Er	68	0.27	Tm	69	0.19	Yb	70	0.43
Lu	71	0.36	Hf	72	0.54	Ta	73	0.45
W	74	0.59	Re	75	0.26	Os	76	0.13
Ir	77	-0.01	Pt	78	0.04	Au	79	0.07
Hg	80	0.49	Tl	81	0.48	Pb	82	0.38
Bi	83	0.03	–	–	–	–	–	–

TABLE A.1— Stellar surface [X/Fe] values for the 3 $M_{\odot}$ $\omega = 0.12$ predictions.

Name	Z	[X/Fe]	Name	Z	[X/Fe]	Name	Z	[X/Fe]
Co	27	-0.01	Ni	28	-0.05	Cu	29	-0.03
Zn	30	-0.04	Ga	31	-0.00	Ge	32	-0.02
As	33	-0.02	Se	34	0.01	Br	35	-0.02
Kr	36	0.06	Rb	37	0.15	Sr	38	0.35
Y	39	0.43	Zr	40	0.49	Nb	41	-0.05
Mo	42	0.30	Ru	44	0.23	Rh	45	0.11
Pd	46	0.35	Ag	47	0.09	Cd	48	0.43
In	49	0.31	Sn	50	0.49	Sb	51	0.17
Te	52	0.11	I	53	0.03	Xe	54	0.21
Cs	55	0.51	Ba	56	0.78	La	57	0.75
Ce	58	0.77	Pr	59	0.60	Nd	60	0.64
Sm	62	0.39	Eu	63	0.09	Gd	64	0.22
Tb	65	0.14	Dy	66	0.28	Ho	67	0.11
Er	68	0.31	Tm	69	0.23	Yb	70	0.49
Lu	71	0.40	Hf	72	0.60	Ta	73	0.51
W	74	0.65	Re	75	0.30	Os	76	0.16
Ir	77	-0.01	Pt	78	0.06	Au	79	0.09
Hg	80	0.55	Tl	81	0.53	Pb	82	0.45
Bi	83	0.06	–	–	–	–	–	–

TABLE A.2— Stellar surface [X/Fe] values for the 3 $M_{\odot}$ $\omega = 0.14$ predictions.

Name	Z	[X/Fe]	Name	Z	[X/Fe]	Name	Z	[X/Fe]
Co	27	0.03	Ni	28	-0.03	Cu	29	0.14
Zn	30	0.05	Ga	31	0.28	Ge	32	0.26
As	33	0.18	Se	34	0.36	Br	35	0.14
Kr	36	0.50	Rb	37	0.74	Sr	38	0.66
Y	39	0.73	Zr	40	0.71	Nb	41	-0.05
Mo	42	0.41	Ru	44	0.23	Rh	45	0.11
Pd	46	0.36	Ag	47	0.10	Cd	48	0.45
In	49	0.33	Sn	50	0.52	Sb	51	0.18
Te	52	0.12	I	53	0.03	Xe	54	0.25
Cs	55	0.68	Ba	56	0.77	La	57	0.76
Ce	58	0.82	Pr	59	0.66	Nd	60	0.64
Sm	62	0.43	Eu	63	0.09	Gd	64	0.28
Tb	65	0.18	Dy	66	0.32	Ho	67	0.14
Er	68	0.37	Tm	69	0.27	Yb	70	0.58
Lu	71	0.49	Hf	72	0.67	Ta	73	0.57
W	74	0.71	Re	75	0.36	Os	76	0.21
Ir	77	0.01	Pt	78	0.11	Au	79	0.13
Hg	80	0.66	Tl	81	0.84	Pb	82	0.73
Bi	83	0.50	–	–	–	–	–	–

TABLE A.3— Stellar surface [X/Fe] values for the 4 $M_{\odot}$ $\omega = 0.12$ predictions.

Name	Z	[X/Fe]	Name	Z	[X/Fe]	Name	Z	[X/Fe]
Co	27	0.03	Ni	28	-0.03	Cu	29	0.16
Zn	30	0.08	Ga	31	0.38	Ge	32	0.37
As	33	0.28	Se	34	0.53	Br	35	0.25
Kr	36	0.91	Rb	37	1.16	Sr	38	1.04
Y	39	1.15	Zr	40	1.22	Nb	41	-0.05
Mo	42	0.92	Ru	44	0.71	Rh	45	0.44
Pd	46	0.86	Ag	47	0.38	Cd	48	0.95
In	49	0.78	Sn	50	1.05	Sb	51	0.62
Te	52	0.55	I	53	0.22	Xe	54	0.73
Cs	55	1.35	Ba	56	1.29	La	57	1.23
Ce	58	1.29	Pr	59	1.09	Nd	60	1.04
Sm	62	0.81	Eu	63	0.27	Gd	64	0.60
Tb	65	0.43	Dy	66	0.63	Ho	67	0.36
Er	68	0.71	Tm	69	0.57	Yb	70	0.97
Lu	71	0.85	Hf	72	1.06	Ta	73	0.95
W	74	1.11	Re	75	0.69	Os	76	0.47
Ir	77	0.11	Pt	78	0.30	Au	79	0.33
Hg	80	1.04	Tl	81	1.23	Pb	82	1.19
Bi	83	1.10	–	–	–	–	–	–

TABLE A.4— Stellar surface [X/Fe] values for the 4 $M_{\odot}$ $\omega = 0.14$ predictions.

Name	Z	[X/Fe]	Name	Z	[X/Fe]	Name	Z	[X/Fe]
Co	27	0.01	Ni	28	-0.04	Cu	29	0.01
Zn	30	-0.04	Ga	31	-0.01	Ge	32	-0.04
As	33	-0.03	Se	34	-0.04	Br	35	-0.04
Kr	36	-0.02	Rb	37	0.08	Sr	38	-0.03
Y	39	-0.01	Zr	40	-0.04	Nb	41	-0.05
Mo	42	-0.10	Ru	44	-0.10	Rh	45	-0.05
Pd	46	-0.07	Ag	47	-0.05	Cd	48	-0.06
In	49	-0.05	Sn	50	-0.07	Sb	51	-0.15
Te	52	-0.21	I	53	-0.05	Xe	54	-0.06
Cs	55	-0.04	Ba	56	-0.03	La	57	-0.04
Ce	58	-0.05	Pr	59	-0.05	Nd	60	-0.06
Sm	62	-0.10	Eu	63	-0.05	Gd	64	-0.10
Tb	65	-0.05	Dy	66	-0.05	Ho	67	-0.05
Er	68	-0.05	Tm	69	-0.05	Yb	70	-0.07
Lu	71	-0.05	Hf	72	-0.04	Ta	73	-0.04
W	74	-0.04	Re	75	-0.05	Os	76	-0.05
Ir	77	-0.05	Pt	78	-0.06	Au	79	-0.05
Hg	80	-0.06	Tl	81	-0.04	Pb	82	-0.04
Bi	83	-0.04	–	–	–	–	–	–

TABLE A.5— Stellar surface [X/Fe] values for the 5 $M_\odot$ $\omega = 0.12$ predictions without ^{13}C.

Name	Z	[X/Fe]	Name	Z	[X/Fe]	Name	Z	[X/Fe]
Co	27	0.01	Ni	28	-0.04	Cu	29	0.07
Zn	30	0.01	Ga	31	0.15	Ge	32	0.13
As	33	0.08	Se	34	0.20	Br	35	0.06
Kr	36	0.33	Rb	37	0.49	Sr	38	0.49
Y	39	0.56	Zr	40	0.56	Nb	41	-0.05
Mo	42	0.32	Ru	44	0.18	Rh	45	0.08
Pd	46	0.28	Ag	47	0.06	Cd	48	0.36
In	49	0.25	Sn	50	0.42	Sb	51	0.12
Te	52	0.06	I	53	0.01	Xe	54	0.18
Cs	55	0.61	Ba	56	0.64	La	57	0.62
Ce	58	0.66	Pr	59	0.50	Nd	60	0.50
Sm	62	0.29	Eu	63	0.04	Gd	64	0.17
Tb	65	0.11	Dy	66	0.21	Ho	67	0.08
Er	68	0.25	Tm	69	0.18	Yb	70	0.41
Lu	71	0.34	Hf	72	0.51	Ta	73	0.42
W	74	0.55	Re	75	0.25	Os	76	0.12
Ir	77	-0.01	Pt	78	0.04	Au	79	0.07
Hg	80	0.49	Tl	81	0.62	Pb	82	0.58
Bi	83	0.40	–	–	–	–	–	–

TABLE A.6— Stellar surface [X/Fe] values for the 5 $M_{\odot}$ $\omega = 0.12$ predictions.

Name	Z	[X/Fe]	Name	Z	[X/Fe]	Name	Z	[X/Fe]
Co	27	-0.01	Ni	28	-0.04	Cu	29	-0.00
Zn	30	-0.04	Ga	31	-0.00	Ge	32	-0.02
As	33	-0.02	Se	34	-0.01	Br	35	-0.03
Kr	36	0.04	Rb	37	0.15	Sr	38	0.04
Y	39	0.07	Zr	40	0.06	Nb	41	-0.05
Mo	42	-0.04	Ru	44	-0.07	Rh	45	-0.03
Pd	46	-0.02	Ag	47	-0.04	Cd	48	-0.01
In	49	-0.02	Sn	50	0.01	Sb	51	-0.11
Te	52	-0.18	I	53	-0.04	Xe	54	-0.02
Cs	55	0.18	Ba	56	0.14	La	57	0.14
Ce	58	0.18	Pr	59	0.11	Nd	60	0.09
Sm	62	-0.01	Eu	63	-0.03	Gd	64	-0.04
Tb	65	-0.02	Dy	66	0.01	Ho	67	-0.02
Er	68	0.03	Tm	69	0.01	Yb	70	0.06
Lu	71	0.05	Hf	72	0.12	Ta	73	0.08
W	74	0.14	Re	75	0.03	Os	76	-0.01
Ir	77	-0.04	Pt	78	-0.04	Au	79	-0.02
Hg	80	0.11	Tl	81	0.20	Pb	82	0.14
Bi	83	0.05	–	–	–	–	–	–

TABLE A.7— Stellar surface [X/Fe] values for the 6 $M_{\odot}$ $\omega = 0.08$ predictions.